ANALYSIS OF THE STRUCTURAL INTEGRITY OF AN AUTOMOBILE ALUMINIUM ALLOY WHEELWITH SELECTED COOLING HOLE GEOMETRIES

BY

Samuel Onoriode IGBUDU

B. Eng. Mechanical Engineering (Minna) M. Sc. Mechanical Engineering (Ibadan)

(Matric. No. 109990)

A Thesis in the Department of Mechanical Engineering,
Submitted to the Faculty of Technology
in partial fulfillment of the requirements for the Degree of

DOCTOR OF PHILOSOPHY

of the

UNIVERSITY OF IBADAN

NOVEMBER 2018

CERTIFICATION

This is to certify that this research work was carried out by S. O. IGBUDU in the Department of Mechanical Engineering, University of Ibadan, Ibadan, Nigeria. .

.....

Supervisor

Dr D. A. Fadare

B. Sc., M. Sc., Ph.D, (Ibadan). Reg. Engr (COREN)

Reader, Department of Mechanical Engineering,

University of ibadan, Nigeria

ABSTRACT

Aluminium alloy wheels are increasingly popular for their light weight and good thermal conductivity. However, there are efforts to introduce Cooling Holes (CH) to reduce their weight without compromising structural integrity. Varieties of CH in use are mostly of parabolic or circular geometry. Literature is sparse on the use of triangular, square and oval shaped CH in wheel design. This study was, therefore, designed to investigate the structural integrity of an aluminium alloy wheel with triangular, quadrilateral and oval shaped CH.

Five-armed-wheel (6JX14H2ET42) with parabolic CH each of 3466 mm^2 area were sourced from the James Watt market, Benin city. Young's Modulus, yield stress, and Poison's ratio were determined. Inner surface of the wheel-tyre assembly was prepared and strain rosette attached at points between 0° and 180° at interval of 30° at wheel's well, Inboard Bead Seat (IBS) and Outboard Bead Seat (OBS). The assembly was mounted on an hydraulically operated static radial test rig and loaded statically with Radial Load (RL) of 4750 N and Inflation Pressures (IP) of 0.3 and 0.15 MPa, respectively. Mean contact patch and strains were measured and converted to contact angle and stresses using trigonometric and stress-strain equations, respectively. A 3-D numerical model for a wheel with parabolic-CH was developed and solved using Finite Element Method (FEM) to determine stress distribution at well, IBS and OBS. The FEM and experimental stress values were analysed using ANOVA at $\alpha_{0.05}$. Further numerical study was conducted for quadrilateral-CH and oval-CH at Aspect Ratios (AR) 0.78 and 0.71, respectively at 4750 N RL and IP of 0.3 MPa, with equal CH area of 3466 mm^2. Numerical study was also conducted at IBS with CH area of 2229 mm^2 for triangular-CH at AR 1 and 0.5; quadrilateral-CH and oval-CH each at AR 1, 0.5, 0.33 and 0.25.

Young's Modulus, yield stress, Poison's ratio and contact angle for parabolic-CH were 22.29±0.02 GPa, 222.50±0.25 MPa, 0.42±0.02 and 30.25±3.50º, respectively. At IP of 0.3 and 0.15 MPa, experimentally obtained stresses at well, IBS and OBS were 6.29±1.52 and 4.47±1.05; 5.45±0.91 and 4.14±0.93; 4.86±0.21 and 3.56±1.63 MPa, respectively. Corresponding FEM results at well, IBS and OBS at 4750 N loading at IP of 0.30 and 0.15 MPa were 6.75±2.82 and 4.68±0.05, 5.33±1.15 and 2.78±1.36, and 2.50±0.33 and 1.50±0.45 MPa, respectively. The FEM and experimental results had no significant difference. Numerically obtained stresses at well, IBS and OBS at 4750 N loading and IP of 0.3 MPa were 4.96±1.24, 4.83±1.24 and 2.00±0.82 MPa and

4.76±0.74, 4.69±1.26 and 1.91±0.90 MPa, respectively for quadrilateral-CH and oval-CH. Numerical inboard stresses at AR of 1 and 0.5 for triangular-CH were, respectively, 5.59±1.50 and 5.84±1.86 MPa. Inboard stresses at AR 1, 0.5, 0.33 and 0.25 for quadrilateral-CH were 5.56±1.18, 5.08±1.30, 5.01±0.45 and 4.49±1.26 MPa, respectively; for oval-CH, 4.46±1.40, 4.37±1.14, 4.63±1.04 and 4.37±1.44 MPa, respectively.

The study established that oval-shaped cooling-hole aluminium alloy wheel possessed highest structural integrity than all others investigated.
Keywords: Aluminum alloy wheel, Cooling hole geometry, Aspect ratio, Structural integrity.
Word count: 482

ACKNOWLEDGEMENTS

I wish to express my profound gratitude to God having gone this far. He has been very gracious and merciful to me. I am most indebted to my supervisor, Dr. D. A. Fadare for the concern, push and doggedness in ensuring that this work comes to fruition. He is a result oriented. I wish to also appreciate Professor P. O. Aiyedun for his query. He would always ask, anytime he sees me: 'Igbudu when are you going to round up?'. At a point, I became shy. His query propelled me further. I thank all the Lecturers and other administrative staff of Mechanical Engineering Department, University of Ibadan for their encouragement support and contributions, especially Dr Dare for his painstaking efforts towards the success of the work. I thank my parents, Late Mr. Ovedhe Igbudu and Mrs. Maria Igbudu; My wife, Omonigho Igbudu and my son (my chairman) Maxwell Igbudu and other members of my family for the love and care, most especially, Late Mr Gordon Igbudu and Mr. Michael Igbudu. They both contributed immensely to my upbringing when I lost my father at my formative age. I also wish to express my gratitude to Mr, Frank Uwalaka and Mr. Dennis Akhagbosu who always make my stay in Ibadan a memorable one. My thanks go to my colleagues in the office for their encouragement. I thank the management of Ambrose Alli University for giving me the opportunity to undertake this programme. I appreciate TEDFUND for the financial assistance during the course of the programme. I also appreciate Engr Dr N. Ehigiamusoe for the role he plaid in the procurement of the instruments used. I thank Engr Girrald, the laboratory and workshop staffof the Faculty of Engineering and Technology, Ambrose Alli University, Ekpoma and Faculty of Technology, University of Ibadan for their technical support.To those who in one way or the other contributed to the success of the programme, but whose names have not been mentioned, I say thank you.

DEDICATION

This work is dedicated, first and foremost, to the Almighty God, our Creator; my parents, Mr. Ovedhe Igbudu and Mrs. Maria Igbudu; My wife, Omonigho Igbudu and my son (my chairman), Maxwell Igbudu.

Table of Contents

List of Figures

List of Tables

List of Plates

NOTATION

SYMBOL	MEANING
F, F_r, W,	Radial load of tyre load
R, r, r_b, r_f	Bead seat radius
K	Acceleration factor
M_b	Bending moment
F_l	Lateral load
μ	Coefficient of friction
d	Wheel's width
FEALAB	Finite element laboratory
NASTRAN	NASA Structural Analysis
ALGOR	Finite Element Software
SAE	Society of Automotive Engineers
FE, FEA	Finite Element Analysis
3 - D	Three dimensions
ABAQUS	Finite Element Software
ASWAL	Axisymmetric Solids with Arbitrary Loading
ADINA	Finite Element Software
ANSYS	Finite Element Software
CATIA	Finite Element Software
IGES	International Graphics Exchange Specification
PBC	Pressure Back Calculation
BC	Boundary Conditions
q	RadiaL load distribution
θ, θ_1	Loading angle
dl	Elemental rim length
dθ	Elemental distributed angle
U	Strain energy
H	Dummy load
a	Tyre radius

W_p	Axial tyre force
P, P_o	Inflation pressure
T_f	Tyre force
ε_x, ε_{ee}	Strain in the x - direction
ε_y, ε_{yy}	Strain in the y - direction
ε_z, ε_{zz}	Strain in the z - direction
σ_x, σ_{xx}	Stress in the x - direction
σ_y, σ_{yy}	Stress in the y - direction
σ_z, σ_{zz}	Stress in the z - direction
σ_{xy}	Shear Stress in the x - y plane
σ_{yz}	Shear Stress in the y -z Plane
σ_{zx}	Shear Stress in the z - x Plane
ε_{ey}	Shear Strain in the x - y Plane
ε_{yz}	Shear Strain in the y - z Plane
ε_{zx}	Shear Strain in the z - x Plane
u	Displacement
NA	Numerical analysis
90 deg EBF	90 degree Eye-bar function angle
40 deg CF	40 degree Cosine function angle
ECA	Experimental Contact Angle
Tri-CH	Triangular cooling hole
Quad-CH	Quadrilateral cooling hole
Oval-CH	Oval cooling hole
AR	Aspect ratio

CHAPTER ONE
INTRODUCTION

1.1 Background

A wheel is acircular frame or disc arranged to revolve on an axle, as in vehicle or machinery (www.dictionary.com). Automobile wheels are vital structural members of the vehicular suspension system that sustainboth static and dynamic loads encountered in operation (Mohd, 2011). As a key safety component, the designs of wheels are by and large governed by aseries of international standards and codes such as the British Standards Institution and the Tyre and Rim Association (Carret*et al*, 2000).Automobile wheels have evolved,with time, from early spoke designs of wood and steel wheels to flat steel discs, stamped metal configurations and the newer generation of cast and forged aluminum alloy wheels(Stearns, 2000). The need for enhanced safety, fuel economy and global concern for a decreasein emissions of greenhouse gas are the most important factors driving the automobile industry in their efforts to reduce weight of vehicle in order to improve the fuel efficiency. The switch from steel to aluminum alloy wheels have been reported to reduce weight fuel efficiency up to 50%, and 16%, respectively (Wimmer and Peterson, 1979).

The four main technical issues related to the design of new automobile wheels are style, weight, manufacture and performance (Tonuk and Samim, 2001; Carvalho *et al*, 2001; Kouichi and Ryoji, 2002). Figure 1.1 shows the wheel characteristics based on style,weight, manufacture and performance.

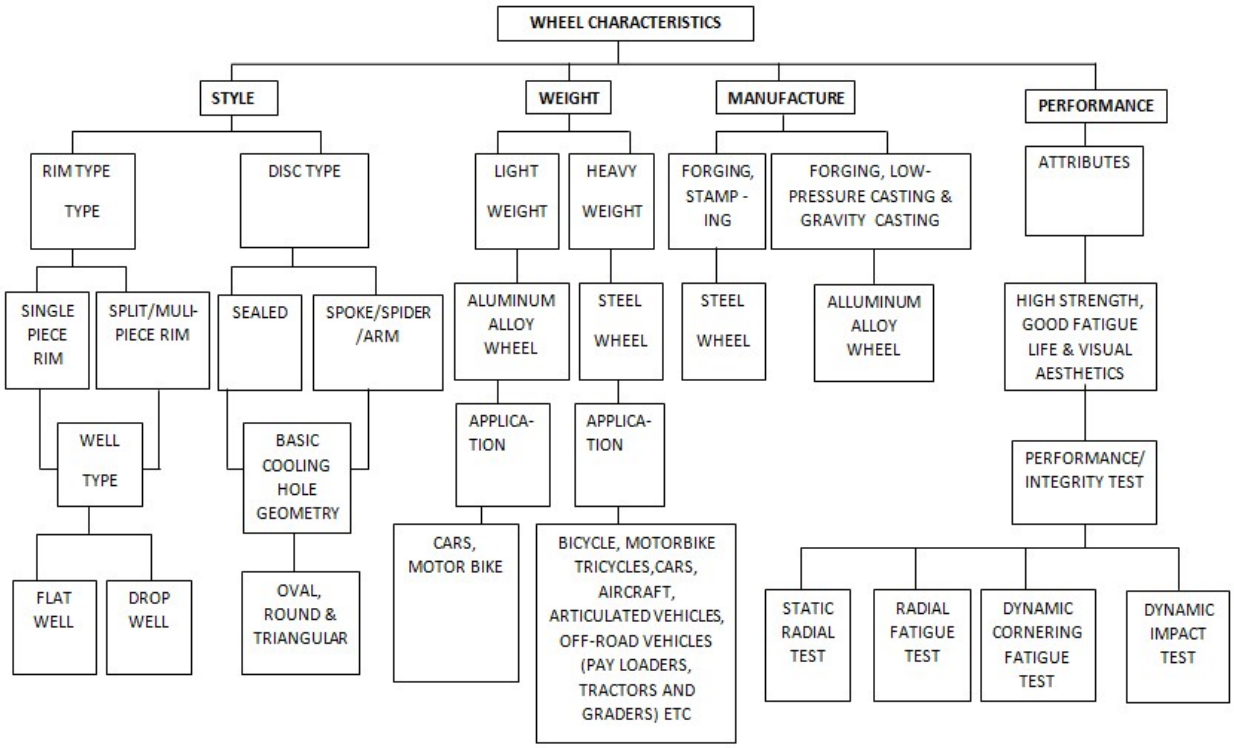

Fig. 1.1: Block diagram of wheel characteristics *(Carvalho et al, 2001)*

According to the Society of Automobile Engineers (SAE) specification, a wheel should maintain structural integrity without any cracks or plastic deformation for more than 4 x 10^6 revolutions under a radial load (Tonuk and Samim, 2001; Baeumeland Seeger, 1990).

Modern automobile wheels are generally of disc type. The part of the wheel where the tyre is fixed is called the rim, the discis the perforatedpart, which transfers force from hub to rim (Stearns, 2000)

1.2 Features and Nomenclature of Modern Automobile Wheel

The main features and nomenclature of typical modern automobile wheel is shown in Figure 1.2. Based on the figure, the basic features are:

- The wheel hub is the part of the wheel attached to the vehicle.. This part has bolt holes to ease in the fastening of the wheel to the vehicle.
- The wheel disc or spoke is the part of the wheel that connects the rim to the hub, whichtransfers all the loads between the hub and the rim.
- The rim flange or lip is the portion of the wheel that retains the tyre and also protects the wheel against impact loads. The tyre bead is incorporated in this area.
- The hump ensures that the tyre stays within the wheel flange in deflection conditions.
- The rim well facilitates assembly and disassembly of the tyre.
- Rim width - The distance between bead mounts (where the tyre is attached to the rim)
- Centerline - The centre line is the line passing through the mid span of the rim's width..
- Offset - This is the distance between the centerline and the wheel mounting pad (Offroaders, 2012)

1.3 Wheel Markings

Markings are placed on the outside of the wheel to indicate the basic numerical features of the wheel (www.tyresizescalculator.com, 2015). For the wheel used, that is,6 J x 14 H2 ET 42, the meaning of the alphanumeric features are:

- 6: Indicates the inner width of wheel in inches
- J: Indicates the shape of the wheel on the place where the tyre bead sits on the wheel
- x: Indicates that the construction of the wheel is one-piece
- 14: Refers to the nominal wheel diameter in inches
- H2: Type of wheel flange. wheel flange is a bulge on the wheel in the place where the tyre bead lies on the wheel. it prevents the tyre from falling inside of the wheel
- ET 42 : ET is the offset, that is the distance between the centreline of the wheel and the plane of the hub-mounting surface of the wheel. The offset is measured in millimetres and can be positive or negative. in our case it is positive. ET 42 means the offset of the wheel is 42 mm.

1.4 Classification of Wheels

Generally wheels are classified according to their configuration (offset) as central, inset or outset as illustrated in Figure 1.3(Carret*et al*, 2000). The different rim sections of automobile wheel are shown in Figure 1.4.

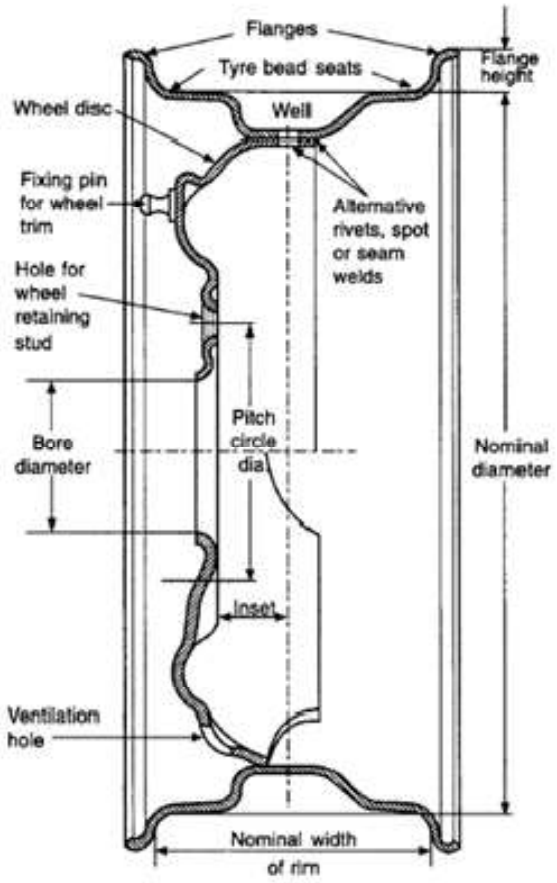

Fig. 1.2: Nomenclature of modern automobile wheel(Carret *et al., 2000*)

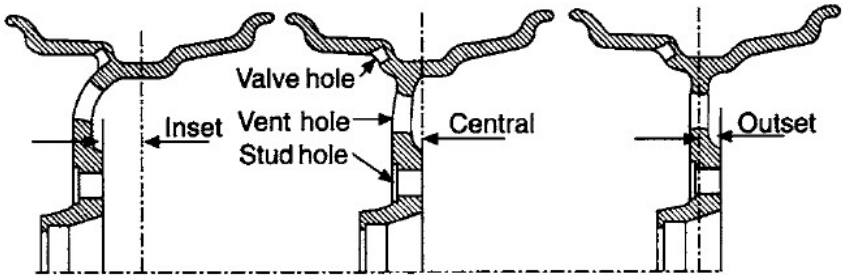

Fig. 1.3: Automobile wheel configurations. ***(Carret et al, 2000)***

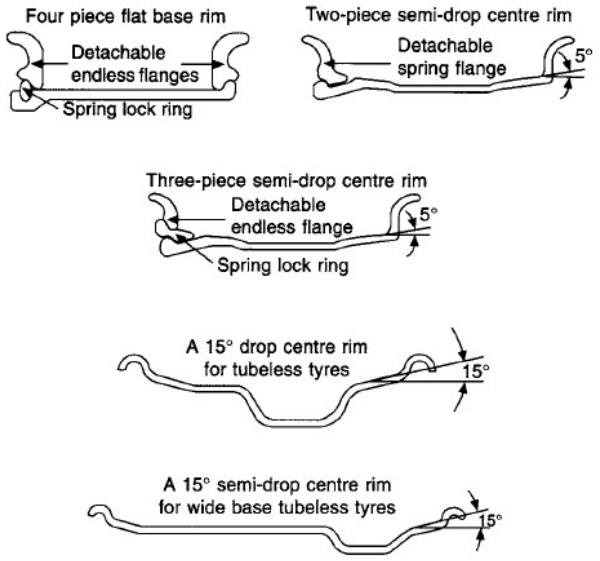

Fig. 1.4: The different rim sections of automobile wheel (Carret *et al*, 2000)

The design of wheel is becoming more intricate and whatever the design, it should fulfill the design criteria forlight weight, high strength, good fatigue life and visual aesthetics (Li *et al.*, 2006).Alloy wheels are light in weight, thus, enhancing steering and fuel economy; good conductors of heat which improves heat dissipation from the brakes, thus, reducing the chances of brake failure and adds beauty to the car. These features differentiate alumium alloy wheels from steel wheel(Shang*et al*., 2004; Blake, 1990; Xiaofeng and Xiaoge, 2010).

In order to improve the performance of wheel, its structural integrity in terms of stress and strain induced, fatigue life are of paramount importance in wheel design. Automobile wheels are safety related components which are highly stressed when loaded. The loading which is complex in nature could lead to failure if not applied correctly.The aftermath of a wheel failure is too serious to be ignored, as this could lead to unquantifiable degree of fatality. Some of the factors ascribed to the frequent fatal accidents include, bad road network, poor driving culture, night trips, overloading, dangerous driving, poor vehicle maintenance (Nigerian Pilot, 2016).

Damage to the wheel could cause vibration and inability of the tyre to retain pressure, instability and even complete structural failure (Torgaland Misshra, 2012). Since the wheels on which cars move, are the most vital elements in a vehicle, they must be designed carefully (Vijay and Mouli, 2015)

Fatigue performance and the state of stress in the wheel under various loading conditions are prime concerns in wheel design. Successful designs are usually achieved after several years of experience and extensive testing (Wimmer and Peterson, 1979), thus making the process of wheel design cumbersome, costly and time consuming. Hence, to meet the increasing demand of modern manufacturing systems, some innovative methods of testing and experimental stress measurements have been developed and applied (Kruse and Mahning, 1976). The procedures have been enhanced by anarray of analytical, experimental and numerical methods (Stearns, 2000; Raju et *a*l 2007; Muhammet, 2010; Li et *al* 2007a).The ground-breaking efforts are dated to the mid 1970s and were mostly analytical and empirical analysis of impact strength and dynamic tests, largely on steel wheels and, lately, on aluminum alloy wheels(Wimme and Peterson, 2014).

a

b

Plate 1.1 (a & b): Picture of damaged wheels (www.Santaanawheels.com)

1.5 Statement of Problem

The need for improved safety, fuel economy together with the global efforts in reducing greenhouse gas emissions are undeniable factors driving the automobile industry in their efforts to reduce weight of vehicle for improved fuel efficiency. Aluminium alloy wheels are becoming increasingly popular for their light weight, good thermal conductivity and aesthetics. However, the search for light wheel is still ongoing and has led to introduction of cooling hole in wheel design without compromising its structural integrity .Varieties of cooling holesare mostly of parabolic or circular geometry. Literature is sparse on the use of triangular,,quadrilateral, and oval shaped cooling holes in wheel design. This study is therefore, designedto investigate the structuralintegrity of an aluminium alloy wheel with selected cooling holes under static loading condition.

1.6 Aim

The aim of the study was to investigate the structural integrity of a selected automobile aluminum alloy wheel with selected cooling hole geometry..

1.7 Objectives of Study

The specific objectives are:

1. Determination of the mechanical properties (Yield stress, Poison's ratio, Young's modulus etc.) and chemical properties (chemical composition) in other to determine the structural integrity of the wheel.
2. To investigate experimentally and numerically the combined effect of radial load and inflation pressure on the mechanical response of the wheel under static loading condition of radial load and inflation pressure.
3. To carry out a numerical study of the wheel based on the results obtained on selected cooling hole geometries.

1.8 Scope of Work

1. The wheel analysed is a selected automobile aluminium alloy wheel, with ISO designation (6JX14H2; ET 42) andTyre of 175/65 R14 (Max. Load, 4750 N; Max inflation pressure, 0.3 MPa) .
2. The loading is limited to the joint effect of both the radial load and inflation pressure
3. Two loading regimes are used in order to have a good basis of comparison between experimental and numerical results

1.9 Justification of the Work

Automobile wheels are critical safety related components and when loaded undergo internal stress, strain and displacement in the vertical plane. The state of the wheel depends on the magnitude of the load.The overriding need to maintain the structural integrity of the wheelat all times cannot be overemphasized.This to avoid damage to the wheel which could cause a reduction or a complete loss of inflation pressure in service.Apart from loss of inflation pressure, deformed wheels could lead to vibration, instability and complete structural failure of the wheel. This study assesses the effect of the combined effect of radial load and inflation pressure on an automobile aluminium alloy wheel.

CHAPTER TWO
LITERATURE REVIEW

2.1 Experimental procedures for structural analysis of automobilewheels

Mechanical performance of road wheels under normal or severe driving conditions is evaluated by using standard methods, such as static radial, radial fatigue, dynamic rotary (cornering) fatigue and dynamic impact tests. The rotating bending test simulates cornering induced loads by applying a constant rotating bending moment to the wheel (Muhammet, 2010). The load on a vehicle's wheel is a combination of the radial load and inflation (air) pressure. The radial load is made up of the vehicle's unladen weight (weight of the vehicle when it is not carrying any passengers) plus the passengers' weight including goods (www.gov.uk/vehicle, 2017; www.//en.m.wilkipeadia.org, 2017).

2.2 Static Radial and Axial Test

This test is used to examine the influence of static radial loads due to vehicle weight, passengers' weight and axial load due to tyre inflation pressure on the displacement, stress, and strain distributions of the wheel. The wheel may undergo excessive displacement, stress and strain that may lead to failure of the wheel as a result of the static loading condition. The effects of the state of loading are commonlyexaminedat specific points of interest on the wheel such as: the contact of tyre with the ground; outboard and inboard bead seats; rim hump; disk hat; outer pad; and the well. Strain gauges are planted in these points of interest on the wheel to measure the strain distribution(Stearns, 2000). A typical experimental setup for static radial and axial test is shown in Figure 2.1.

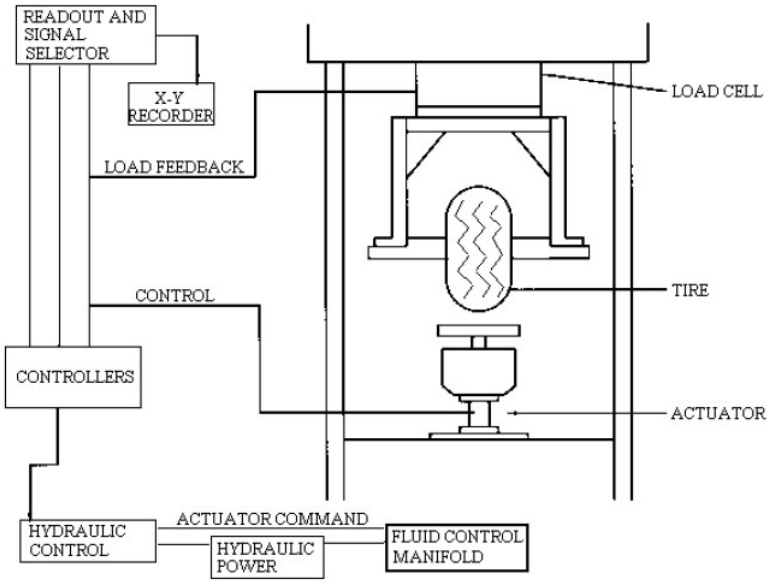

Fig..2.1: Typical experimental setup for static radial and axial test(Stearns, 2000)

2.3 Dynamic Impact Test

Thisis used to assess the impact performance. It simulates a situation where the wheel collides with the curb of the road or a large obstacle.in which the striker is dropped from a specified height above the tyre–wheel assembly. The test is to evaluate the frontal impact resistance of wheel and tyre assemblies used in all cars and multi–purpose vehicles (Muhammet, 2010; Raju, Satyanrayana*et al,* 2007). A typical experimental setup for dynamic impact test is shown in Figure 2.2. The wheel is visually inspected before the test to make certain that no cracks exist. For a successful test, the wheel must satisfy minimum performance standards, viz:there will be no visible fracture of the central member of the wheel assembly, no separation of the central member from the rim, no sudden loss of tyre air pressure and deformation of the wheel assembly, or fracture in the area of the rim section contacted by the faceplate weight system do not constitute a failure (International standard, 1995). Impact load is applied to the wheel-tyre assembly by a striker as shown in Figure 2.2. The wheel ispositioned with its axis at an angle of 13 degrees (± 1 degree) to the vertical, so that its highest point is presented to the vertically acting striker. The impacting face of the striker is at least 125 mm wide and 375 mm long. The freely dropping height of the striker is 230 mm (± 2 mm) above the highest point of the rim flange. The striker is placed over the tyre and its edge overlaps the rim flange by 25 mm. The inflation pressure of the tyre can be specified by manufacturer taking into account, the serves conditions(Raju*et al*,2007).

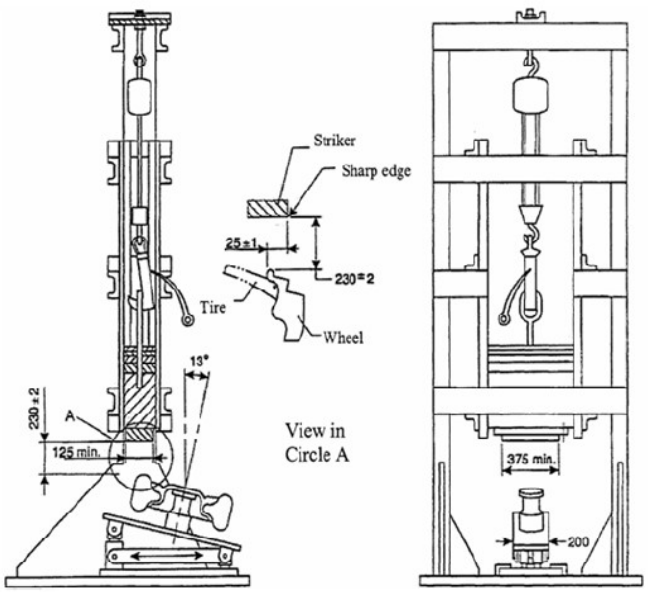

Fig.2.2: Typical experimental setup for dynamic impact test(Muhammet, 2010)

2.4 Dynamic radial fatigue test

This test is used to simulate a condition where the wheel-tyre assembly runs on a smooth road surface. A typical experimental setup for dynamic radial fatigue test is shown in Figure2.3.While the wheel is rotating, the radial load becomes a cyclic load. The test is terminated when the wheel in questionhas complete the minimum number of test cycles, loss of inflation pressure through a fatigue crack or the inability of the wheel to sustain the test load. Failure of the tyre or other parts of the test fixture does not necessitate test termination, but may result in damage to the wheel and test invalidation (JISD, 1989; Kocabicak and Firat, 2001). A wheel should maintain structural integrity without any cracks or plastic deformation for more than 10^6 cycles (Wimmer and Peterson, 1979; Kocabicak and Firat, 2001) under a radial load Fr, expressed by the following equation,

$$Fr = F \times K \qquad (2.1)$$

where K is acceleration test factor (K = 2.2) and F is the maximum tyre load in N.

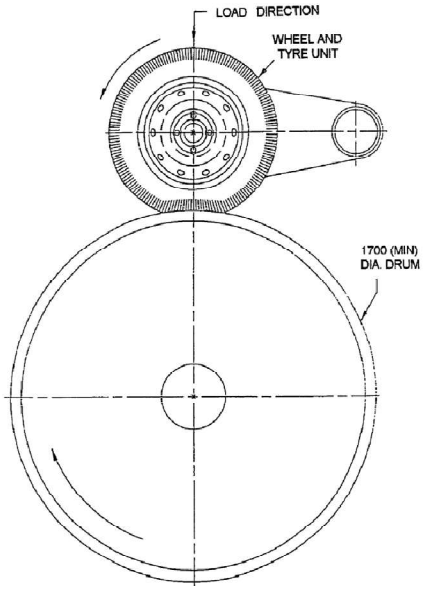

Fig.2.3: Typical experimental setup for radial fatigue test(Kocabicak and Firat, 2001)

2.5 Cornering Fatigue Test

This simulates the dynamic loading of the wheel during cornering on the road. It is used for modelcertification. Figure 1.8 represents a typical experimental setup for cornering fatigue test. The forces acting on the wheel are a combination of the vertical load and lateral force between tyre and ground. The two components of loading result in a rotating bending moment on the hub of the wheel. The bending moment is calculated as(Chia-Lung and.Shao-Huei, 2009)

$$M_b = F_R d + F_L R \quad (2.2)$$

$$F_L = \mu . F_R \quad (2.3)$$

2.6 Application of Numerical Techniques In Structural Analysis Of Aluminum Alloy Wheels

Finite element analysis is generally used in numerical methods for wheel design. NASTRAN, generally, has been used in series of finite element analysis on aluminum alloy 545 in the fatigue design (Reipert, 1985; Mizoguchi *et al*, 1982). The analytical stress and fatigue life were in good agreement with the result of a rotary cornering fatigue test. (Rhinda, 1976) did a finite element study of a rim section to determine the varying stress patterns using tetrahedral elements. (Fadare*et al*, 2011), investigated the combined effects of static load due to varying automobile weights and tyre inflation pressures on the total deformation and stresses of an aluminum alloy automobile rim using a commercially available 3-dimensional finite element model in FEALAB® 3.0. The effects of the loading condition were investigated at the point of contact of tyre with the ground; outboard and inboard bead seats; and the well.

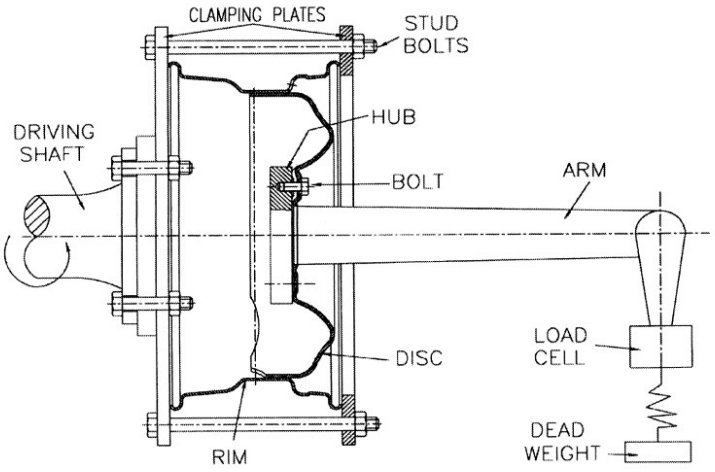

Fig.2.4: Typical experimental set- up for cornering fatigue test (Chia-Lung and.Shao-Huei, 2009).

In predicting the natural frequency and wheel geometry with weight as the basic parameter using, NASTRAN, the result showed that the lowest first mode natural frequency was greater than 230 Hz (Wood *et al*,2011). This was by adding weight until the natural frequency was reached. (Ferreira, 1992) modeled a rim with eight node brick elements using the ALGOR finite element system. An extremely high margin of safety was achieved after several design modifications were made to the model. The final design which met the minimum life requirements of 2,320,000 cycles, performed extremely well in the fatigue tests.

Mohd (2011) in his work used the analogy and analysis from thick ring theory in the development of loadings on links and eye-bar. Results show that the loading shape is in the form of a cosine function about a central angle of about 30^{o} from either side of the point of contact with the ground. The angle is assumed to be formed from the contact patch geometry of the tyre.The length of the flat portion of the tyre in contact with the ground when the tyre is loaded is called patch, and the length of this patch is then converted to an angle swept by the bead seat area in contact with the rim called the contact angle. (Mohd, 2011; Stearns, 2000).

Sourave (2014) used Finite Element analysis to simulate radial fatigue and damage amalysis for weight optimisation of aluminum alloy wheel. Results showed that a weight reduction of about 50% was achieved when compared to steel wheel and that damage on the wheel was about 0.2% in the flange region.

Weight reduction in wheels without compromising fatigue resistance and other mechanical properties was examined by Gergele (1983) using finite element methods based on design optimization were developed in order to try to find the right thickness and best design that would guarantee minimum weight.

Mohamed *et al*, (2017) studied a parametric model of Al 356.2 and ZK60A alloy wheel rims with radial and spiral flexures, respectively.CREO was used in the design, while analysis was by ANSYS. Results showed that Al 356.2 and ZK60A with spiral flexure offer greater resistance to stress than radial flexure.

Jitendra *et al*(2017) reviewed the effect of various materials on fatigue life of the automotive wheel rim by using finite element analysis and radial load testing. Modeling of the wheel was with CATIA and imported into ANSYS for analysis.

Panithi and Abhilash (2016) gave a detailed static and fatigue analysis of A356.2 aluminum alloy wheel using Finite Element analysis. CATIA was used in designing the 3 dimensional model of the wheel and the IGES (international graphics exchange specification) format was imported into ANSYS for analysis to determine the life, safety factor and damage of alloy wheel and corresponding deformation, shear stress and alternative stress. They assert that it is essential to validate numerical analysis results with experiment.

In the recent technological advancement, considerable attempts are being made to develop Al and Mg alloy wheels bearing in mind factors such as strength to weight ratio, low cost and better fuel consumption Razak (2015). Most aluminium alloy wheel manufacturing companies carry various test on their products, but method of testing is always limited(Nallusamy *et al*, (2015).

Raju *et al*(2009) simulated rotary bending fatigue test at different stress levels on aluminium alloy (Al) A356.2. Results showed that cracks were initiated at the joint between the arm and the hub, closer to the spanner hole on the wheel' outboard, while the wheel mounting face experienced maximum stress.

Mattia *et al* (2009) studied the effects of microstructure on an A356 17-in aluminium alloy wheel using impact strength. Results indicated that the impact energy was higher in T6 heat-treated wheels than as-cast wheel.

2.7 Application of Both Numerical and Experimental TechniquesIn Structural Analysis of Aluminum Alloy Wheels

Stearns (2000), in modeling the state of stress and displacement in aluminum alloy rim, by employing the static radial test. The magnitude of the stress, strain and displacement were determined via finite element software, ALGOR. The experimental set-up involves three basic steps: (1) measurement of surface strains with strain rosette. (2) Conversion of measured strains to principal strains and (3) conversion of principal strains to von Mises stresses. He concluded that the bead seats and the rim's well are the most critical regions for a wheel subjected to static loading condition.

Raju et al(2007) estimated the stress distribution and fatigue life of aluminium alloy wheel by conducting a destructive tests under radial fatigue load and compared same

with that of the finite element analysis. Ten wheels were tested on radial fatigue testing machine . The test was conducted in two stages. The wheel wasfirst inspected after 10^6 cycles for visible cracks and test terminated if cracks develop, otherwise it would be continued up to 1,500,000 cycles. Initiation of cracks started between 1,050,000 and 1,300,000 cycles and all wheels were found to have cracks after 2,500,000 cycles. The finite modeling and analysis was carried out using finite element software, ANSYS and, since the angle of application of load in circumferential direction to which actual contact takes place cannot be decided exactly, analysis was carried out at different angles starting from 40^o to 90^o and the results were compared with those of the actual durability test performed in earlier experiment. The next step of analysis was carried out at circumferential loading angle from 0–40^o to0–90^o with different safety factors 1, 1.5, 2 and 2.5.Results demonstrated that the location of crack initiation in both experimental and the finite element analysis (FEA) were in good agreement.

Muhammet (2010) applied numerical simulation of dynamic side impact test on an aluminium alloy wheel using 3-D explicit finite element methods. The result showed that the lug region of the wheel experienced most stress. This is as a result of geometrical complexities and irregularities occasioned by the hole in the lug region. The aluminium specimen used was A356 alloy that is widely used in automobile industries. Commercially available finite element ABAQUS/explicit code was used for the 3-D dynamic analysis.

Li *et al*(2007b)used the through process modelling methodology to predict the fatigue life of A356 automobile wheel subjected to bending fatigue. The through process methodology includes: (1) casting, (2) heat treatment, (3) machining, (4) in-service loading and (5) performance prediction. The cyclic elastic strains measured on the wheel surface for a series of different bending loads were in agreement with the predictions. The crack initiation location and number of cycles, as predicted, to cause failure were in agreement with fatigue test on the wheels. Earlier studies have established the viability of the through process modeling methodology, validating separately the casting and residual stress and fatigue (Li et al, 2007b;Zang *et al*,2007; Yi *et al*, 2003).

Reipert(1985) and Mizoguchi(1982) carried out fatigue analysis by employing the use of NASTRAN. Assessment of the wheel performance as a function of the rim and disc thickness was carried out. The analytical resultof stress and fatigue life was in good

agreement with that obtained for rotary cornering fatigue test. Cerit (2010)carried out an experimental and numerical simulation of dynamic impact loading of cast aluminum alloy wheel owing to collision with the curb of the road or large obstacle. The result obtained showed that the maximum stress occurred in the lug region of the bolt hole as a result of geometrical complexities, which was also reported by Muhammet (2010). In the study of different size wheels using ABAQUS and emperical analysis, results with good agreement were obtained (Konishi *et al*, 1996).Results from further works showed that stress concentrations occurred in the spoke area of the rim and cracks formation began in these areas(Woods. 1988; Mizoguchi *et al*,1982; Liangmo *et al*,2011; Stearns *et al*,2003).

Stearns *et al*(2003) modeled the mechanical response of an aluminum alloy automotive rim-tyre combination. They assert that the air pressure is constant load and has little or no relation to rotation of automobile wheel unit. High inflation pressures tend to increase the stress by about 25% in certain critical locations on the rim. A decrease in inflation pressure lead to an increase in displacement of the rim. This is because the circular geometry of the wheel is retained by the air pressure. When the air pressure is released, the rim tends to elliptical about the point of loading(Stearns et al, 2003).

Janardhan *et al*(2014) carried out both experimental and numerical radial fatigue analusis on alumium alloy wheel. The experimental analysis was carried out on a test bench, while the numerical analysis was implemented with ANSYS.Results obtained were further analysed with fatigue module to determine the life of the wheel.

Yang *et al* (2013) presented a study on the effects of casting defects and optimisation on aluminium alloy wheels by numerical simulation and analysis of uniaxial tensile test of the defected wheels. The inference drawn from both empirical and simulated results was that tensile strength increases with increase in defects due to the presence of impurity.

Borase and Deore (2016) studied the effect of pressure on rim by simulating radial fatigue test experimentally and numerically (using ANSYS) with constant inflation pressure and varying loads. With a load increase of between 20% and 33%, the maximum Von-Mises stress value increased by between 13% and 26%.

2.8 Application of numerical techniques in structural analysis of steel wheels

Mehemet et al (2009)applied a numericalapproach which depends on the local strain concept and linear elastic finite element analysis for fatigue destructive analysis of metallic components under elastic and non-elastic loading states. The simulation wascarried out in two steps viz: a global analysis for all material points on the wheel's surface and a local analysis at the most critical damage areasidentified in the global analysis. The tyre-wheel interaction was not considered. linear elastic finite element analysis was implemented using ANSYS. The mechanical stresses on the wheel were considered viz: the stress due to manufacturing; pre-stress on the wheel due to the assembly with other components, mainly on the disc region due to bolt penetration and on the rim due to tyre inflation pressure and the dynamic loading stresses caused by vertical wheel force, cornering force with the wheel alignment and the centrifugal force due to the rotation of assembly.

Topac *et al*(2012) predicted the fatigue life of a heavy vehicle steel wheel under radial loading condition by the use of finite element analysis. In order to analyse failure, a full scale numerical model of the wheel was generated and loading condition of the test bench simulated using ANSYS workbench v12.0. Initiation of crack was said to have occurred at the most stress concentrated regions of the air ventilation holes which are the critical regions of the wheel.

Xiaofeng and Xiaoge (2010) sought a total and practical method of simulating the dynamic cornering fatigue test of a steel passenger car steel wheel. The simulation was implemented by the combined use of linear transient dynamic finite element analysis and the local strain approach. It was established that only a radial component of the rotating force is needed to obtain the amply accurate radial normal strain histories of the elements located along the radial direction. The bolt connections were not modeled for simplicity and the fact that comparatively small number of failure occurred at the bolt circle areas in the real dynamic cornering fatigue tests of the wheel studied.

Kocabicak and Firat (2001) carried out numerical analysis of wheel cornering fatigue test in a program called ‘Metal Fatigue Prediction and Analysis (MFPA)with the ain of predicting the accumulated number of cycles at which a small crack (such as 0.5mm for mild steel) are detected. The stress distribution in the wheel was a function of the mode

of operation and the stress at any point in the wheel was made up of pre-stresses (stress due to the manufacturing process, tyre pressure and assembly to the hub) and service stresses (the wheel loads which are the vertical force composed of static load due to the vehicle weight and dynamic forces developed passing road irregularities such as potholes when driving straight, the lateral force due to the quasi-steady cornering forces as the most important ones. The longitudinal forces developed during breaking and acceleration as well as the wheel aligning moments are considered to be of secondary importance). Highly stressed region in a disc type wheel are the rim well, weld zone between disc and cooling holes, bolt contact area and hat radius, (Kocabicak and Firat, 2001; Topac *et a*l, 2012; Wang *et al*, 2009).

Wright (1983) and Kawasshima and Ishihara (1989)employed the finite element method to simulate the dynamic effects of rolling, cornering and breaking loads in steel rims. Results showed that the actual load on the tyre–rim unit assumed a cosine function having a central angle of about40^{o}measured from either side of the point of contact with the ground (Shang and Altenhof, 2005; Dowling, 1982; Currie, 2000; Morita and Sumimoto, 1987; Morita *et al*,1989; Morita *et al*, 1987).In dealing with fatigue strength under cornering fatigue test during driving, strength and the critical region for fatigue crack initiation were influenced by the shape of the design (Tanaka *et al*, 1987)

Wubin *et al*(2011)worked on a simplified stress analysis of large-scale harbour machine's. To establish the response of the wheel subjected to radial load, a similar model was developed and analysed using finite element analysis which gave results of the stress and displacement distribution. The results were further confirmed by testing the numerical model under different pressure. The pressure distribution with spread angle of 60^{o} was adopted in the finite element modeling and the results analyses showed that this method wasconsistent and of use.

Thomas and Nair (1983) predicted the stress level of a 36inches (916mm) diameter freight car wheel subjected to cyclic thermal loads in the presence of mechanical and cyclic mechanical loads by the use of elasto-plastic finite element analysis using ASWAL (Axisymmetric Solids With Arbitrary Loading) software. Fatigue life were predicted based on the stresses and strains computed via the loading conditions. High stresses were developed at the inside plate near the rim at the tread. The elasto-plastic wheel analysis

that had been done had many shortcomings. In some of these analyses, the wheel models were over-simplified and were rather poor representations of the actual wheel.

Sherwood *et al*(1995) investigated the tyre-wheel interface loads of an aircraft wheel using ADINAl. The investigation was limited to the tyre-wheel interface pressure. Under static loading condition the wheel deflects and, these deflections wereemployed in ADINA version 6.1.4 model of the wheel by load displacement command to apply a displacement field on the wheel. The procedure also avoid the need for the tyre to be modeled. Only the boundary conditions (BCs) associated with the static loading of the tyre-wheel assembly due to inflation pressure were investigated.

A successful durability test is a pre condition for accepting procedure for wheel in fatigue evaluation in both radial fatigue and the dynamic cornering tests(Shang *et al*, 2008; ISO 3006, 1976). In addition to these test, a biaxial wheel fatigue test machine was designedto perform the combined radial and lateral cyclic loading to simulate the loads on road more accurately (Gribisic and Fisher, 1983; Richard and Rice, 1988; Fancher, and Bareket, 1993; Wright, 1999;) . Early assessment of mechanical components to ascertain the durabilityis necessity in the design stage of wheels.This is usually accomplished using prototype tests by simulating the actual service conditions (ISO 3006, 1976). An understanding of fatigue failure mechanisms under multi-axial loading conditions is still a practical need that proposes design and material variation against active damage(Richard and Rice, 1988; Wright, 1999). Computer modeling and simulation of multi-axial fatigue process is cost effective andreduces iteration sequence during product development and refinement process(Gribisic and Fisher, 1984; Chu *et al*, 1993). The simulation modeling for fatigue failure of metallic structures may follow different methodologies depending on the type of the application and available experimental data characterizing the fatigue damage process (Firat and Kocabicak, 2004). Resaerch papers which deal with the simulation of the dynamic cornering fatigue tests of automotive wheels have been published (Riesner and.'DeVries, 1989; Karandikar and Fuchs, 1990) but generally do not provide ample details for others to follow and make the simulation (Stearns, 2000).

Investigation of the tyre rim interface under radial loading conditionsto determine the effect of air pressure variations on the tyre-rim interface was carried out by Tsang

(1989) and Jeusette (1992).The conclusion was that when inflation pressure is halved the induced stress is reduced by the same magnitude.

Noda (1982)carried out a research work that entailsoptimizing weight to reduce fuel consumption in Japanese bus and truck vehicles. His conclusion was that about 30% weight reduction in aluminum alloy rims for trucks and buses could beachieved. A method for the design of railway wheels, which is based on the use of the semi -analytical finite element method was proposed. The method accounts for both the forces of contact interaction between the rail and the wheel (Esaulov and Sladkovskii, 1991).

Ramamurti and Srinivasan (1981) dealt with the static stress analysis of the web portion of the rimby assuming the rim as a ring; the hub rigidand the disc as a round in plane stress conditions.

Leslie (1986) developed an analytical model to predict the lateral forces acting on the tyre under various loading and soil conditions and travelling at an angle to the centre plane.

Landgraf*et al*(1994) studied fatigue performance using a finite element model. The use of analytical and experimental methods gave an idea of wheel fatigue performance under laboratory and simulated conditions.. Hahn *et al*(1984)employed the use of theory of elasticity to analysis of rolling contact fatigue and fracture.

2.9 Application of Experimental Techniques In The Structural Integrity of Steel Wheels

Wang et al (2009) examined the fatigue property of low cost and high strength wheel for commercial vehicle by simulating the dynamic cornering fatigue test (cornering of the wheel on the road). Initiation of cracks were noticed at the cooling holes and bolt holes regions. Fatigue life is influenced by the number and shape of cooling holes.

2.10 Limitations of Structural Analysis of Automobile Wheels

i. Due to the complex nature of tyre-rim and tyre-ground interactions, it is difficult to model accurately the forces acting on the wheel. As a result simplifying assumptions are made in order for the model to be achievable(Stearns, 2000).

ii. It is difficult to assess fatigue life by using analytical methods.

iii. The bolt connections are not usually modelled for simplicity in both static and dynamic conditions which couldlead to errors in the critical areas.

iv. Estimation of induced stresses by mathematical approximations is complicated.

v. Due to the complexity associated with manufacturing stresses (stresses left on the wheel due to processes such as the blank stamping forming), no attempt is made to describe their contribution to the total stress state at a material point on the wheel.

vi. The bead - tyre interface is assumed to be air-tight in both static and dynamic conditions. This may not be so assertive as in real life situation, the tyre may dislodge partially and momentarily from the bead seat, thus causing loss of inflation pressure, due to the undulating motion occasioned by bumps and road surface irregularities.

vii. Centrifugal force due to the rotation of tyre wheel assembly is not usually considered.

viii. Strain gauge/rosetteerrors may affect the accuracy of results.

2.11 Overview of Loading Methods

Several methods for modeling the effect of the radial load as its transferred to the rim have been adapted. Results show that the loading shape is in the form of a cosine function about a central angle of approximately $30^{o}$to 40^{o} from either side of the point of contact with the ground. Some assumed this 30^{o} angle is developed from the contact patch (flat spot at the point of contact with the ground) geometry of the tyre converted to an equivalent angle swept by the bead seat area in contact with the rim. Another method assumes the contact patch sweeps an angle of 90^{o} symmetrical about the point of loading, which is is analogous to a cylindrical bar (eye-bar) in clevis, assuming no gap exists. (Stearns et al, 2003).

2.12 Eye - Bar Analogy

Consider a round rod in an eye bar under an equilibrium of forces as shown in Figure 2.5(Stearns, 2000; Stearns et al, 2003; Mohd, 2011).

In the figure, r, is the radius of the hole, W is the load imparted, θ, is the angle and q_{max} is the maximum pointload. The horizontal components of q are balanced. The vertical forces can be related to the external load, W given as:

$$W = 2r \int_0^{\frac{\pi}{2}} q cos\theta d\theta \tag{2.4}$$

Defining q =q_{max} cosθ and substituting into equation (2.4) gives,

$$W = 2r \int_0^{\frac{\pi}{2}} q_{max} cos^2\theta d\theta \tag{2.5}$$

integrating yields,

$$W = 2r q_{max} \left[\frac{\theta}{2} + \frac{sin}{4}\right]_0^{\frac{\pi}{2}} \tag{2.6}$$

$$W = 2q_{max} r \left[\left(\frac{\pi/2}{2} + \frac{sin2^{*}\pi/2}{4}\right) - (0)\right] \tag{2.7}$$

or,

$$q_{max} = \frac{2W}{\pi r} \tag{2.8}$$

q_{max} is the unit load N/mm and r is the radius of the bead seat. Normally, this radius is assumed to be nearly equal to the pin radius. Dividing q_{max} by the width of the eye-bar cross-section (taken as width of bead seat) gives the compressive stress based on the above model.

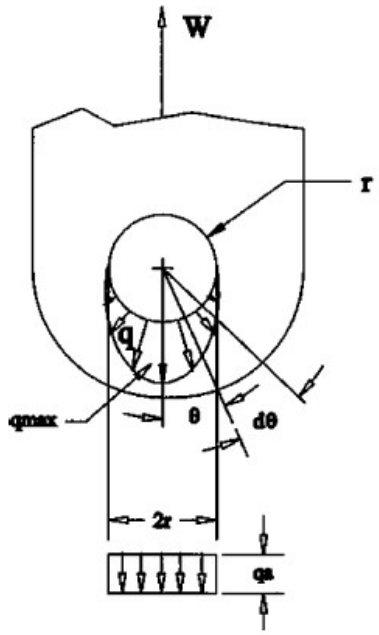

Fig.2.5: Eye-bar loading(Stearns et al, 2003).

2.13 Analysis Under Radial Load (Cosine Function) Approach

The total weight of a car is balanced by a vertical reaction force from the road through the tyre. As the load constantly compresses the wheel radially, it becomes a cyclic load with rotation of the wheel (Stearns, 2000; Stearns et al, 2003; Mohd, 2011). The radial load is expressed by:

$$Q = S_r W \tag{2.9}$$

where, S_r means acceleration test factor (S_r= 2.2) and W, maximum tyre load as with Equation (1.1).In an actual wheel, the radial load is applied to the wheel on the bead seats with tyre, the distributed pressure is loaded directly on the bead seat of the model. The pressure is assumed to have a cosine function distribution mode within a central angle of 40^o in the circumferential direction, Figure 2.6.

By using the cosine function accordingly, the distributed pressure, W_r, is given as:

$$W_r = W_0 cos\left(\frac{\pi}{2}\frac{\theta}{\theta_0}\right) \tag{2.10}$$

The total radial load, W, is evaluated using Equation(2.10) as follows,

$$W = b\int_{-\theta_0}^{\theta_0} W_r r_b d\theta \tag{2.11}$$

Substituting Equation(2.10) into Equation (2.11) results in,

$$W = b\int_{-\theta_0}^{\theta_0} W_0 r_b cos\left(\frac{\pi\theta}{2\theta_0}\right) d\theta \tag{2.12}$$

Integrating,

$$W = bW_0 r_b \frac{1}{(\pi/2\theta_0)}\left[sin\left(\frac{\pi\theta}{2\theta_0}\right)\right]_{-\theta_0}^{\theta_0} \tag{2.13}$$

$$W = 4br_b\theta_0\frac{W_0}{\pi} \tag{2.14}$$

or solving for W_0, gives,

$$W_0 = \frac{W\pi}{4br_b\theta_0} \tag{2.15}$$

where, r_b is the bead seat radius and b is the total width of the bead seats.

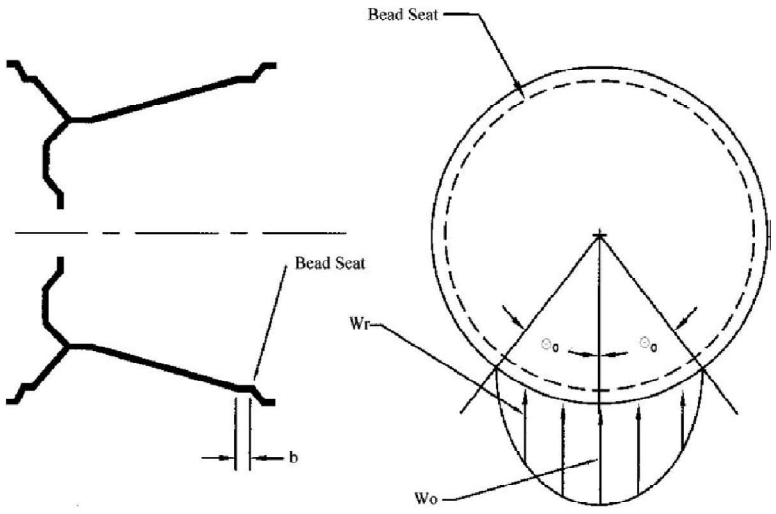

Fig.2.6: Radial loading schematic (Mohd, 2011).

2.14 Contact patch method

Using the idea of the contact patch width, the area of contact over the bead seat is shown in Figure 2.7.(Stearns, 2000; Stearns et al, 2003; Mohd, 2011).

2.15 Half - Plane Under the Action of Concentrated Force Perpendicular to the Boundary - Boussinesq's Theorem.

Consider Figures 2.8 (a), (b) and (c). In both cases of Figures 2.8 (b) and (c) the formula for σ_r , σ_θ and $\tau_{r\theta}$ are the same; the main difference occurs in the magnitude of displacements. Hence, in determination of stresses it will be all the same which is being considered (b or c).

Let us consider a case of plane stress, taking the thickness of the plate equal to unity. The force P is assumed to be applied at one point (concentrated force), therefore, in the small vicinity of the point of application of P it induces very big stress which in case of real material will exceed the proportional limit (Sakyaan, 1996). That area is shaded in Figure 2.9. That area is excluded from our consideration.

Let the stress function for this problem be in the form:

$$\varphi(r\theta) = -\frac{K}{2} r sin\theta \qquad (2.16)$$

Minus sign is chosen because σ_r obviously will be compressive.

Using equation (2.16), we obtain for stresses,

$$\sigma_r = \frac{\partial^2 \varphi}{r^2 \partial\theta^2} + \frac{1}{r}\frac{\partial \varphi}{\partial \theta} = -\frac{Kcos\theta}{r} \qquad (2.17a)$$

$$\sigma_\theta = \frac{\partial \varphi^2}{\partial r^2} = 0 \qquad (2.17b)$$

$$\tau_{r\theta} = -\frac{\partial}{\partial r}\left(\frac{1}{r}\frac{\partial \varphi}{\partial \theta}\right)$$

$$= -\frac{1}{r}\frac{\partial \varphi^2}{\partial r \partial \theta} + \frac{1}{r^2}\frac{\partial \varphi}{\partial \theta} = 0 \qquad (2.17c)$$

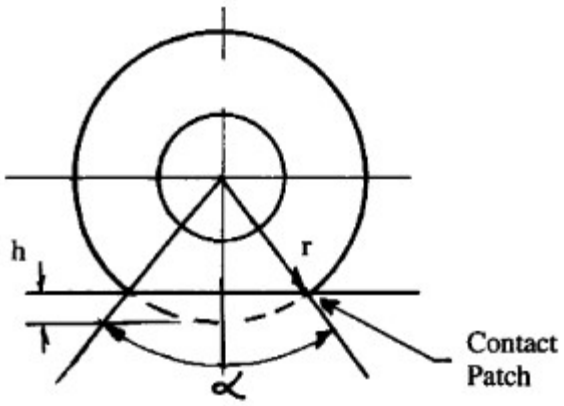

$$h = r\left[1 - \cos\left(\frac{\alpha}{2}\right)\right]$$

Fig.2.7: Contact patch schematic(Stearns, 2000)

Now the differential equations and compatibility equation are satisfied identically.

Determining the coefficient from the boundary conditions:

1. The upper boundary is stress-free ie,

for θ = $\pm\frac{\pi}{2}$, $\sigma_r = 0$ and $\tau_{r\theta} = 0$

it could be seen that these conditions are satisfied everywhere on line AB (see Figure 2.9), except at point of application of force P.

Excluding the small region of radius ρ from consideration where stress is very big (usually exceeding the proportional limit). Replacing the concentrated force and its action by a statically equivalent system of force. The cut is made in elastic region that is why we may assume the action of the removed part by radially distributed forces.

substituting expression for σ_r gives,

$$K\int_{\frac{-\pi}{2}}^{\frac{\pi}{2}}\frac{cos\theta}{\rho}cos\theta\rho d\theta = P \qquad (2.18)$$

or,

$$K\int_{\frac{-\pi}{2}}^{\frac{\pi}{2}}cos^2\theta = P$$

Hence,

$$K\frac{\pi}{2} = P$$

and,

$$K = \frac{2P}{\pi} \qquad (2.19)$$

substituting (2.19) into (2.17a) we have,

$$\sigma_r = \frac{-2Pco}{\pi r} \qquad (2.20)$$

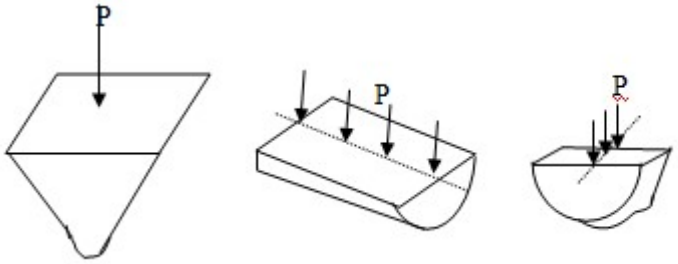

(a) Half-space (b) Plane strain (c) Plane stress

Fig.2.8: Boundary sections(Sakyaan, 1996).

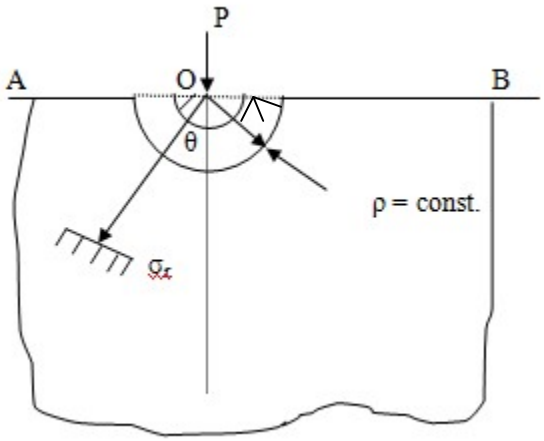

Fig.2.9: Loaded half - plane section(Sakyaan, 1996).

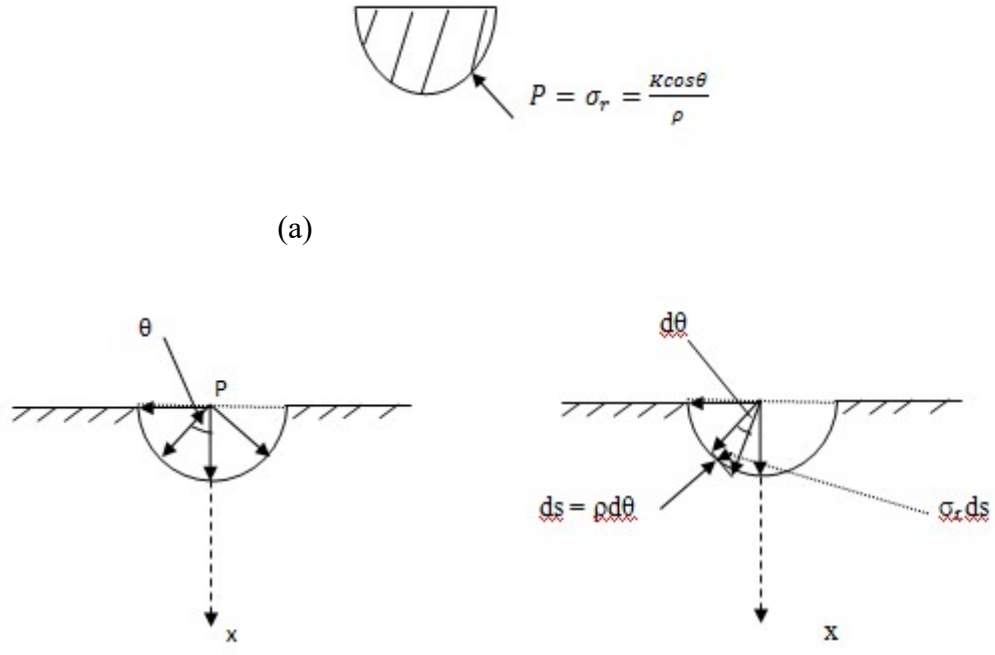

Fig.2.10: Active and reactive forces on plane(Sakyaan, 1996).

2.16 Analysis of Tyre Pressure

The tyre pressure is a constant load with no relation to the rotation of the wheel. However, the induced stress on the rim due to inflation pressure only, is comparatively small. The tyre air pressure is applied directly to both the outside of the rim and tyre. The load on the flange is directed in the axial direction and, is generated by the air pressure pressing on the side wall. This load dependson the type, aspect ratio of the cross-sectionand the reinforcement structure of the tyre (Stearns *et al*, 2003). From Figure 2.11,the axial component of the force W_p which results from the inflation of the tyre is calculated by,

$$W_P = \pi\left(a^2 - r_f^2\right)P_o \tag{2.21}$$

where, a, is the design radius of the tyre and r_f is the radius of the loading point on the rim flange. Because the axial load is supported by the tread of the tyre and the rim flange, approximately a half of the load is assumed to be loaded on each part. So, the load (tyre force T_f) on the circumferential unit length of the rim flange is calculated as follows:

$$T_f = \frac{W_P}{2(2\pi r_f)} = \left(a^2 - r_f^2\right)\frac{P_O}{4r_f} \tag{2.22}$$

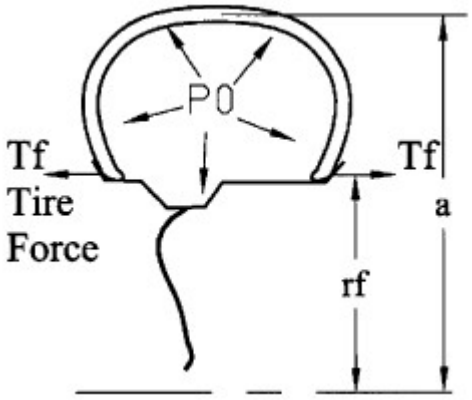

Fig. 2.11: Tyre force schematic(Stearns, 2000)

2.17 Constitutive Stress-Strain Relations

2.17.1 Three-Dimensional Case

In the case of linearly elastic isotropic three-dimensional solid,(Rao, 1992), the stress-strain relations are:

$$= \begin{Bmatrix} \varepsilon_{xx} \\ \varepsilon_{yy} \\ \varepsilon_{zz} \\ \varepsilon_{xy} \\ \varepsilon_{yz} \\ \varepsilon_{zx} \end{Bmatrix} = [C]\sigma \qquad (2.23)$$

$$= [C] \begin{Bmatrix} \sigma_{xx} \\ \sigma_{yy} \\ \sigma_{zz} \\ \sigma_{xy} \\ \sigma_{yz} \\ \sigma_{zx} \end{Bmatrix} = [C]\sigma \qquad (2.24)$$

$$[C] = \begin{bmatrix} C_{11} & C_{12} & C_{13} & C_{14} & C_{15} & C_{16} \\ C_{21} & C_{22} & C_{23} & C_{24} & C_{25} & C_{26} \\ C_{31} & C_{32} & C_{33} & C_{34} & C_{35} & C_{36} \\ C_{41} & C_{42} & C_{43} & C_{44} & c_{45} & c_{46} \\ c_{51} & c_{52} & c_{53} & c_{54} & c_{55} & c_{56} \\ c_{61} & c_{62} & c_{63} & c_{64} & c_{65} & c_{66} \end{bmatrix} \qquad (2.25)$$

Where [C] is a matrix of elastic coefficient given by:

$$[C] = \frac{1}{E} \begin{bmatrix} 1 & 1-\nu & -\nu & 0 & 0 & 0 \\ -1 & 1 & -\nu & 0 & 0 & 0 \\ -\nu & -\nu & 1 & 0 & 0 & 0 \\ 0 & 0 & 0 & 2(1+\nu) & 0 & 0 \\ 0 & 0 & 0 & 0 & 0 & 2(1+\nu) \\ 0 & 0 & 0 & 0 & 0 & 2(1+\nu) \end{bmatrix} \qquad (2.26)$$

Inverting equation(2.28) gives:

$$\sigma = \begin{Bmatrix} \sigma_{xx} \\ \sigma_{yy} \\ \sigma_{zz} \\ \sigma_{xy} \\ \sigma_{yz} \\ \sigma_{zx} \end{Bmatrix} = D\varepsilon \qquad (2.27)$$

$$D = \begin{Bmatrix} \varepsilon_{xx} \\ \varepsilon_{yy} \\ \varepsilon_{zz} \\ \varepsilon_{xy} \\ \varepsilon_{yz} \\ \varepsilon_{zx} \end{Bmatrix} \qquad (2.28)$$

Where the matrix D is given by:

$$[D] = \frac{E}{(1+\nu)(1-2\nu)}\begin{bmatrix} 1-\nu & \nu & \nu & 0 & 0 & 0 \\ \nu & 1-\nu & 0 & 0 & 0 & 0 \\ \nu & \nu & 1-\nu & 0 & 0 & 0 \\ 0 & 0 & 0 & (1-2\nu)/2 & 0 & 0 \\ 0 & 0 & 0 & 0 & (1-2\nu)/2 & 0 \\ 0 & 0 & 0 & 0 & 0 & (1-2\nu)/2 \end{bmatrix} \quad (2.29)$$

In the case of two-dimensional problem, both plane stress and plane strain exist.

2.17.2 Two - dimensional case (Plane Stress)

For plane stress, $\sigma_{zz} = \sigma_{zx} = \sigma_{yz} = 0$ and the stress-strain relationis:

$$\varepsilon = [C]\sigma \quad (2.30)$$

$$\varepsilon = \begin{Bmatrix} \varepsilon_{xx} \\ \varepsilon_{yy} \\ \varepsilon_{xy} \end{Bmatrix} \quad (2.31)$$

And,

$$\sigma = \begin{Bmatrix} \sigma_{xx} \\ \sigma_{yy} \\ \sigma_{xy} \end{Bmatrix} \quad (2.32)$$

$$[C] = \frac{1}{E}\begin{bmatrix} 1 & -\nu & 0 \\ -\nu & 1 & 0 \\ 0 & 0 & 2(1+\nu) \end{bmatrix} \quad (2.33)$$

inverting equation(2.30) gives,

$$\sigma = D\varepsilon \quad (2.34)$$

with

$$[D] = \frac{1}{1-\nu^2}\begin{bmatrix} 1 & \nu & 0 \\ \nu & 1 & 0 \\ 0 & 0 & \frac{1-\nu}{2} \end{bmatrix} \quad (2.35)$$

In the case of plane stress, the component of strain in the z-direction will be nonzero and is given by:

$$\varepsilon_{zz} = -\frac{\nu}{E}(\sigma_{xx} + \sigma_{yy}) \quad (2.36)$$

while,

$$\varepsilon_{yz} = \varepsilon_{zx} = 0 \quad (2.37)$$

2.17.3 Two - Dimensional Case (Plane Strain)

In this case the three - dimensional stress - strain relationgiven by equation(2.33)reduces to:

$$\varepsilon = [C]\sigma \qquad (2.38)$$

where,

ε and σ are as expressed by equations (2.31) and (2.32)and,

$$[C] = \frac{1+\nu}{E}\begin{bmatrix} 1-\nu & -\nu & 0 \\ -\nu & 1-\nu & 0 \\ 0 & 0 & 2 \end{bmatrix} \qquad (2.39)$$

inverting gives,

$$\sigma = D\varepsilon \qquad (2.40)$$

where ε is as defined by equation (2.31) and,

$$[D] = \frac{E}{(1+\nu)(1-2\nu)}\begin{bmatrix} 1-\nu & \nu & 0 \\ \nu & 1-\nu & 0 \\ 0 & 0 & \frac{1-\nu}{2} \end{bmatrix} \qquad (2.41)$$

the component of stress in the z - direction is given by,

$$\sigma_{zz} = \nu(\sigma_{xx} + \sigma_{yy}) \qquad (2.42)$$

and

$$\sigma_{yz} = \sigma_{zx} = 0 \qquad (2.43)$$

2.17.4. One - Dimensional Case

In the case of one -dimensional problem, all stress components except one normal stress are zero and the stress - strain relation reduces to:

$$\varepsilon = [C]\sigma \qquad (2.44)$$

where,

$$\varepsilon = \varepsilon_{zz} \qquad and \qquad \sigma = \sigma_{xx} \qquad (2.45)$$

$$[C] = \left[\frac{1}{E}\right] \qquad (2.46)$$

and

$$\sigma = D\varepsilon \qquad (2.47)$$

where

$$D = [E] \qquad (2.48)$$

2.17.5. Axisymmetrical Case

In the case of solids of revolution (axisymmetric solids), the stress - strain relations(Rao, 1992) are give by:

$$\varepsilon = [C]\sigma \tag{2.49}$$

where

$$\varepsilon = \begin{Bmatrix} \varepsilon_{rr} \\ \varepsilon_{\theta\theta} \\ \varepsilon_{zz} \\ \varepsilon_{rz} \end{Bmatrix} \tag{2.50}$$

and

$$\sigma = \begin{Bmatrix} \sigma_{rr} \\ \sigma_{\theta\theta} \\ \sigma_{zz} \\ \sigma_{rz} \end{Bmatrix} \tag{2.51}$$

$$[C] = \frac{1}{E}\begin{bmatrix} 1 & -\nu & -\nu & 0 \\ -\nu & 1 & -\nu & 0 \\ -\nu & -\nu & 0 & 0 \\ 0 & 0 & 0 & 2(2+\nu) \end{bmatrix} \tag{2.52}$$

and

$$\sigma = D\varepsilon \tag{2.53}$$

and

$$[D] = \frac{E}{(1+\nu)(1-2\nu)}\begin{bmatrix} 1-\nu & \nu & \nu & 0 \\ \nu & 1-\nu & \nu & 0 \\ \nu & \nu & 0 & 0 \\ 0 & 0 & 0 & (1-2\nu)/2 \end{bmatrix} \tag{2.54}$$

2.17.6. Strain - Displacement Relation in Three Dimensions

The strain - displacement relationis given as:

$$\varepsilon = \begin{Bmatrix} \varepsilon_{xx} \\ \varepsilon_{yy} \\ \varepsilon_{zz} \\ \varepsilon_{xy} \\ \varepsilon_{yz} \\ \varepsilon_{zx} \end{Bmatrix} = \begin{Bmatrix} \frac{\partial u}{\partial x} \\ \frac{\partial v}{\partial y} \\ \frac{\partial w}{\partial z} \\ \frac{\partial u}{\partial y} + \frac{\partial v}{\partial x} \\ \frac{\partial v}{\partial z} + \frac{\partial w}{\partial y} \\ \frac{\partial w}{\partial x} + \frac{\partial u}{\partial z} \end{Bmatrix} = \begin{Bmatrix} \frac{\partial}{\partial x} & 0 & 0 \\ 0 & \frac{\partial}{\partial y} & 0 \\ 0 & 0 & \frac{\partial}{\partial z} \\ \frac{\partial}{\partial y} & \frac{\partial}{\partial x} & 0 \\ 0 & \frac{\partial}{\partial z} & \frac{\partial}{\partial y} \\ \frac{\partial}{\partial x} & 0 & \frac{\partial}{\partial z} \end{Bmatrix} \begin{Bmatrix} u \\ v \\ w \end{Bmatrix} \tag{2.55}$$

2.20. Coordinate Transformation

2.20.1 Transformation in Two - Dimensions

Considering the double integral (Stroud, 1996),

$$\iint \phi(x,y)dxdy \tag{2.56}$$

where, $x = f(u,v)$ and $g = f(u,v)$ and singled valued functions, then every point P(x,y) within the region R in the x-y plane maps on to a unique point $P_1(u,v)$ in the corresponding region R_1 in the uv plane Figures 2.12 a & b)(Stroud, 1996). For an element of area in the x-y plane and corresponding element in the uv-plane, Figures 2.13 (a& b).

Points P, Q, R, S in the x-y plane map into P_1, Q_1, R_1, S_1 in the uv-plane. Point P(x_0, y_0) now have the value $P_1(u_0, v_0)$ in the new variables. If the transformation equations are x = f(u, v) and y = g(u, v), and treating as a pair of simultaneous equations for u and v gives,

$$u = F(x,y) \tag{2.57a}$$

and

$$v = G(x,y) \tag{2.57b}$$

The u and v values relating to any particular point are its curvilinear coordinates and x = f(u, v) and y = g(u, v) are the transformation equations between the two systems.

In the Cartesian coordinates (x, y) system, Figures 2.14 (a &b) the element of area $\delta A = \delta_x\delta_y$ and is the area bounded by the lines $x = x_0$, $x = x_0 + \delta_x$; $y = y_0$, $y = y_0 + \delta_y$.

In the new system of curvilinear coordinates (u, v) the element of area δA, can be taken as that of figure P_1, Q_1, R_1, S_1, i.e, the area bounded by the curves $u = u_0$, $u = u_0 + \delta u$; $v = v_0$, $v = v_0 + \delta v$. Since δA_1 is small, P_1, Q_1, R_1, S_1 and regarding it as a rectangle, i.e,

$\delta A \approx 2 \times$area of triangle P_1, Q_1, S_1.

Expressing the area of a triangle with vertices (x_1, y_1), (x_2, y_2), (x_3, y_3) in determinant form gives,

$$Area = \frac{1}{2}\begin{vmatrix} 1 & 1 & 1 \\ x_1 & x_2 & x_3 \\ y_1 & y_2 & y_3 \end{vmatrix} \tag{2.58}$$

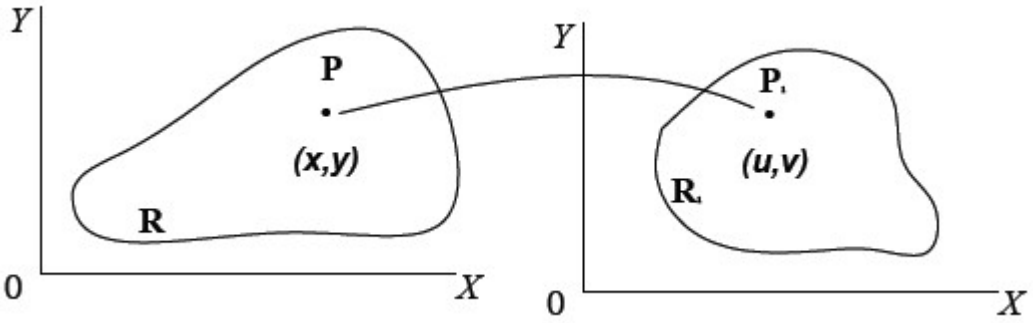

(a) (b)

Fig.2.12: (a) & (b): Mapping planes(Stroud, 1996).

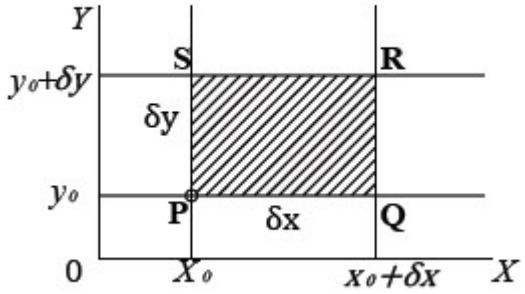

(a)

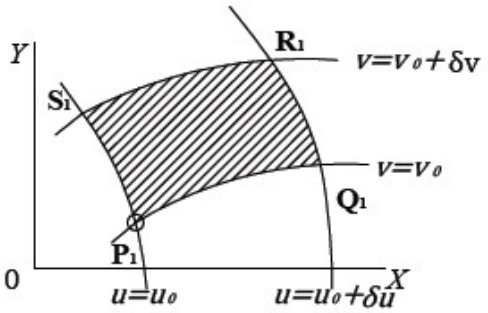

(b)

Fig.2.13: (a) & (b): Transformation planes(Stroud, 1996)

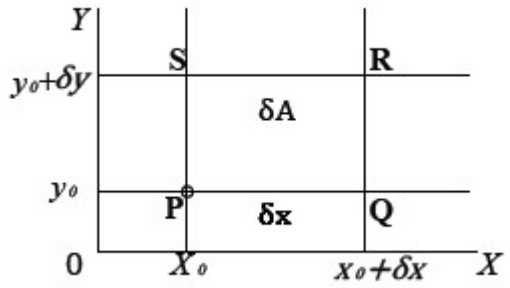

(a)

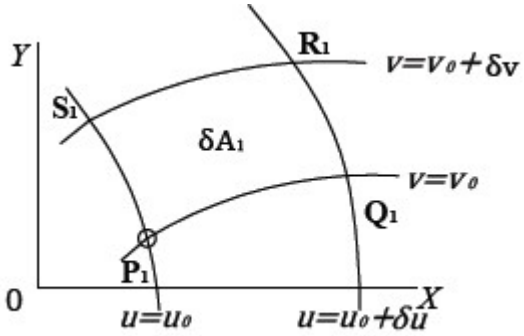

(b)

Fig.2.14: (a & b): Transformation planes(Stroud, 1996)

If x = f(u, v), then a small increase δ_x in x is given by,

$$\delta x = \frac{\partial f}{\partial u}\delta u + \frac{\partial f}{\partial v}\delta v \tag{2.59}$$

ie,

$$\delta x = \frac{\partial x}{\partial u}\delta u + \frac{\partial x}{\partial v}\delta v \tag{2.60}$$

and for y = g(u, v),

$$\delta y = \frac{\partial y}{\partial u}\delta u + \frac{\partial y}{\partial v}\delta v \tag{2.61}$$

P_1 coincides with P(x, y), therefore,

a. P_1 is the point (x, y)

b. Q_1 corresponds to Q, ie, small change from P and equations (2.60)and (2.61)apply.

But along P_1 Q_1 v is constant, therefore, δv = 0.

that is:

$$\delta x = \frac{\partial x}{\partial u}\delta u \tag{2.62}$$

and

$$\delta y = \frac{\partial y}{\partial u}\delta u \tag{2.63}$$

ie Q is at point $(x + \frac{\partial x}{\partial u}\delta u, y + \frac{\partial y}{\partial u}\delta u)$

Similarly for S_1, u is constant along P_1 S_1, $\delta u = 0$ and therefore,

S_1 is the point $(x + \frac{\partial x}{\partial v}\delta v, y + \frac{\partial y}{\partial v}\delta v)$

so that the Cartesian coordinates of P_1, Q_1, S_1 are:

P_1 (x, y); $Q(x + \frac{\partial x}{\partial u}\delta u, y + \frac{\partial y}{\partial u}\delta u)$; $S_1(x + \frac{\partial x}{\partial v}\delta v, y + \frac{\partial y}{\partial v}\delta v)$

the determinant for the area P_1, Q_1, S_1 is

$$Area = \frac{1}{2}\begin{vmatrix} 1 & 1 & 1 \\ x & x + \frac{\partial x}{\partial u}\delta u & x + \frac{\partial x}{\partial v}\delta v \\ y & y + \frac{\partial y}{\partial u}\delta u & y + \frac{\partial y}{\partial v}\delta v \end{vmatrix} \tag{2.64}$$

subtracting column 1 from columns 2 and 3 gives,

$$Area = \frac{1}{2}\begin{vmatrix} 1 & 0 & 0 \\ x & \frac{\partial x}{\partial u}\delta u & \frac{\partial x}{\partial v}\delta v \\ y & \frac{\partial y}{\partial u}\delta u & \frac{\partial y}{\partial v}\delta v \end{vmatrix} \tag{2.65}$$

which simplifies to,

$$Area = \frac{1}{2}\begin{vmatrix} \frac{\partial x}{\partial u}\delta u & \frac{\partial x}{\partial v}\delta v \\ \frac{\partial y}{\partial u}\delta u & \frac{\partial y}{\partial v}\delta v \end{vmatrix} \quad (2.66)$$

Taking out the factor δu and δv from the first and second columns respectively gives,

$$Area = \frac{1}{2}\begin{vmatrix} \frac{\partial x}{\partial u} & \frac{\partial x}{\partial v} \\ \frac{\partial y}{\partial u} & \frac{\partial y}{\partial v} \end{vmatrix} \delta u \delta v \quad (2.67)$$

multiplying equation (2.67)by 2 gives the area of the rectangle as,

$$\text{Area, } \delta A = \begin{vmatrix} \frac{\partial x}{\partial u} & \frac{\partial x}{\partial v} \\ \frac{\partial y}{\partial u} & \frac{\partial y}{\partial v} \end{vmatrix} \delta u \delta v \quad (2.68)$$

expressing in differential gives,

$$dA = \begin{vmatrix} \frac{\partial x}{\partial u} & \frac{\partial x}{\partial v} \\ \frac{\partial y}{\partial u} & \frac{\partial y}{\partial v} \end{vmatrix} du dv \quad (2.69)$$

and for convenience, this is written as,

$$dA = \frac{\partial(x,y)}{\partial(u,v)} du dv \quad (2.70)$$

$\frac{\partial(x,y)}{\partial(u,v)}$is called the Jacobian of the transformation from cartesian coordimates (x,y) to the curvilinear coordinates (u,v),

ie,

$$J(u,v) = \frac{\partial(x,y)}{\partial(u,v)} = \begin{vmatrix} \frac{\partial x}{\partial u} & \frac{\partial x}{\partial v} \\ \frac{\partial y}{\partial u} & \frac{\partial y}{\partial v} \end{vmatrix} \quad (2.71)$$

$$dA = detJ(u,v) du dv \quad (2.72)$$

2.20.2 Transformation in Three - Dimensions

If the integral is of the form, $\iiint \theta(x,y,z)\, dxdydz$ such that $x = f(u,v,w)$; $y = g(u,v,w)$ and z $= h(u,v,w)$ then the Jacobian is given as,

$$J = (u, v, w) = \frac{\partial(x,y,z)}{\partial(u,v,w)} = \begin{vmatrix} \frac{\partial x}{\partial u} & \frac{\partial y}{\partial u} & \frac{\partial z}{\partial u} \\ \frac{\partial x}{\partial v} & \frac{\partial y}{\partial v} & \frac{\partial z}{\partial v} \\ \frac{\partial x}{\partial w} & \frac{\partial}{\partial w} & \frac{\partial z}{\partial w} \end{vmatrix} \tag{2.73}$$

and the element of volume dv = dxdydz becomes

$$dv = |J(u, v, w)| dudvdw \tag{2.74}$$

Also, the integral is transformed, thus,

$$\iiint \theta(x, y, z)\, dxdydz = \iiint G(x, y, z) \left|\frac{\partial(x,y,z)}{\partial(u,v,w)}\right| dudvdw \tag{2.75a}$$

$$= \iiint G(x, y, z)\, detJ dudvdw \tag{2.75b}$$

2.21. Principal Strains and Direction From Measurement.

The equations for calculating principal strains from three rosette (rectangular and delta) strain measurements are derived from "strain transformation" relationship. It involves expressing themeasured normal strain in any axial direction on the test surface in terms of two principal strains and the angle relative to the principal axis. This depicted by Figure 2.15 (www.measurementsgroup.com., 2000). While the strain gages in rectangular rosettes are oriented at 0^o, $45^o$and 90^o, that of delta rosette are oriented at0^o, 60^o and 120^o.

From Figure 2.16 (noting that the angles in the Mohr's circle are double the physical angles on the test surface) that the normal strain at any angle θ from the major principal axis is simply expressed by:

$$\varepsilon_\theta = \frac{\varepsilon_P + \varepsilon_Q}{2} + \frac{\varepsilon_P - \varepsilon_Q}{2} cos2\theta \tag{2.76}$$

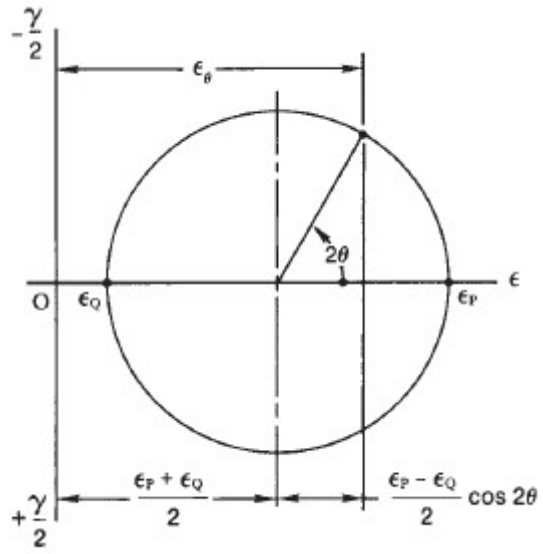

Fig.2.15: Mohr's circle for strains (www.measurementsgroup.com., 2000)

2.21.1 Rectangular Rosette

Figure 2.16 shows a surface with a rectangular rosette installed and with reference grid oriented at θ degrees from ε_p. Figure (2.17) shows the graphical (Mohr's circle) representation of the rosettes. Substituting the respective angles into equation (2.76) yield:

$$\varepsilon_1 = \frac{\varepsilon_P+\varepsilon_Q}{2} + \frac{\varepsilon_P-\varepsilon_Q}{2} cos2\theta \quad (2.77a)$$

$$\varepsilon_2 = \frac{\varepsilon_P+\varepsilon_Q}{2} + \frac{\varepsilon_P-\varepsilon_Q}{2} cos2(\theta + 45^o) \quad (2.77b)$$

$$\varepsilon_2 = \frac{\varepsilon_P+\varepsilon_Q}{2} + \frac{\varepsilon_P-\varepsilon_Q}{2} cos2(\theta + 90^o) \quad (2.77c)$$

Equations (2.77) express axial strain in terms of principal strains. Inverting equation (2.77), that is, expressing principal strains in terms of axial strains yield;

$$\varepsilon_{P,Q} = \frac{\varepsilon_1+\varepsilon_3}{2} \pm \frac{1}{\sqrt{2}}\sqrt{(\varepsilon_1-\varepsilon_2)^2+(\varepsilon_2-\varepsilon_3)^2} \quad (2.78)$$

$$\theta = \frac{1}{2} tan^{-1}\left(\frac{\varepsilon_1-2\varepsilon_2+\varepsilon_3}{\varepsilon_1-\varepsilon_3}\right) \quad (2.79)$$

the angle, θ represents the acute angle from the principal axis to the reference grid of the rosette.

2.21.2 Delta Roette

The grid angles, θ, θ + 60 degrees and θ + 120 degrees, of the delta rosette are shown in Figure 2.18. Substituting values from Figure 2.20 into equation (2.72) yield axial principal strain values as:

$$\varepsilon_{P,Q} = \frac{\varepsilon_1+\varepsilon_2+\varepsilon_3}{3} \pm \frac{\sqrt{2}}{3}\sqrt{(\varepsilon_1-\varepsilon_2)^2+(\varepsilon_2-\varepsilon_3)^2+(\varepsilon_3-\varepsilon_1)^2} \quad (2.80)$$

$$\theta = \frac{1}{2} tan^{-1}\left(\frac{\sqrt{3}(\varepsilon_1-\varepsilon_3)}{2\varepsilon_1-\varepsilon_2-\varepsilon_3}\right) \quad (2.81)$$

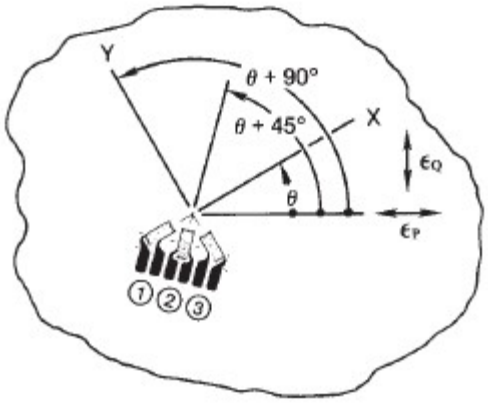

Fig.2.16: Arrangement of rectangular rosette *(*www.measurementsgroup.com., 2000)

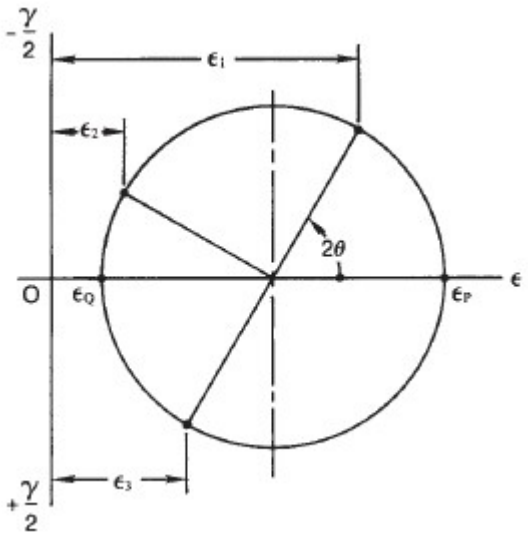

Fig.2.17: Mohr's circle for rectangular rosette (www.measurementsgroup.com., 2000)

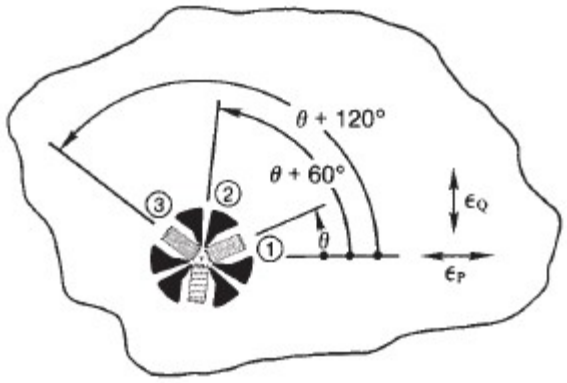

Fig.2.18: Arrangement of delta rosette (www.measurementsgroup.com., 2000) .

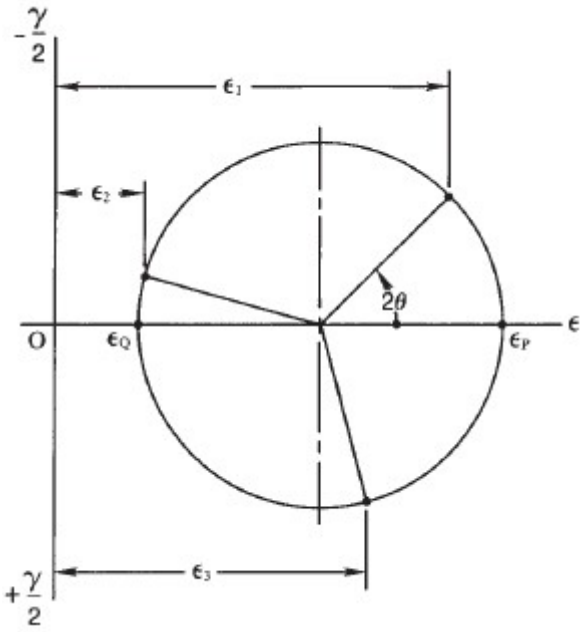

Fig.2.19: Mohr's circle for delta rosette(www.measurementsgroup.com., 2000)

2.21.3 Principal Stresses From Principal Strains

Knowing the Young's modulus of elasticity (E) and the poison's ratio (ν) of the material and referring to equation (2.42) and replacing σ_x and σ_y with σ_P and σ_Q respectively and equating $\sigma_{xy} = 0$; replacing ε_x and ε_y with ε_P and ε_Q respectively and, making $\varepsilon_{xy} = 0$, Hooke's law for the biaxial strain state is expressed, in terms of the principal stresses and strains are:

$$\sigma_P = \frac{E}{1-\nu^2}\left(\varepsilon_P + \nu\varepsilon_Q\right) \quad (2.82a)$$

$$\sigma_Q = \frac{E}{1-\nu^2}\left(\varepsilon_Q + \nu\varepsilon_P\right) \quad (2.82b)$$

The numerical values of the principal strains calculated from equations (2.78) and(2.30)can be substituted into equation (2.82), along with the elastic properties, to obtain the principal stresses. Alternatively, is to substitute equations (2.84)or(2.86), depending on the rosette type into equation (2.81) to express the principal stress straight in terms of the three measured strains and the material properties. The results are::

For rectangular rosette,

$$\sigma_{P,Q} = \frac{E}{2}\left(\frac{\varepsilon_1+\varepsilon_3}{1-\nu} \pm \frac{\sqrt{2}}{1+\nu}\sqrt{(\varepsilon_1-\varepsilon_2)^2 + (\varepsilon_2-\varepsilon_3)^2}\right) \quad (2.82)$$

while for delta rosette,

$$\sigma_{P,Q} = \frac{E}{3}\left(\frac{\varepsilon_1+\varepsilon_2+\varepsilon_3}{1-\nu} \pm \frac{\sqrt{2}}{1+\nu}\sqrt{(\varepsilon_1-\varepsilon_2)^2 + (\varepsilon_2-\varepsilon_3)^2 + (\varepsilon_3-\varepsilon_1)^2}\right) \quad (2.83)$$

2.22 Finite Element Analysis

The finite element method is a numerical method which can be used for the accurate solution of complex engineering problems. The method was first developed in 1956 for the analysis of aircraft structural problems. Thereafter, within a decade, the potentialities of the method for solution of different types of applied science and engineering problems were recognized. Over the years, the finite element technique has been so well established that today it is considered to be one of the best methods for solving a wide variety of practical problems efficiently. In fact, the method has become one of the active research areas for applied mathematicians. One of the main reasons for the popularity of the method in different fields of engineering is that once a general

computer programme has been written, it can be used for the solution of any problem simply by changing input data (Rao, 1992 and Zienkiewicz, 1997)

2.22.1 General Description of the Finite Element Method

In the finite element method, the actual continuum is made up of assemblage of subdivisions known as elements which are to be interconnected nodes. (specific joint). The nodes are located at the boundaries between adjacent elements. The actual variation of the field variable - displacement, stress, temperature, pressure and velocity- in the continuum is unknown and is usually approximated by interpolating functions By solving the field equations for the nodal values, the global solution is derived by the assemblage of the elements (Rao, 1992).

2.22.2 Steps in Finite Element Implementation

The solution of a general continuum problem by the finite element method always follows an orderly step-by-step process viz: Disccritisation of the Structure; Selection of proper interpolation or displacement model; Derivation of Element Stiffness Matrix and Load Vectors; Assemblage of Element Equations to Obtain the Overall Equilibrium Equations; Solution for the nodal displacement and Computation of Element Strains and Stresses for structural problems

2.22.3 Classification of Elements

Finite elements can be classified into three categories, namely, simplex, complex and multiplex.

The simplex elements are those for which the approximating polynomials consist of constant and linear terms. In simplex elements the corners of the elements are taken as nodes. Example of simplex element is two-dimensional triangle with three nodes (corners).

The complex elements may have the same shapes as the simplex elements, but will have additional boundary nodes and sometimes, internal nodes, An example of complex element is a triangular element with three corner nodes and three inside nodes.

The multiplex elements are those whose boundaries are parallel to the coordinate axes to achieve interelement continuity, and whose approximating polynomials contain

higher order terms. A rectangular element is an example of multiplex elements in two-dimensions (Rao, 1992).

2.22.4 Analysisof Three-Dimensional Problems

The basic three dimensional elements for finite element analysis is the tetrahedron element with four corner nodes. One of the major difficulties associated with the use of three-dimensional elements (like tetrahedral, hexahedra and rectangular parallelepiped elements) is that a larger number of elements have to be used for obtaining reasonably accurate results. This leads to a very large number of simultaneous equations to be solved in static analysis.

2.22.5 Tetrahedron Element

The tetrahedron element is shown in Figure 2.20 with global xyz coordinate system. Since there are twelve nodal degrees of freedom and three displacement components u, v and w, the displacement variation is taken to be linear as,

$$u(x,y,z) = \alpha_1 + \alpha_2 x + \alpha_3 y + \alpha_4 z \quad (2.85a)$$

$$v(x,y,z) = \alpha_5 + \alpha_6 x + \alpha_7 y + \alpha_8 z \quad (2.85a)$$

$$w(x,y,z) = \alpha_9 + \alpha_{10} x + \alpha_{11} y + \alpha_{12} z \quad (2.85c)$$

where, α_1, α_2..... α_{12} are constants. By using the nodal coordinates,

$u = Q_{3i-2}$; $v = Q_{3i-1}$; $w = Q_{3i}$ at (x_i, y_i, z_i) (2.86a)

$u = Q_{3j-2}$; $v = Q_{3j-1}$; $w = Q_{3j}$ at (x_i, y_i, z_i) (2.86b)

$u = Q_{3k-2}$; $v = Q_{3k-1}$; $w = Q_{3k}$ at (x_i, y_i, z_i) (2.86c)

$u = Q_{3l-2}$; $v = Q_{3l-1}$; $w = Q_{3l}$ at (x_i, y_i, z_i) (2.86d)

From it is obtained

$$u(x,y,z) = N_i(x,y,z)Q_{3i-1} + N_j(x,y,z)Q_{3j-1} + N_k(x,y,z)Q_{3k-1} + N_l(x,y,z)Q_{3l-1} \quad (2.87)$$

where, N_i, N_j, N_k and N_l are the shape functions.

The field variable is expressed, as follows, in matrix form

$$u = \begin{Bmatrix} u(x,y,z) \\ v(x,y,z) \\ w(x,y,z) \end{Bmatrix} = [N]Q^{(e)}$$

(2.95)

where,

$$N = \begin{bmatrix} N_i & 0 & 0 & N_j & 0 & 0 & N_k & 0 & 0 & N_l & 0 & 0 \\ 0 & N_i & 0 & 0 & N_j & 0 & 0 & N_k & 0 & 0 & N_l & 0 \\ 0 & 0 & N_i & 0 & 0 & N_j & 0 & 0 & N_k & 0 & 0 & N_l \end{bmatrix} \quad (2.88)$$

noting that all the six strain components are relevant in three-dimensional analysis, the strain-displacement relation can be expressed using equation (2.55) as,

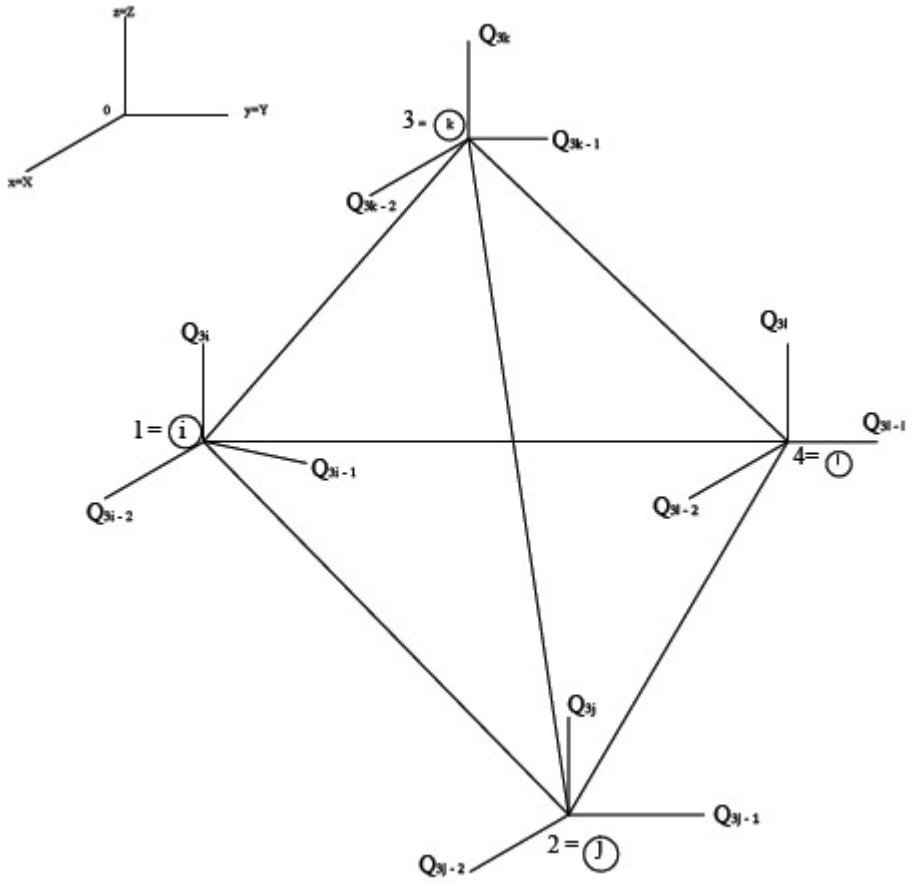

Fig.2.20: A tetrahedron element in the global xyz system(Rao, 1992).

$$\varepsilon = \begin{Bmatrix} \varepsilon_{xx} \\ \varepsilon_{yy} \\ \varepsilon_{zz} \\ \varepsilon_{xy} \\ \varepsilon_{yz} \\ \varepsilon_{zx} \end{Bmatrix} = \begin{Bmatrix} \frac{\partial u}{\partial x} \\ \frac{\partial v}{\partial y} \\ \frac{\partial w}{\partial z} \\ \frac{\partial u}{\partial y} + \frac{\partial v}{\partial x} \\ \frac{\partial v}{\partial z} + \frac{\partial w}{\partial y} \\ \frac{\partial w}{\partial x} + \frac{\partial u}{\partial z} \end{Bmatrix} = [B]Q^{(e)} \quad (2.89)$$

$$[B] = \frac{1}{6V}\begin{bmatrix} b_i & 0 & 0 & b_j & 0 & 0 & b_k & 0 & 0 & b_l & 0 & 0 \\ 0 & c_i & 0 & 0 & c_j & 0 & 0 & c_k & 0 & 0 & c_l & 0 \\ 0 & 0 & d_i & 0 & 0 & d_j & 0 & 0 & d_k & 0 & 0 & d_l \\ c_i & b_i & 0 & c_j & b_j & 0 & c_k & b_k & 0 & c_l & b_i & 0 \\ 0 & d_i & c_i & 0 & d_j & c_j & 0 & d_k & c_k & 0 & d_l & c_l \\ d_i & 0 & b_i & d_j & 0 & b_j & d_k & 0 & b_k & d_l & 0 & b_i \end{bmatrix} \quad (2.90)$$

The stiffness matrix of the element in the global system can be obtained, taking into account the transformation of equation (2.76), as follows,

$$[K]^e = \iiint [B]^T [D][B] dv \quad (2.91)$$

where, [D] is as expressed by equation (2.29).

2.22.6 Hexahedron element

The simplest hexahedron element has eight corner nodes, each with three degrees of freedom. For convenience, the element stiffness matrix is derived by treating it as an isoparamatic element. This element is known as Zienkiewicz-Irons-Brick with 8 nodes (ZIB8)(Rao, 1992) and shown in Figures (2.21&2.22)

2.23 Manufacture of Aluminum Alloy Wheel and its Use in Vehicles

The aluminum alloy A356 is widely used in the wheel industry. It is produced by either gravity casting or by low pressure casting. Gravity casting is the process whereby molten metal is pressed into mold under gravity, while low-pressure casting uses low-pressure of air. (Anonymous, 2006; Das and W. Yin, 2007Jirang and Hans, 2010). Application of aluminium in vehicles extends to semi-finished products and castings.

Research shows that most widely used casting alloy for automotive applications is A356 alloy with a share of approximately 48% of all castings (Rombach and Kuckshinrichs, 2002; Ducker, 2008). Apart from the use of A356 aluminium alloy, A356 T6 and A356.2 are also being used.

CHAPTER THREE
METHODOLOGY

3.1 ANALYTICAL PROCEDURES

The research work presents experimental and finite element (FE) procedure for the annalysis of a selected five armed automobile aluminum alloy wheel (6JX14H2; ET 42) with parabolic cooling hole each of 3466 mm^2 for a passenger car which was loaded with a combination of varying inflation pressure of 0.3 MPa, and 0.15 MPa radial loads of 4750 N and 3570 N, respectively. The radial load represents the combined weight of the vehicle and its occupants. The inflation pressure and radial load were based on the tyre used. In this work, the tyre used was designated: 175 x 65 R14 (Max inflation pressure, 0.3 MPa; maximum radial load, 4750N). The contact patch analogy was used in determining the effective angular range of radial load distribution on the rim. The locations of the rim that were considered for this work were the inboard bead seat, well and the outboard bead seat for both the experimental and the FE methods. Numerical and experimental stress values were then compared using loading conditions of 90 degree eye bar function (EBF), 40 degree cosine function (CF) and the evaluated experimental angle (ECA). Comparison of both FE and experimental values were also done with established works from literature. The variation of both radial load and inflation pressure was to have a wider bases for comparison between the experimental and numerical models.

3.2 EXPERIMENTAL PROCEDURE

For the experiment, the mechanical properties of the wheel were determined by the simple tensile test at the Department of Metallurgy and Materials, Obafemi Awolowo University Ile Ife, while the chemical properties were determined by spark test at The Federal Institute of Industrial Research Oshodi (FIIRO). The wheel was prepared and strain gauge rosettes were attached to the outer surface of the rim at the inboard bead seat, well and

outboard bead seat at interval of 30 degree, from 0 degree to 180 degree, with the datum at the point of contact of the wheel with the ground. With the wheel loaded, its contact patch was measured and converted to the angle swept by the bead seat area, while the induced strain were recorded by the strain measuring device or amplifier. The strains read-out were converted to their respective principal strains, then to principal stresses and ultimately to Von-Mises stresses.

3.3 Items for the Experiment

In carrying out the experiment, the items used were:

1. Tyre (175 x 65 R 14)
2. Five-armed Aluminum alloy Wheel (6JX14H2; ET 42), for a passenger car
3. Test rig
4. Strain rosette (Rectangular)
5. Strain measuring device

3.4 Wheel Surface Preparation

The tyre was mounted on the rim of the wheel. The locations of the surface on which the strain rosette are to be mounted - inboard, well and outboard - were prepared and cleaned. This operation was carried out thus:

1. Solvent degreasing
2. Surface abrasion
3. Application of gage layout lines
4. Surface conditioning
5. Neutralizing

3.4.1 Solvent Degreasing

Solvent degreasing was carried out by the use of chloroethane. it was done to be able to remove oils, grease, organic contaminants and residues. it was the first operation to be carried out. (Karl, 1996 and www.measurementsgroup.com. 2001)

3.4.2 Surface Abrasion

This was carried out to remove scale, rust, paint, coatings, oxides etc, For this action, a silicon carbide paper of P 220 C grits was used to clean the surface.

3.4.3 Layout Lines

The locations for the strain rosette were cleaned with soft, clean, cloth and marked-out with the use of HB pencil.

3.4.4 Surface Conditioning

After marking-out the layout lines, M-Prep Conditioner A was applied repeatedly, and the surface scrubbed with cotton-tipped applications until a clean tip was no longer discoloured by scrubbing. The surface was kept wet until the cleaning was completed.

3.4.5 Neutralizing

The surface on which the rosette were placed was then neutralized by applying the neutralizing agent to avoid oxidation of the surface. The gages (rosettes) were then installed within 30 minutes.

3.5 Gage Handling and Preparation

In handling and preparing the gauge for bonding, certain steps were taken to ensure a successful operation.

Step 1

The gage was removed from its envelop with the aid of tweezers and placed on a clean glass with its bonding side down.

Step 2

The terminals were then placed on the clean class surface and aligned with the gage tabs and separated by a distance of about 3 mm.

Step 3

About 100 mm length of cellophane tape was used to pick the gage and terminals. The tape with the attached gage and terminals were then transferred to the surface/location where the gage is to be attached by positioning and aligning the marks on the gage with the marked lines on the surface of the wheel bead seats and well.

Step 4

The end of the tape opposite the solder tab was then lifted until the gage and terminal were free. The loosed end of the tape was tacked under and pressed to the surface to cause the gage to lie flat with the bonding side exposed.

Step 5

Catalyst, M-Bond 200, was applied and allowed to dry for at least a minute under normal ambient laboratory conditions.

Step 6

The adhesive bond was then applied to the gage-terminal-tape assembly

Step 7

The gage-tape assembly was brought back down so as to align the gage marks with the wheel markings with a single wipe. The cellophane tape was then pulled back directly over itself and off the surface.

Step 8

The gage and terminals were covered with masking tape, while exposing only the solder tabs of both strain gage rosette and terminals.

Step 9

Lead wire of about 2m length was cut. One end of the wire was stripped for a length of about 13 mm and a strand separated from the strands. The remaining strands were then cut close to the insulation and held together with solder and, bonded to the tab of the terminal. The single strand was then soldered to the gage tab. The gage, terminal and lead wire were checked for continuity and resistance using an AVO meter. This procedure was carried out for each of the gages of the strain rosettes. Altogether, there were 21 (twenty-one) strain rosettes, 63 (sixty-three) gages and 126 (one hundred and twenty-six) lead wires,

Step 10

Protective coating was applied to the solder points of the gage and terminal tabs.

3.6 Operation of Test Rig

The steps taken before loading the tyre - wheel assembly were as follows: First the tyre was mounted on the rim of the wheel. The inner surface of the rim was prepared. Strain rosette were then attached at intervals of 30 degree (between 0 degree and 180 degree) on the wheel's inboard bead seat, the well and outboard beat seat. Lead wires were then attached to each of the terminals and strain rosette, with the other end attached to the strain recorder. The flanged rods were then attached to the wheel's hub and, with the vertical column support slipped onto the rod ends of each flanged rod. The horizontal beam support was then slipped into the bushings of the vertical guide column. The whole assembly was slipped into the vertical guide rails, base plate and base structure assembly.

With this in place, the entire assembly was mounted on the hydraulic press and loaded as prescribed. The loading comprised the radial load (weight of vehicle and occupants) and the inflation pressure of the tyre. the radial load values employed were 4750 and 3570 N, while the inflation pressure employed are 0.3 MPa, and 0.15 MPa. These values were used depending on the maximum load and maximum inflation pressure of the tyre as prescribed by the manufacture. The tyre used was 175/65 R14, and with a maximum load of 4750 N and maximum inflation pressure of 0.3MPa. The strain induced due to each loading combination was read off the strain recorder. The rosettes were numbered from R1 to R21 (R1 is for Rosette no. 1, while R2 is for Rosette no. 2 in that order to R21), with each rosette having three gauges each, tagged as G1, G2 and G2 respectively. The gage numbering was counterclockwise.

Table 3.1: Load variation combination

Inflation Pressure (MPa)	Scenerio	Radial Load (Min)	Radial Load (Max)
0.15 KPa	Under inflation pressure	3570 N	4750 N
0.3KPa	Maximum inflation pressure	3570 N	4750 N

3.7 Finite Element Analysis

In the finite element approach, a 3-D solid model of the wheel (6JX14H2; ET 42) with the same parabolic cooling hole shape and area of 3466 $mm^2$was generated,discredited into elements and all loading patterns were deployed for analysis by the finite element method using Creo Elements/ Pro 5.0. The model consists of 38,493hexahedral elements. The wheel was constrained at the bolt holes. Radial loads of 4750 N and 3570 N was then applied with varying inflation pressure of 0.3MPa and 0.15MPa, respectively to determine the stress and displacement distribution at the inboard, well and outboard bead seats respectively.

3.8 Numerical Study

A numerical study to investigate the effect of cooling hole geometry of triangular, quadrilateral and oval was carried out. First, 3-D models of the wheel with quadrilateral and triangular cooling holes each with the same cooling hole area of 3466 mm^2 as the oval cooling hole shaped wheel with respective aspect ratio of 0.78 and 0.71 were generated and numerical study was carried out at 4750 N radial load and 0.3 MPa inflation pressure. A further numerical study was carried out at the inboard with the same loading conditions, but with cooling hole area 0.2229 mm^2 for triangular, quadrilateral and oval cooling holes at different aspect ratios. This area was chosen because this was the largest sized equilateral triangular cooling hole area that can be accommodated between the hub and the inner face of the wheel. The aspect ratios considered for the triangular cooling hole were 1 and 0.5 respectively, while for the quadrilateral and oval cooling holes, the aspect ratio each were 1, 0.5, 0.33. and 0.2, respectively. Aspect ratio of 0.33 and 0.25 were not considered for the triangular cooling hole because beyond aspect ratio of 0.5, the arm of the wheel snapped leaving the wheel as a hollow cylinder.

CHAPTER FOUR

RESULTS AND DISCUSSION

Plate 4.1 shows the picture of the selected wheel. Plate 4.2 shows the cut section of the selected wheel, while Plate 4.3 represents the cut-out sample of gauge length that was used for the tensile test to determine the wheel's mechanical properties. The mechanical properties are shown in Table 4.1 and the results for Table 4.2 represent the chemical properties of the wheel. Figure 4.1 depicts the wheel's dimensions. Figure 4.2 and 4.3 show the 3-D wheel model,outboard and inboard view, respectively. The wheel's 3-D mesh is represented Figure 4.4. Experimental strain results from the stain rosette at the inboard bead seat, well and outboard bead seat,at interval of 30 degree between 0 degree and 180 degree, are shown in TablesA1- A16in appendix A. They represent the measured strains, maximum principal strains, maximum principal stresses and the Von - Mises stresses at the wheel's locations of inboard bead seat, well and outboard bead seats.

4.1 Contact Patch Angle From Experiment

Table 4.3 shows the contact patch angleobtained during the course of carrying out the experiment. The mean value was used for the numerical simulation. The mean value of the experimentalwheel's contact angle was about 30.25 degrees.Literature values range approximately 30, 40 and 90 degrees. The result obtained from the finite element analysis at 30.25 degree were then used to compare values at 40 degree cosine function 90 degree contact angle.

Plate 4.1: Picture of Selected Wheel

Plate 4.2: Picture of Selected wheel section

Plate 4.3: Gauge length of test piece

Table 4.1: Mechanical properties of Al alloy wheel

Mechanical properties	
Young's Modulus	22.29 GPa
Yield Stress	222.5 MPa
Poison's ratio	0.42
Ultimate tensile stress	69.2 MPa
Percentage elongation	2.8 %
Brinell hardness	48

Table 4.2: Chemical properties of Alloy wheel

Chemical composition	
Element	Percentage composition (%)
Aluminum (Al)	87.00
Silicon (Si)	11.150
Cupper (Cu)	0.496
Magnesium (Mn)	0.281
Manganese (Mg)	0.032
Chromium (Cr)	0.050
Zinc (Zn)	0.259
Titanium (Ti)	0.082
Lead (Pb)	0.038
Iron (Fe)	0.590
Others	0.020

Plate 4.4: Coordinate Measuring Machine (CMM)

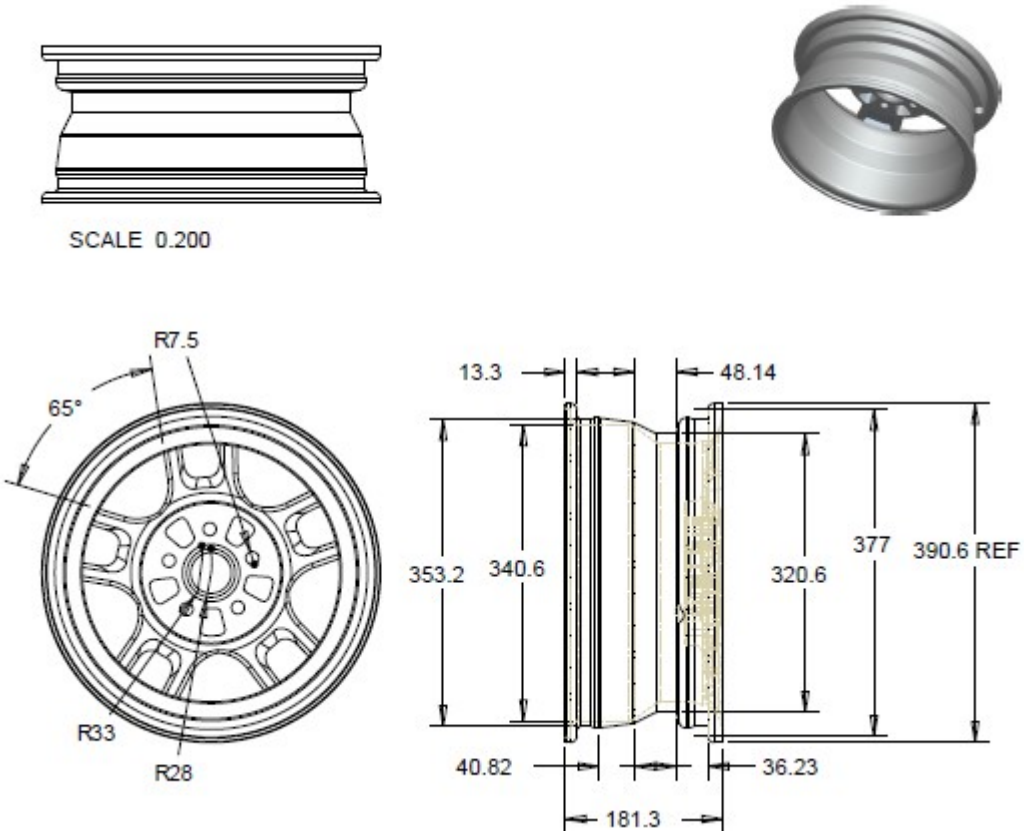

Fig 4.1: Wheel dimensions

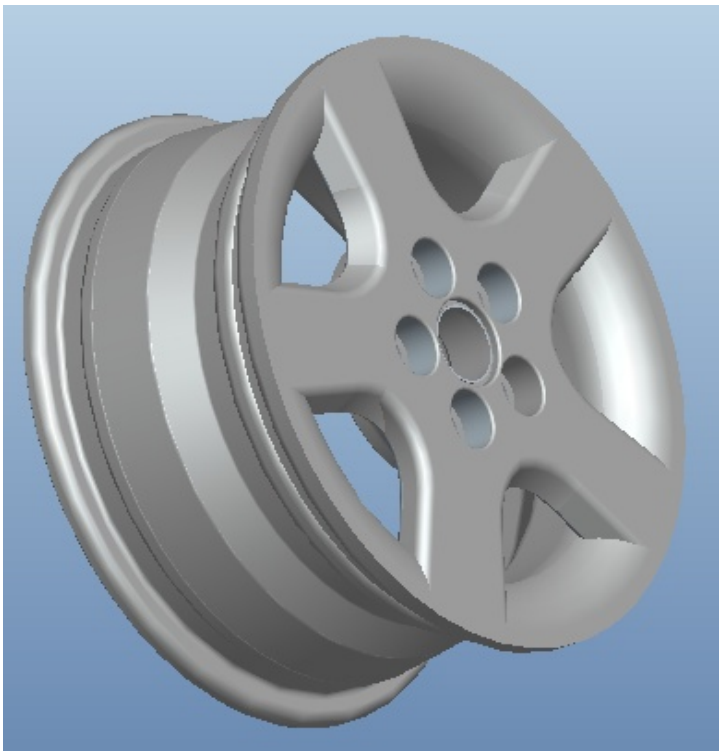

Fig.: 4.2: 3-D Numerical model outboard view

Fig.: 4.3: 3-D wheel model Inboard view

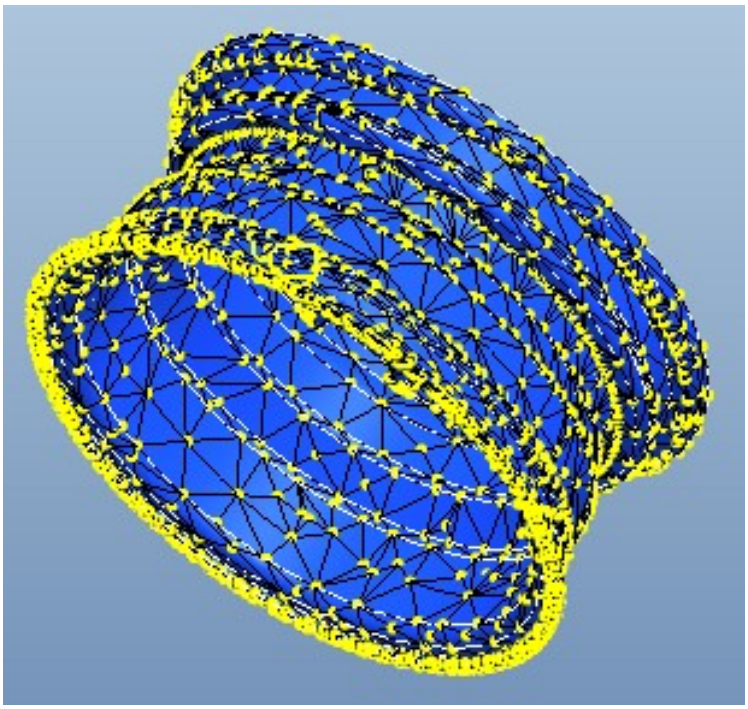

Fig. 4.4: 3-D wheel model mesh

Table 4.3: Relation between contact patch length and radial load distribution angle at radial load of 450 N and 3570 N

Wheel Type	Tyre Aspect Ratio	Radial Load (N)	Inflation Pressure (MPa)	Radial load Distribution Angle (Deg)
6JX14H2 ET 42	175/60 R14	4750	0.3	29
			0.15	34
		3570	0.3	26
			0.15	32

4.2 OBSERVATIONS AT WHEEL'S LOCATIONS OF INBOARD BEAD SEAT, WELL AND OUTBOARD BEAD SEAT

Figures 4.5 to 4.40represent plots, of the maximum principal strains, maximum principal stresses and Von-Mises stresses at circumferential angles between 0 and 180 degree at locations of the inboard bead seat, well and outboard bead seat for the experimental and FE values of experimental wheel at contact angle of 30.25 degree in comparison with literature values at 40 and 90 degree.

4.2.1 OBSERVATION AT THE INBOARD BEAD SEAT

4.2.2 Maximum Principal Strain

Figures 4.5and4.6 show plots at the inboard bead seat, of the maximum principal strain experimental results and the FE results at different loading angles of 90 degree eye bar function (EBF), 40 degree cosine function (CF) and experimental contact angle of 30.25 degrees (ECA) at 4750 N radial load and different inflation pressure of 0.3 and 0.15 MPa, respectively.

Figure 4.5 illustrates the relationship, at inboard bead seat, between the experimental and FE on the induced maximum principal strain at 4750 N radial load and 0.3 MPa inflation pressure. All plots exhibit negative slopes between 0 and 40 degree locations. There was no obvious difference between the experimental and 40 degree CF at 40 degree circumferential angular location and between the experimental and FE values at 110 degree location. Between 40 and 110 degree locations, the curves assumed identical characteristics. The highest maximum principal strain values were about 1.85×10^{-4} , 1.38×10^{-4}, 4.51×10^{-4} and 5.69×10^{-4} mm/mm, respectively for the experimental, 90 degree EBF, 40 degree CF and ECA. All strain values were less than the yield strain value of about 1.00×10^{-2} in simple tension test.

Figure 4.6 explains the relationship between experimental and FE on the induced maximum principal strain at 4750 N radial load and 0.15 MPa inflation pressure at the inboard bead seat. Negative slopes were observed for all curves between 0 and 40 degree locations on the wheel. There was no obvious difference between experimental and Fe values at 40 degree angular location. but for the 90 degree which may be due to its larger

load distribution angle. The values at ground contact represent the highest induced maximum principal strain values of about 1.76×10^{-4}, 1.29×10^{-4}, 2.53×10^{-4} and 5.26×10^{-4} mm/mm, respectively, for experimental, 90 degree EBF, 40 degree CF and ECA. As with Figure 4.5, strain values were less than the yield strain value of about 1.00×10^{-2} in simple tension test.

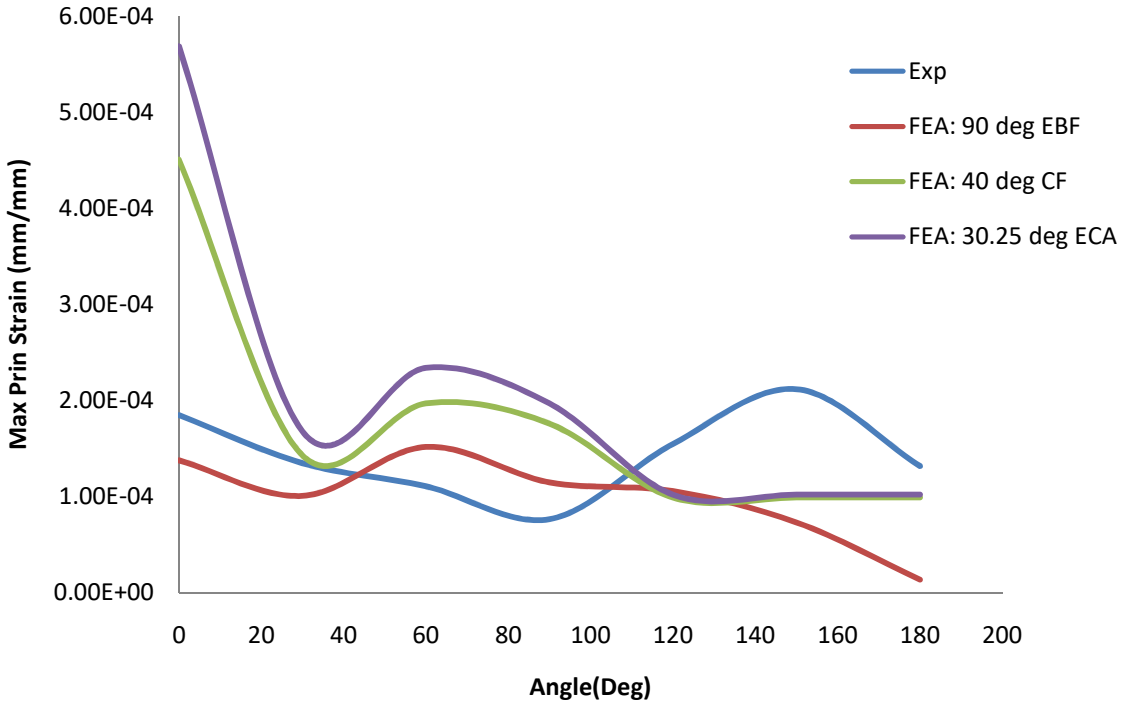

Fig.4.5:Maximum Principal Strain Results at the Inboard Bead Seat: Experimental versus FEA at 4750 N Radial Load and 0.3 MPa Inflation Pressure.

**(Yield strain = 1 x 10^{-2} mm/mm)*

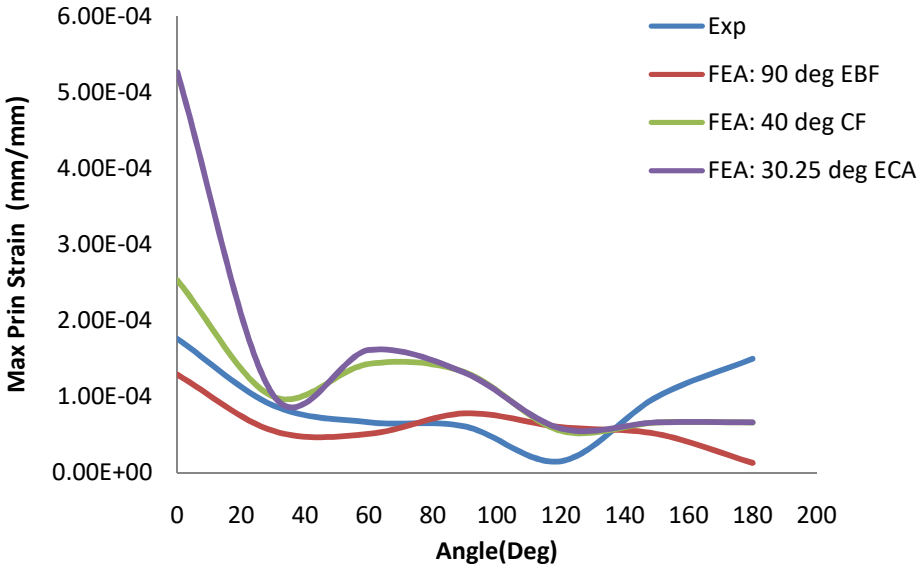

Fig.4.6: Maximum Principal Strain Results at the Inboard Bead Seat: Experimental versus FEA at 4750 N Radial Load and 0.15 MPa Inflation Pressure.

Figures 4.7and4.8 show plots at the inboard bead seat, of the maximum principal strain experimental results and the FE results at different loading angles of 90 degree eye bar function (EBF), 40 degree cosine function (CF) and experimental contact angle (ECA) 30.25 degree at 3570 N radial load and inflation pressure of 0.3 and 0.15 MPa, respectively.

Figure 4.7 shows the connection, at inboard bead seat, between the experimental and FE on the induced maximum principal strain at 3570 N radial load and 0.3 MPa inflation pressure. All four curves exhibited negative slopes between 0 and 30 degree locations. There were no significant difference between experimental and FE values at location 30 degree location and locations between 120 and 160 degree. The highest induced maximum principal strain values were about 1.36×10^{-4}, 0.86×10^{-4}, 2.53×10^{-4} and 5.26×10^{-4} mm/mm, respectively for the experimental, 90 degree EBF, 40 degree CF and ECA.

Figure 4.8 demonstrates relation between experimental and FE on the induced maximum principal strain at 4750 N radial load and 0.15 MPa inflation pressure at the inboard bead seat. The predominance of the influence of loading angle distribution was apparent at 0 degree location. However, between locations of 150 and 160 degree, there was a marginal disparity between maximum principal strain values. Between 0 and 40 degree locations there was an inverse relationship between the induced maximum principal strain and location distance from the point of contact of the wheel with the ground for all four curves exhibit. As with Figure 4.1, strain values were less than the yield strain value of about 1.00×10^{-2} in simple tension test

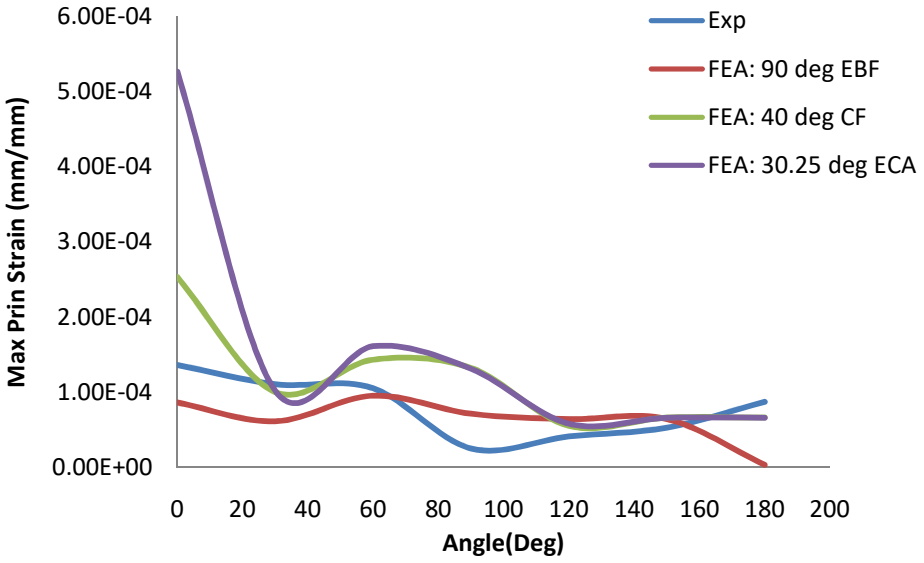

Fig.4.7: MaximumPrincipal Strain at the Inboard Bead Seat: Experimental versusFEA at 3570 N Radial Load and 0.3 MPa Inflation Pressure.

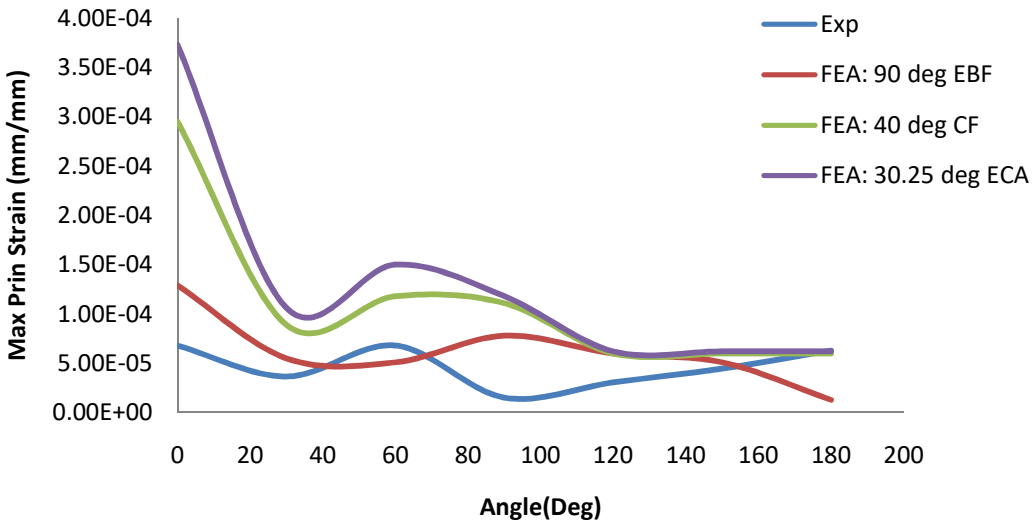

Fig. 4.8 : Maximum Principal Strain Results at the Inboard Bead Seat: Experimental versus FEA at 3570 N Radial Load and 0.15 MPa Inflation Pressure.

4.2.3 Maximum Principal Stress

Figures 4.9-4.10 represents the graphs of experimental maximum principal stress values with that of the FE values (90 degree EBF, 40 degree CF and ECA) at 0.3 and 0.15 MPa inflation pressure respectively, at 4750 N radial load.

Figure 4.9 shows the correlation at inboard bead seat, between the experimental and FE on the induced maximum principal stress at 4750 N radial load and 0.3 MPa inflation pressure. Each curve presents a negative slope, with the 30.25 degree ECA and 40 degree CF steeper than that of the experimental and 90 degree EBF. There was no obvious difference between the experimental and 30.25 degree values at 0 degree location. The experimental curve values predominates between 10 and 180 degree locations. This may be due to the strain rosette setting.

Figure 4.50 represents values of maximum principal stress at inboard bead seat at 4750 N radial load and 0.15 inflation pressure. All four plots showed negative slopes between 0 and 30 degree locations, with the 30.25 degree ECA and 40 degree CF curves steeper than experimental and 90 degree EBF. There was no significant difference between experimental and 40 degree CF values at 0 degree and between 50 and 120 degree locations. There was significant difference between the experimental and the FE values between 20 and 50 degree and between 130 and 180 degree locations, with experimental values higher than the FE values. This may have been caused by sensitivity of the gages in those locations. All maximum principal stress values were less than the yield stress value of about 222.5 MPa.

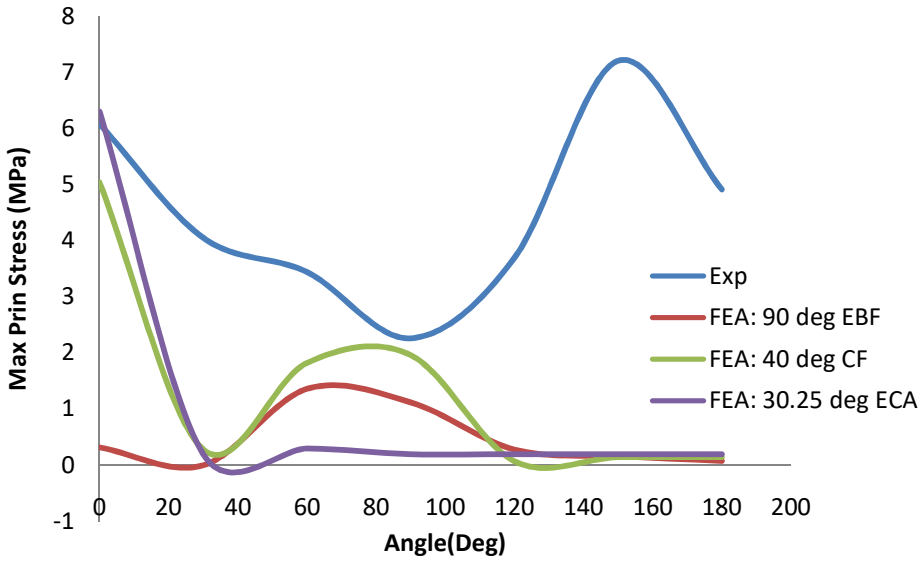

Fig.4.9: Maximum Principal Stress Results at the Inboard Bead Seat: Experimental versusFEA at 4750 N Radial Load and 0.3 MPa Inflation Pressure.

**(Yield stress = 222.5 MPa)*

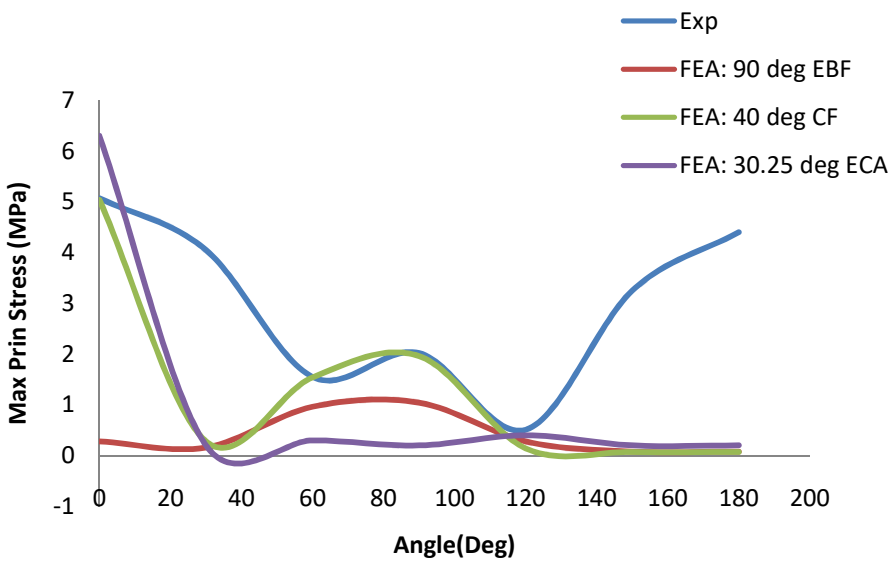

Fig. 4.10:Maximum Principal Stress Results at the Inboard Bead Seat: Experimental versusFEA at 4750 N Radial Load and 0.15 MPa Inflation Pressure.

Figure 4.11, at 0.3 MPa inflation pressure and 3570 N radial load, the experimental ground contact maximum principal stress value was about 3.25 MPa, while those of the FE - 90 degree EBF, 40 degree CF and ECA - were about 0.25, 3.93 and 4.78 MPa, respectively. Their highestmaximum principal stress values were about 3.25,1.27, 3.93 and 4.78 MPa, respectively. While the highest induced experimental value and those of 40 degree CF and ECA were at ground contact, that of the 90 degree EBF was at 60 degree circumferential angular location. The slope of the coves between 0 and 30 degree locations were negative. The FE values flattened out between 140 and 180 degree and approaching values of about 1.04, 0.08, and 0.20 MPa, respectively for the 90 degree EBF, 40 degree CF and ECA. That of the experimental curve rose to a value of about 2.84 MPaat 180 degree location.

From Figure 4.12 and at inflation pressure of 0.15 MPa at 3570 N radial load, the highest maximum principal stress values were about 2.02 MPa for the experimental condition. Corresponding FE values were about0.60,2.77 and 4.01 MPa for 90 degree EBF, 40 degree CF and ECA, respectively. The experimental ground location maximum principal stress valuewas about 2.02 MPa, while those of the FE - 90 degree EBF, 40 degree CF and ECA - were about 0.18 MPa, 2.77 MPa and 4.01 MPa, respectively. The curves assume the same characteristics as that of Figure 4.11.

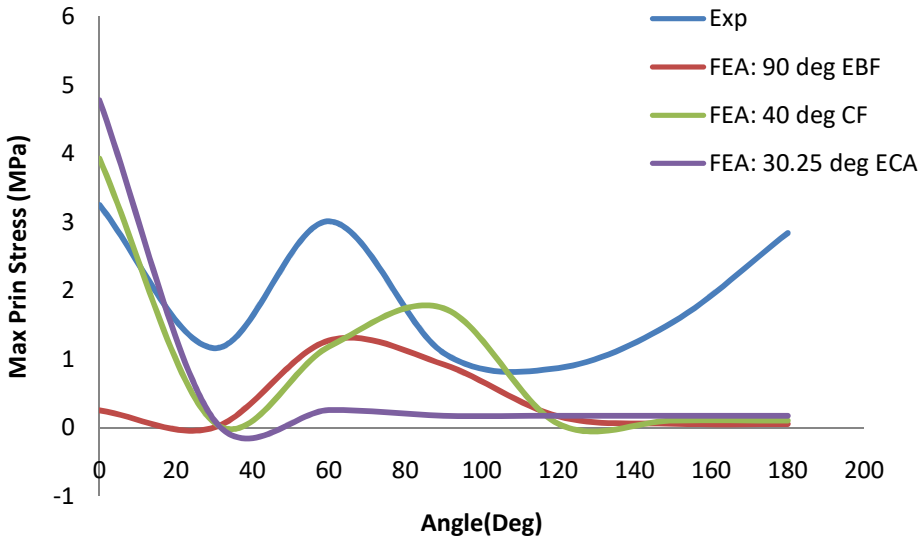

Fig. 4.11: Maximum Principal Stress Results at the Inboard Bead Seat: Experimental versusFEA at 3570 N Radial Load and 0.3 MPa Inflation Pressure.

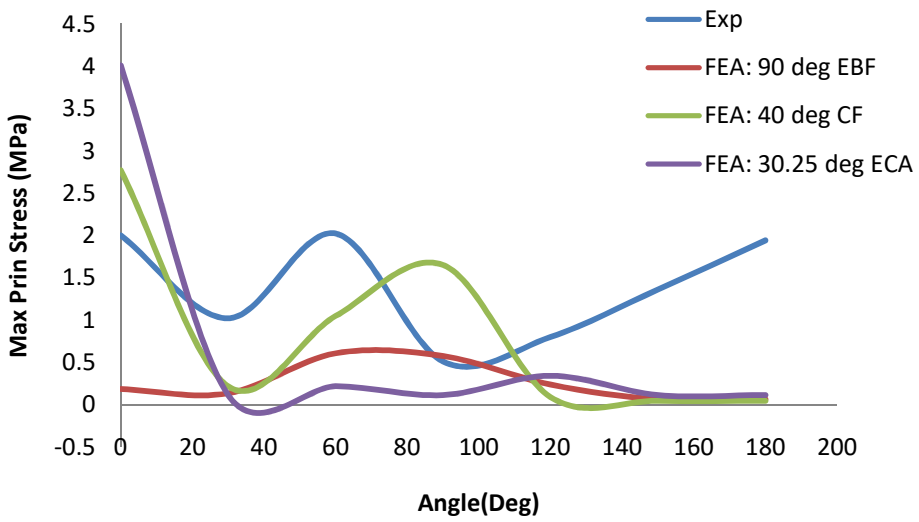

Fig. 4.12: Maximum Principal Stress Results at the Inboard Bead Seat: Experimental versusFEA at 3570 N Radial Load and 0.15 MPa Inflation Pressure.

4.2.4 Von-Mises Stress

Figure 4.13 - 14 show the plots of the Von-Mises stresses of both the experimental and the FE results at the inboard bead seat at different inflation pressure and loading conditions.

Figure 4.13 explains relationship between experimental and FE on the induced Von-Mise stress values at 4750 N radial load and 0.3 MPa inflation pressure at the inboard bead seat. Every curve exhibiting negative slope between 0 and 30 degree locations, with the 90 degree EBF almost horizontal and depicting constant stress within the range. There influence of the load distribution angle on the values at 0 degree contact angle obvious was evident. There was no significant variation between experimental and FE values at 30 degree and between 100 and 130 degree locations. There was only a marginal difference between the experimental and FE values of about 3%.

Figure 4.14 represents the plots of values of the Von-Mises stresses at 015 MPa inflation pressure. The curves maintain constant gradient between 0 degree location and 30 degree location. The Von-Mises stress values at 0 degree angular location for experimental, 90 degree EBF, 40 degree CF and ECA were about 7.18, 3.68, 8.06and 10.50 MPa, respectively. There was a marginal difference between the experimental and FE values for both 40 degree CF and 30 degree CF at locations between 40 and 120 degree locations. While the FE curves approachtheir respective constantvaluesbetween 130 and 180 degree locations, that of the experimental was increasing; an indication that there might be some error in either strain rosette placement or reading.

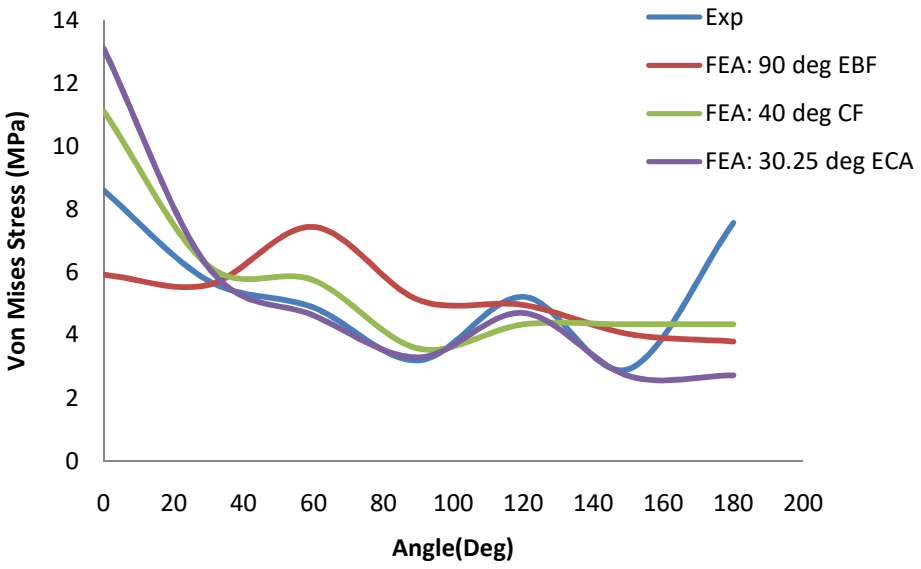

Fig. 4.13: Von Mises Stress Results at the Inboard Bead Seat: Experimental versus FEA at 4750 N Radial Load and 0.3 MPa Inflation Pressure.

**(Yield stress = 222.5 MPa)*

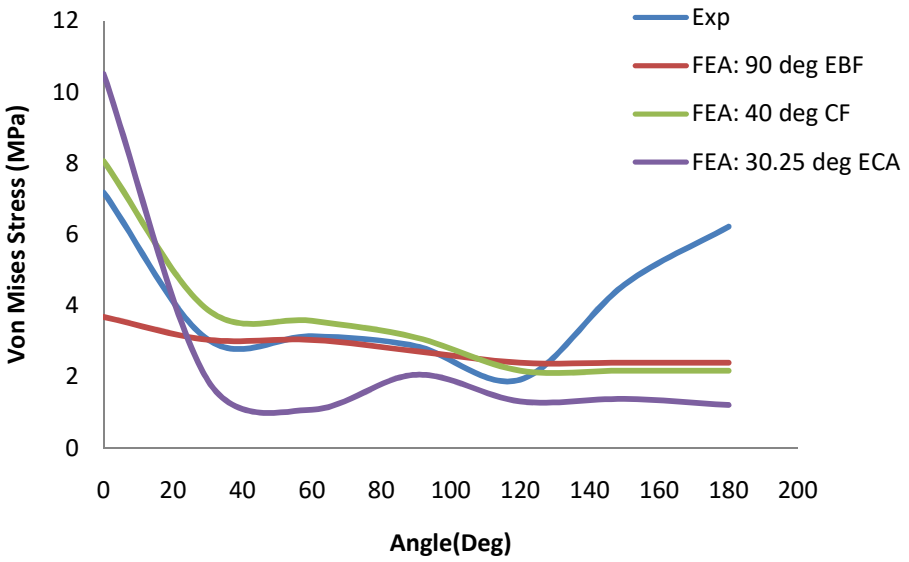

Fig.4.14 : Von Mises Stress Results at the Inboard Bead Seat: Experimental versus FEA at 4750 N Radial Load and 0.15 MPa Inflation Pressure.

Figure 4.15-4.16 show the plots of the Von-Mises stresses of both the experimental and the FE results at the inboard bead seat at different inflation pressure and 3570 N radial load loading conditions. At 0.3 MPa, Figure 4.11, it was observed that at ground contact, Von_Mises stress values were 5.63, 1.52, 7.44 and 7.27 MPa, respectively. for experimental, 90 degree EBF, 40 degree CF and ECA. Their corresponding mean Von-Mises stresses were about 2.33, 0.64, 1.71 and 2.19 MPa respectively. The Von - Mises stress values at ground contact represent their respective peak values. The curve assumed the same attributes as those of Figure 10, between 130 and 180 degree locations.

Figure 4.16 represents the curves at 0.15 MPa inflation pressure, at the inboard bead seat, of the Von-Mises stress values, for both the empirical and FE values of 90 degree EBF, 40 degreeCF and ECA at 3570 N radial load. The results showed that at ground contact, the experimental value of the Von-Mises stress was about 2.86 MPa. Corresponding FE values for 90 degree EBF, 40 degree CF and ECA wereabout 1.23, 5.34 and 5.02 MPa, respectively. These values represented their corresponding highest induced values. In the same order as the values at ground contact, the mean Von-Mises stresses were about, 1.96 MPa, for experimental0.44 MPa and corresponding FE values were 1.09 and 1.56, respectivelyfor 90 degree EBF, 40 degree CF and ECA. The curve assumed the same attributes as those of Figure 10, between 130 and 180 degree locations.

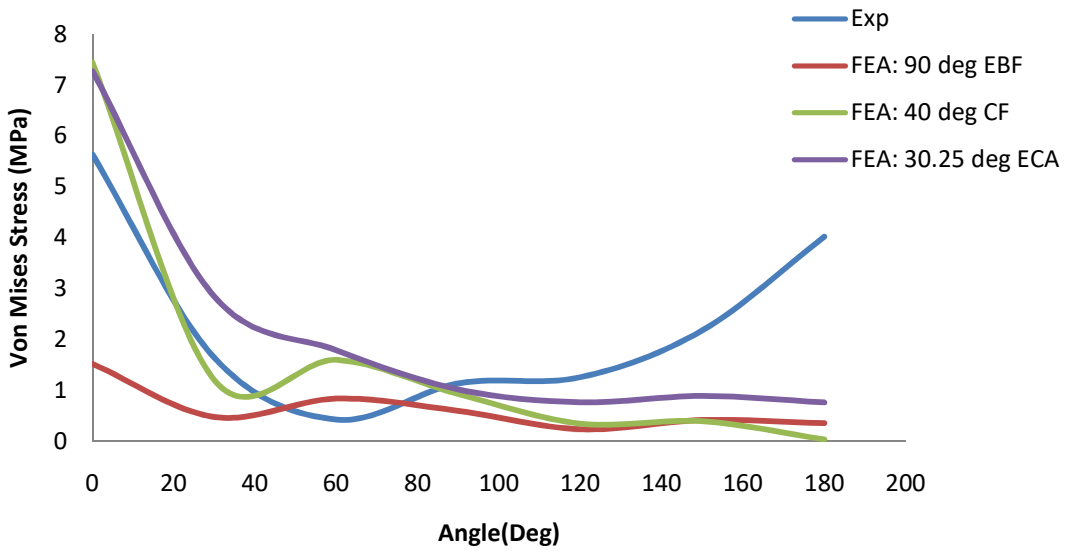

Fig.4.15: Von Mises Stress Results at the Inboard Bead Seat: Experimental versus FEA at 3570 N Radial Load and 0.3 MPa Inflation Pressure.

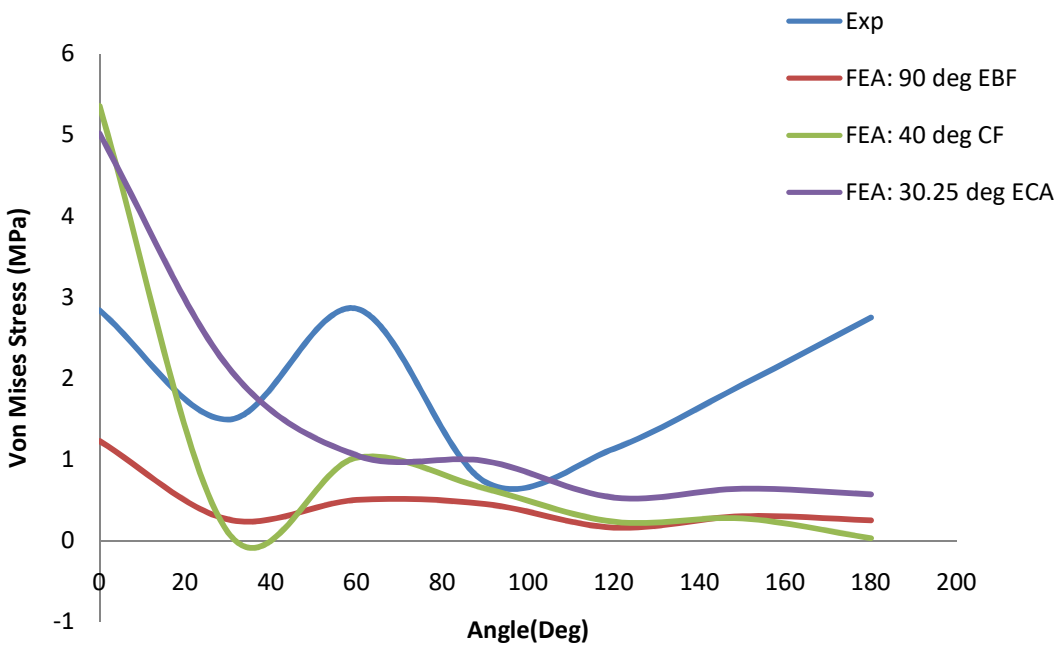

Fig.4.16: Von Mises Stress Results at the Inboard Bead Seat: Experimental versus FEA at 3570 N Radial Load and 0.15 MPa Inflation Pressure.

4.3 OBSERVATION AT THEWELL

4.3.1 Maximum Principal Strain

Figures 4.17 - 4.18 represent the graphic view of the maximum principal strain at the well at different inflation angles and loading conditions for both experimental and FE.

Considering Figure 4.17 and at 0.3 MPa inflation pressure, the maximum principal stress values at the well were respectively, about 1.11 x 10^{-4}, 4.30 x 10^{-4}, 5.O7 x 10^{-4} and 5.66 x 10^{-4} mm/mm, for the experimental, 90 degree EBF, 40 degree CF and ECA.The highest and mean experimental maximum principal strain values were lower than the FE values between 0 and 180 degree angular locations. All the curves exhibit downward slopes from 0 to 30 degree locations. The values at ground contact represent the maximum principal strain values for the FE curves, while that for the FE curves, while that of the experimental curve occur location, with a value of about 2.11 mm/mm. The shape of the curves assume the same characteristics.

Figure 4.18 shows the maximum principal strain values at the well at 0.15 MPa inflation pressure. It was observed that at between 0 and 30 degree locations the FE curves assumed negative slopes, while experimental curve was positive. Experimental values were higher than those of the FE values between 30 and 180 degree locations.

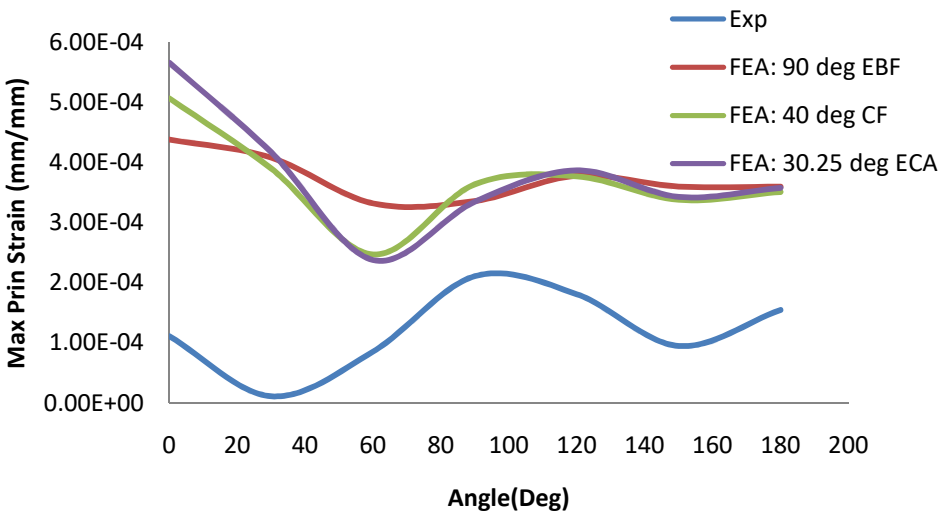

Fig.4.17: Maximum Principal Strain Results at the Well : Experimental versus FEA at 4750 N Radial Load and 0.3 MPa Inflation Pressure.

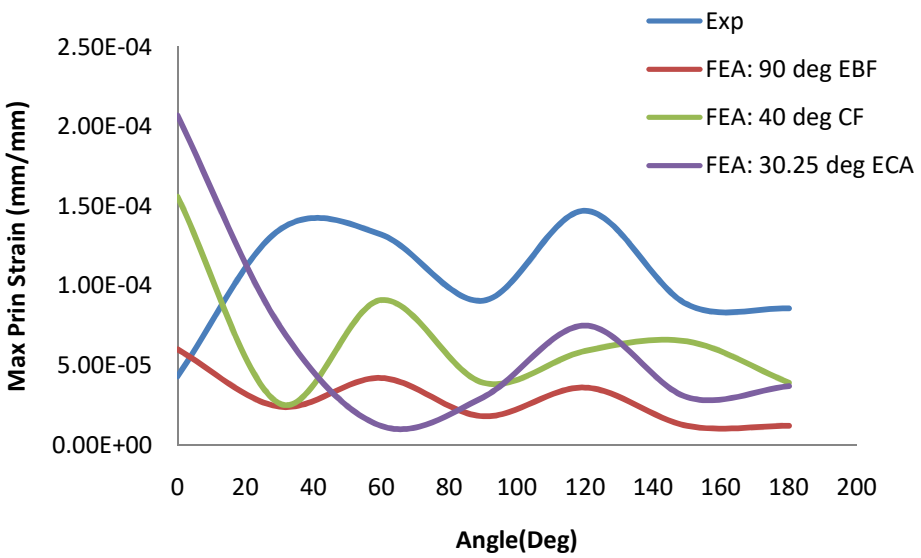

Fig. 4.18: Maximum Principal Strain Results at the Well : Experimental versus FEA at 4750 N Radial Load and 0.15 MPa Inflation Pressure.

Figures 4.19 - 4.20 represent the graphic view of the maximum principal strain at the well at different inflation angles and loading conditions for both experimental and FE at 3570 N radial load.

Figure 4.19 shows the plot of the induced maximum principal strain at the well at 3570 N radial load and 0.3 MPa inflation pressure. There was a significant influence of loading angle at 0 degree location. The mean difference between the experiment and FE values lie between 8% and 32 %, depending on the loading angle, which was insignificant going by the induced maximum principal strain which is in the order of 10^{-4}. The highest induced maximum principal strain values were less than the yield strain value of about 1x 10^{-2} mm/mm.

Figure 4.20 depicts the curves of the principal strain at the well at 3570 N radial load and 0.15 MPa inflation pressure. At ground contact, there was an obvious difference between the FE values of 30.25 degree ECA and 40 degree CF. However, there was negligible variation between experimental 90 degree EBF values. Experimental and FE values were the same at different locations between 0 and 180 degree locations. The highest induced maximum principal strain values were about 0.73 x 19^{-4}, 0.47 x 19^{-4}, 1.2 x 19^{-4} and 1.62 x 19^{-4} mm/mm, respectively for the experimental, 90 degree EBF, 40 degree CF and 30 degree CF.

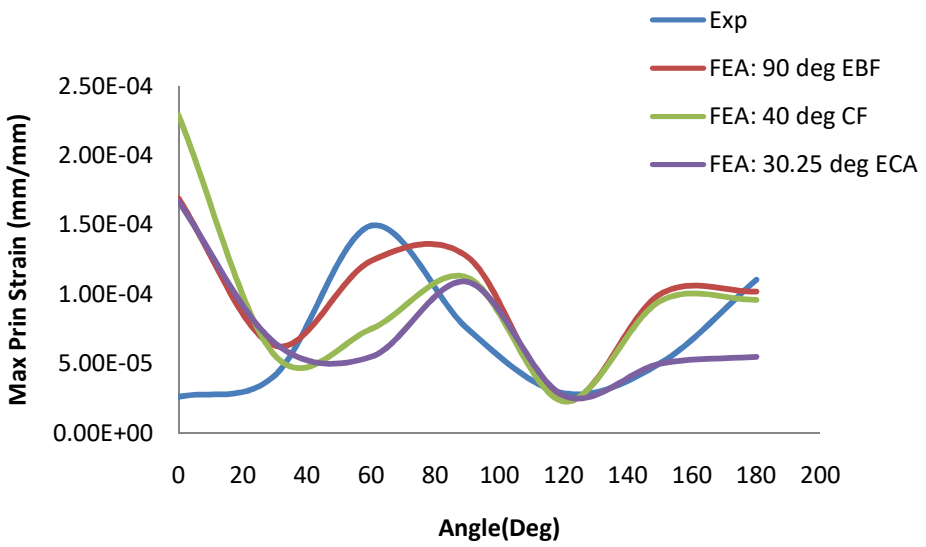

Fig. 4.19: Maximum Principal Strain Results at the Well: Experimental versus FEA at 3570 N Radial Load and 0.3 MPa Inflation Pressure.

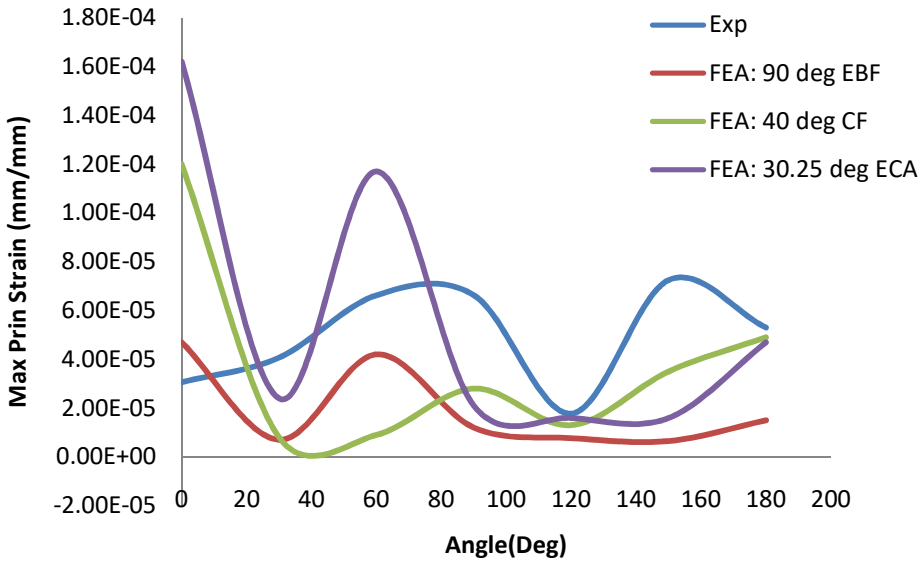

Fig. 4.20: Maximum Principal Strain Results at the Well: Experimental versus FEA at 3570 N Radial Load and 0.15 MPa Inflation Pressure.

4.3.2 Maximum Principal Stress

Figure 4.21- 4.22 represent the values, at the well, of the maximum principal stresses of the experimental and the FE values of 90 degree EBF, 40 degree CF and ECA at inflation pressure of 0.3 and0.15 MPa, respectively at 4750 N radial load.

Figure 4,21 shows the curves of the principal strain at the well at 4750 N radial load and 0.3 MPa inflation pressure. There was an obvious influence of the loading angle between the maximum principal stress values of experimental and FE at 0 degree location, with each curve exhibiting negative slope between 0 and 30 degree locations. Each curve approaches respective constant values between 150 and 180 degree locations, with lower and same values for experimental and 40 degree CF within the range.

Figure 4.22 shows the plots of experimental values against the FE values at 0.15 MPa inflation pressure. It was observed that the maximum principal stress values at 0 degree angle location of the wheel were about 1.09, 5.94, 8.37 and 10.54 MPa, respectively for the experimental, 90 degree EBF, 40 degree CF and ECA. These values also represented their respective peak maximum principal stress, except for that of the experimental, whose largest value was about 5.17 MPa at 120 degree location. At locations of about 40 and 90 degree angular locations, the experimental values approach the FE values at 30 and 110 degree locations, except for the 90 degree EBF. The values at these points are about 4.40 and 5.00 MPa respectively. The experimental mean maximum principal stress value was about 3.17 MPa. Corresponding FE values for 90 degree EBF, 40 degree CF and ECA were about 4.30, 4.32 and 4.64 MPa respectively. The FE curves slopes downwards between 0 and 30 degree locations, while that of the experimental curve slopes upwards within this range.

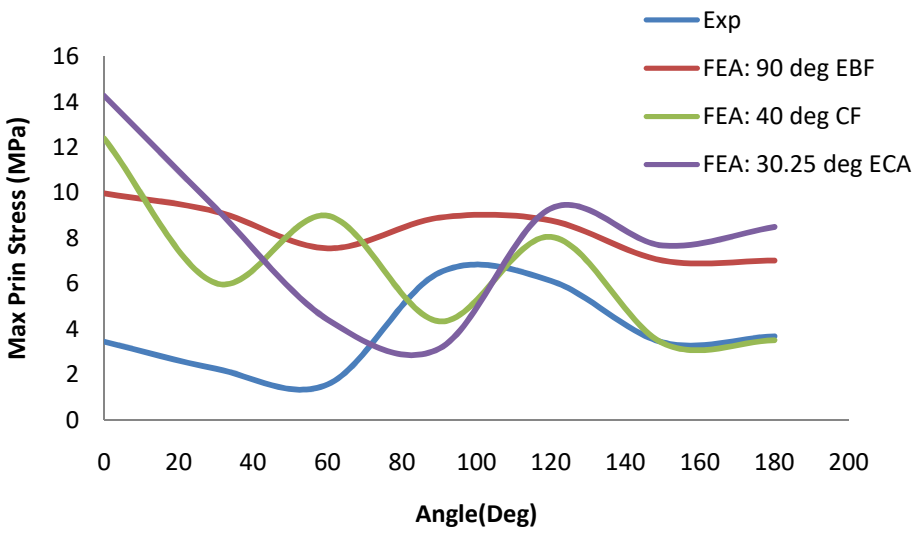

Fig.4.21: Maximum Principal Stress Results at the Well: Experimental versus FEA at 4750 N Radial Load and 0.3 MPa Inflation Pressure.

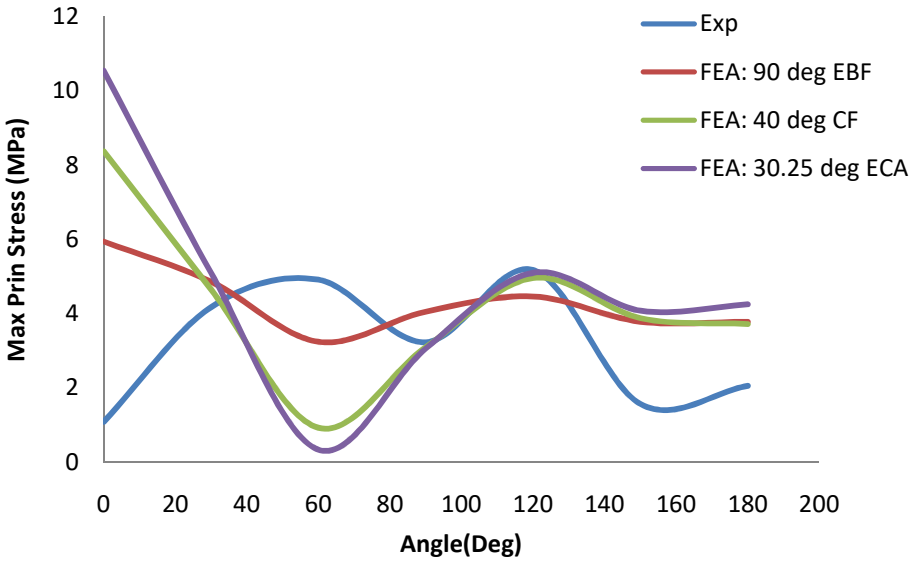

Fig.4.22: Maximum Principal Stress Results at the Well: Experimental versus FEA at 4750 N Radial Load and 0.15 MPa Inflation Pressure.

Figure 4.23and4.24 represent the values, at the well, of the maximum principal stresses of the experimental and the FE values of 90 degree EBF, 40 degree CF and ECA at inflation pressure of 0.3 and 0.15 MP respectively at 3570 N radial load.

Figure 4.23 illustrates the induced maximum principal stress at the well at 3570 N radial load and 0.3 MPa inflation pressure. The highest maximum principal stress values for all four plots were at 120 degree locationm with values of about 7.71, 11.02, 10.01 and 11.72 MPa, respectively for the experimental, 90 degree EBF, 40 degree CF and 30.25 degree ECA. The shape of the curves assume approximately the same attributes as that of Figure 4.18 between 150 and 180 degree location.

Figure 4.24 explains relationship between experimental and FE values on the induced maximum principal stress at 3570 N radial load and 0.15 MPa inflation pressure at the well. The shape of the curves were similar to that of Figure 4.19, but with higher values at the point of contact of the wheel with ground. This could probably be due to the fact that the wheel tends to ovalise at lower inflation pressure, with maximum induced stress tending to be at 0 degree location.

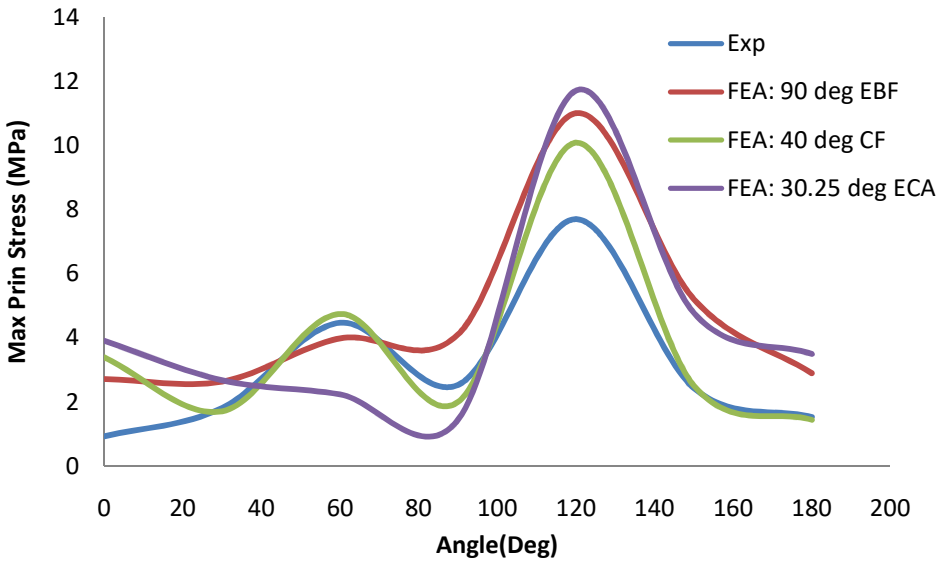

Fig. 4.23: Maximum Principal Stress Results at the Well: Experimental versus FEA at 3570 N Radial Load and 0.3 MPa Inflation Pressure.

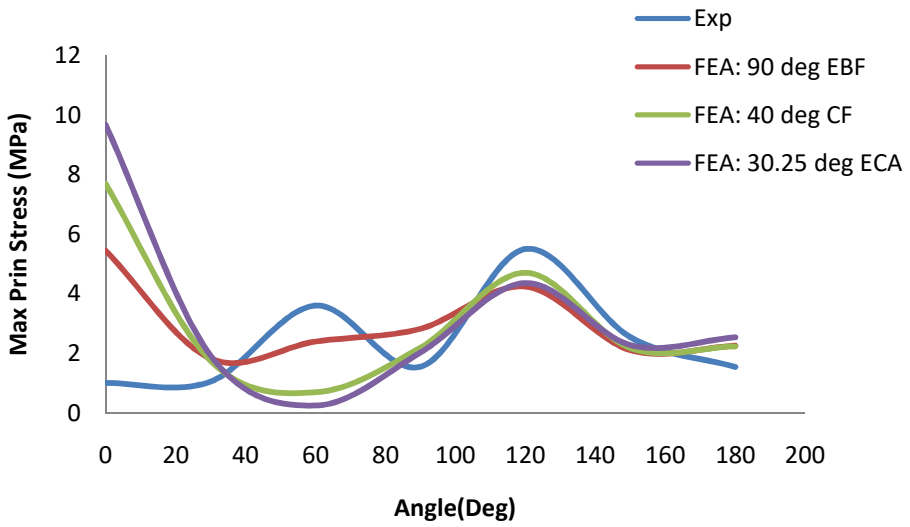

Fig. 4.24: Maximum Principal Stress Results at the Well: Experimental versus FEA at 3570 N Radial Load and 0.15 MPa Inflation Pressure.

4.3.3 Von-Mises Stress

Figures 4.25 - 4.26 show the curves of the Von-Mise stresses of both expirical and FE results at different inflation pressure of 0.3 and 0.15MPa respectively at a radial load of 4750 N.

Figure 4.25 shows the relationship between experimental and FE values of the Von-Mises stress at the well at 4750 N radial load and 0.3 MPa inflation pressure. The FE curves depicts negative slopes between 0 and 30 degree locations; that of the experimental was positive within the range. There was an obvious influence of the load distribution angle on the maximum induced Von-Mises between the experimental and FE values at 0 degree contact angle. The maximum induced Von-Mises stresses were about 9.19, 9.45, 12.40 and 12.90 MPa, respectively for the experimental, 90 degree EBF, 40 degree CF and 30.25 ECA. However, there was a marginal difference in their corresponding mean values of about 6.29, 8.52, 7.75, and 6,75 MPa, respectively.

Figure 4.26 represent the Von-Mises stress at the well curves at 4750 N radial load and 0.15 MPa inflation pressure. The character of the curves between 0 and 30 degree locations was the same with that of Figure 4.25. The experimental values dominate between locations of 30 and 140 degree. The influence of loading angle distribution affects the magnitude of the stress at 0 degree location; but marginal at 180 degree location. The maximum induced Von-Mises stresses were about 7.23, 5.40, 8.37 and 9.00 MPa, respectively for the experimental, 90 degree EBF, 40 degree CF and 30.25 ECA, with corresponding mean values of about 4.47, 4.32, 4.23 and 4.68 MPa, respectively.

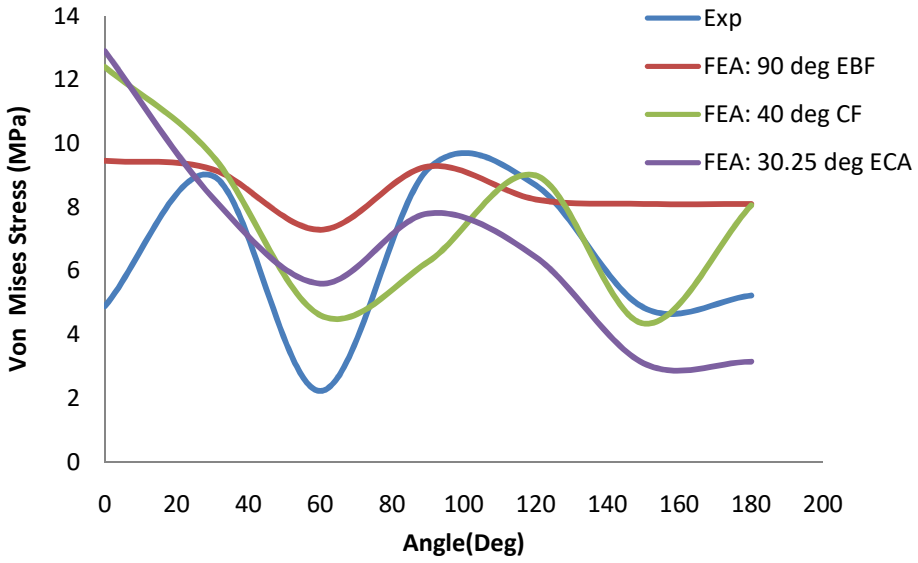

Figure 4.25: Von Mises Stress Results at the Well: Experimental versus FEA at 4750 N Radial Load and 0.3 MPa Inflation Pressure.

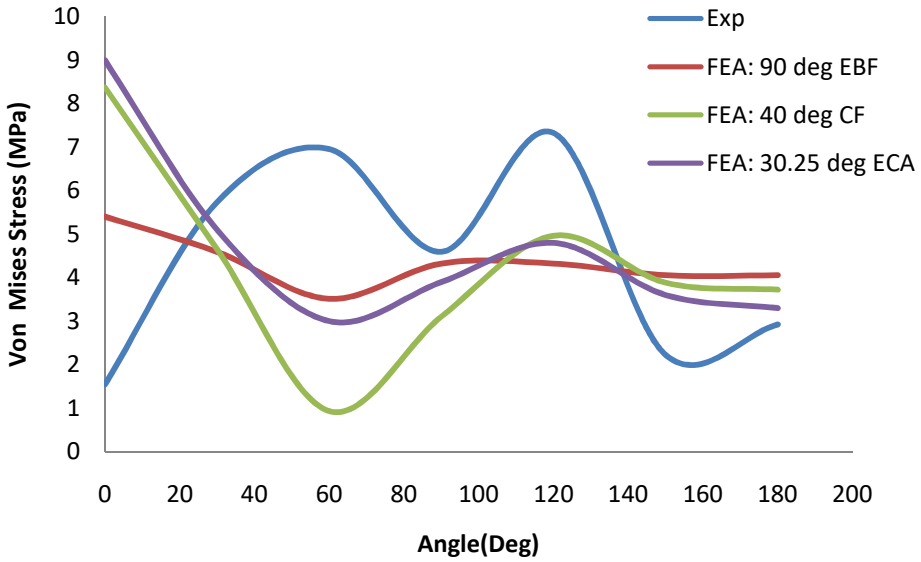

Fig.4.26: Von Mises Stress Results at the Well: Experimental versus FEA at 4750 N Radial Load and 0.15 MPa Inflation Pressure.

Figures 4.27 - 4.28 show the curves of the Von-Mise stresses of both empirical and FE results at different inflation pressure of 0.3, and 0.15MPa, respectively at a radial load of 3570 N.

Figure 4.27 represents the curves at 0.3 MPa inflation pressure, at the well, of the Von-Mises stress values for both the empirical and FE values of 90 degree EBF, 40 degree CF and ECA at 3570 N radial load. The results showed that at ground contact, the experimental value of the Von-Mises stress was about 1.32 MPa; for 90 degree EBF, about 4.98 MPa; about 7.72 MPa for 40 degree CF and about 8.29 MPa for ECA. These values signified their corresponding highest values, except for the experimental whosehighest value was about 6.33 MPa at 60 degrees contact angle. In the same order as the values at ground contact, the mean Von-Mises stresses were about, 3.57, 3.08, 3.14 and 3.49 MPa, respectively.

Figure 4.28 shows the plots of Von-Mises stress at the well at 3570 N radial load and 0.15 MPa inflation pressure. All four plots exhibit gradual slope between 0 and 40 degree locations. They all assumed maximum stress values at 60 degree location. There was no obvious difference between experimental and FE values between 40 and 180 degree locations, except that of 90 degree EBF between 120 and 170 degree locations

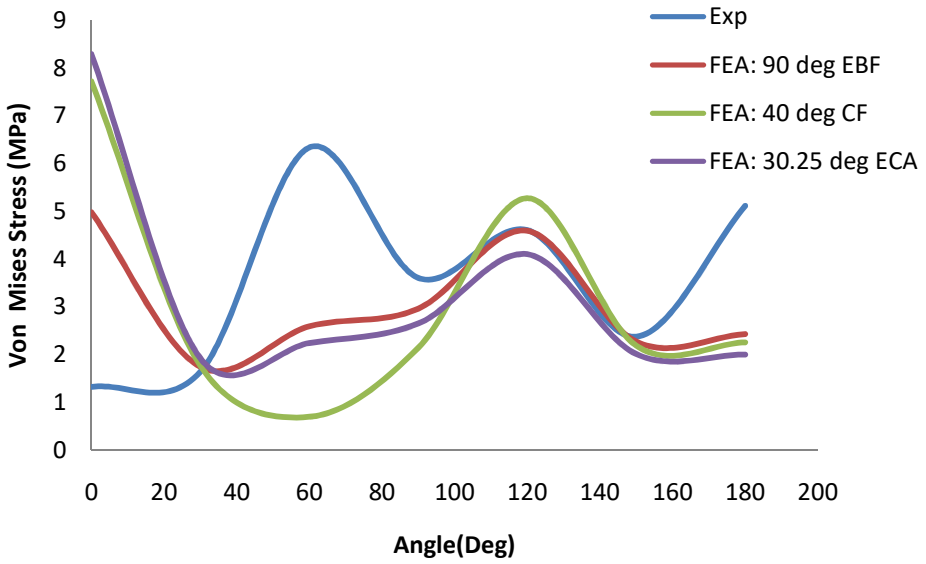

Fig. 4.27: Von Mises Stress Results at the Well: Experimental versus FEA at 3570 N Radial Load and 0.3 MPa Inflation Pressure.

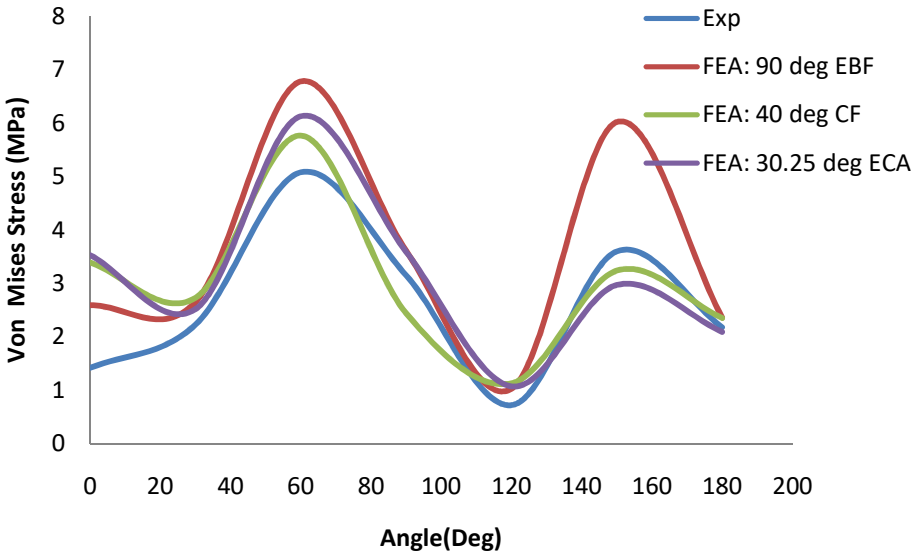

Fig.4.28: Von Mises Stress Results at the Well: Experimental versus FEA at 3570 N Radial Load and 0.15 MPa Inflation Pressure.

4.4 OBSERVATION AT THE OUTBOARD BEAD SEAT

4.4.1 Maximum Principal Strain

Figures 4.29 - 4.30 represent plots of the maximum principal strain at the wheel's outboard bead seating surface at different inflation pressure of 0.3 and 0.15 MPa, respectively at 4750 radial load.

From Figure 4.29, at 0.3 MPa, at ground contact angle, the empirical maximum]principal strain value was about 2.22 x 10^{-4} mm/mm, while the FE values were about, 0.30 x 10^{-4}, 0.43 x $10^{-4}$and 0.49 x 10^{-4} mm/mm, respectively for 90 degree EBF; 40 degree CF and ECA. Their corresponding mean maximum principal strain values are about 1.00 x 10^{-4}, 0.50 x 10^{-4}, 0.64 x 10^{-4} and 0.84 x 10^{-4} mm/mm respectively. The respective largest maximum principal stress values were 2.46 x 10^{-4}, 0.54 x 10^{-4}, 0.99 x 10^{-4} and 1.56 x 10^{-4}mm/mm for experimental, 90 degree EBF,40 degree CF and ECA. The greatest value for the experimental curve was at ground contact, 120 degree location for 40 degree CF, while that for the 90 degree EBF and ECA were each at angular location of 150 degree. The experimental maximum principal strain coincides with the FE values at different locations on the wheel's rim. The slope of the experimental curve was negative between 0 and 30 degree locations, while the FE curves assume negative slope within this range/

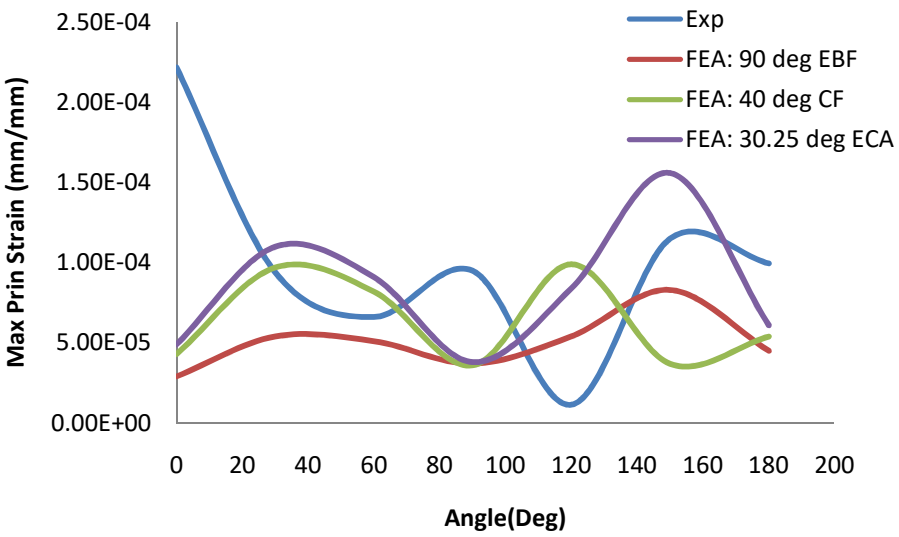

Fig.4.29: Maximum Principal Strain Results at Outboard Bead Seat: Experimental versus FEA at 4750 N Radial Load and 0.3 MPa Inflation Pressure.

Figure 4.30 illustrate the plots of the maximum principal strain results at the outboard bead seat at 4750 N radial load and 0.15 MPa inflation pressure. The experimental curve exhibited a negative slope between 0 and 60 degree locations, while the FE curves showed positive slopes between 0 and 30 degree locations. The wavy shape of the curves was probably due to the wheel's arms and their orientation around the outboard. The experimental and FE values were the same at different locations depending on the load distribution angle.

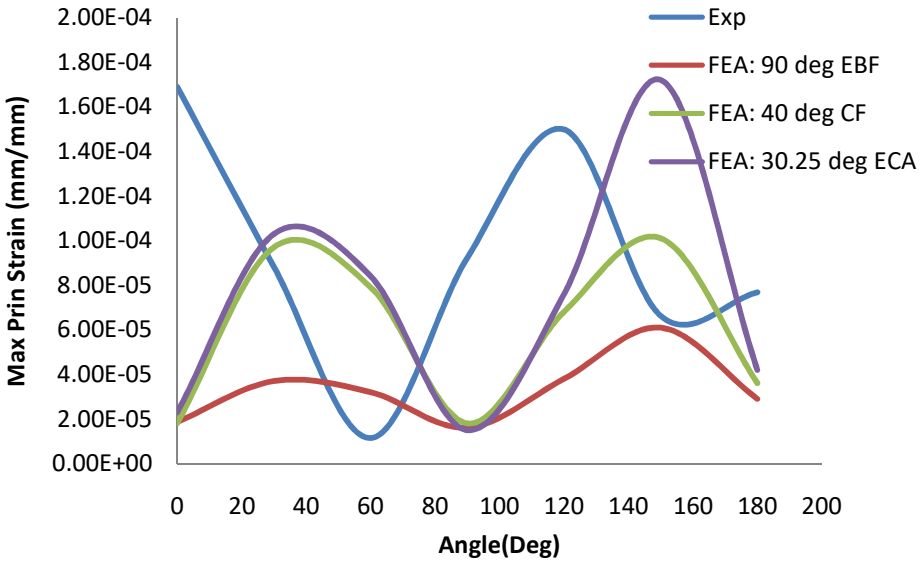

Fig.4.30: Maximum Principal Strain Results at Outboard Bead Seat: Experimental versus FEA at 4750 N Radial Load and 0.15 MPa Inflation Pressure.

Figures 4.31 - 4.32 represent plots of the maximum principal strain at the wheel's outboard bead seating surface at different inflation pressure of 0.3 MPa and 0.15 MPa respectively at 3570 N radial load.

From Figure 4.31, at 0.3 MPa inflation pressure and 3570 N radial load. It could be seen that at 0 degree contact angle, the experimental maximum principal strain value was about 1.11 x 10^{-4} mm/mm, while those of 90 degree EBF, 40 degree CF and ECAwer about 0.05 x 10^{-4}, 0.11 x 10^{-4} and 0.13 x 10^{-4} mm/mm respectively. Their corresponding mean maximum principal strain values, in the same order, were about 0.49 x 10^{-4}, 0.23 x 10^{-4},0.55 x 10^{-4} and .59 x 10^{-4} mm/mm, respectively. The largest experimental maximum principal strain value of about 1.11 x 10^{-4} mm/mm and occurred at about 0 degree location at the outboard bead seat. The highest FE values for 90 degree EBF, 40 degree CF and ECAwere 0.45 x 10^{-4}, 0.90 x 10^{-4} and, 1.03 x 10^{-4} mm/mm, respectively at 30 degree location.The curves assume the same characteristics as those of Figure 4.15

From Figure 4.32 at 0.15 MPa inflation pressure and 3570 N radial load. It could be seen that at 0 degree angular location, the experimental maximum principal strain value wasabout 1.07 x 10^{-4} mm/mm, while those of 90 degree EBF, 40 degree CF and ECAwere about 0.04 x 10^{-4}, 0.12 x 10^{-4}, and 0.12 x 10^{-4} mm/mm, respectively. Their corresponding mean maximum principal strain values were about 0.48 x 10^{-4}, 0.16 x 10^{-4}, 0.31 x 10^{-4} and 0.32 x 10^{-4} mm/mm, respectively. The highest experimental maximum principal strain value was about 1.07 x 10^{-4} mm/mm and occurred at circumferential angle location of 0 degree, while, the greatest FE values of 90 degree EBF, 40 degree CF and ECAwere about 0.29 x 10^{-4},0.55 x 10^{-4}0.61 x 10^{-4} mm/mm, respectively. at 150 circumferential angle. The curves assume the trend in Figure 4.31.

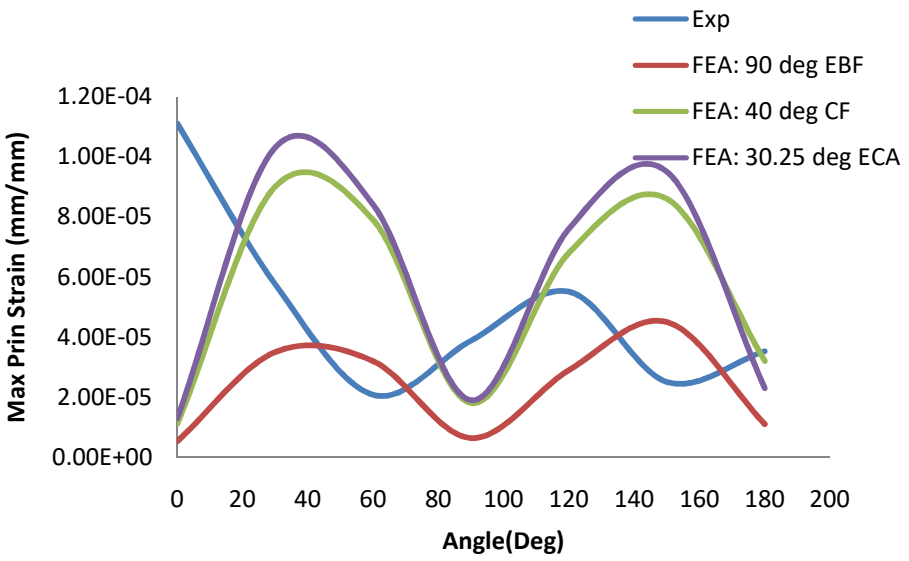

Fig. 4.31: Maximum Principal Strain Results at the Outboard Bead Seat: Experimental versusFEA at 3570 N Radial Load and 0.3 MPa Inflation Pressure.

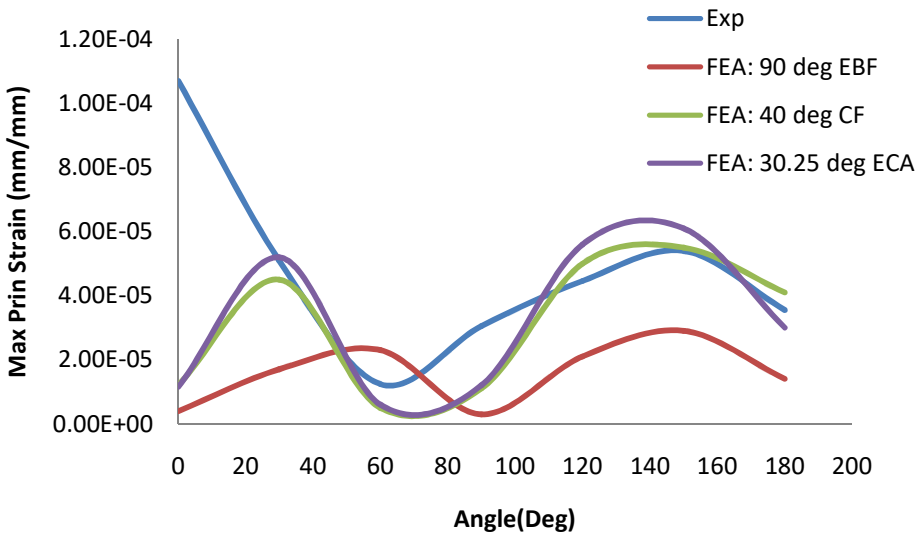

Fig. 4.32: Maximum Principal Strain Results at the Outboard Bead Seat: Experimental versusFEA at 3570 N Radial Load and 0.15 MPa Inflation Pressure.

4.4.2 Maximum Principal Stress

Figures 4.33-4.34 show the curves of the maximum principal stresses at different inflation pressure and 3570 N radial loading conditions.

At 0.3 MPa inflation pressure, Figure 4.33, the experimental maximum principal stress value at ground contact was about 6.21 MPa. For the FE loading condition, the values were about, 0.58,0.48 and and 0.48 MPa, respectively for 90 degree EBF, 40 degree CF and ECA. Their corresponding mean values were about 3.44,0.33, 1.01 MPa and 1.03 MPa respectively. The experimental values were all higher than those of the FE within the range of 0 and 180 degree locations.

At 0.15 MPa inflation pressure, Figure 4.34, the experimental maximum principal stress values were higher than the 90 degree EBF, 40 dgree CF and ECA values, with their corresponding ground contact angle values of about 4.31, 0.24, 0.10 and 0.10 MPa, respectively. Their matching mean maximum principal strain values were about 2.92,0.45, 0.85 and 1.18 MPa, respectively. Their highest values were about 4.31, 1.10, 1.52 and 1.81, respectively for the experimental, 90 deg EBF, 40 deg CF and ECA. All experimental values were higher than FE values.

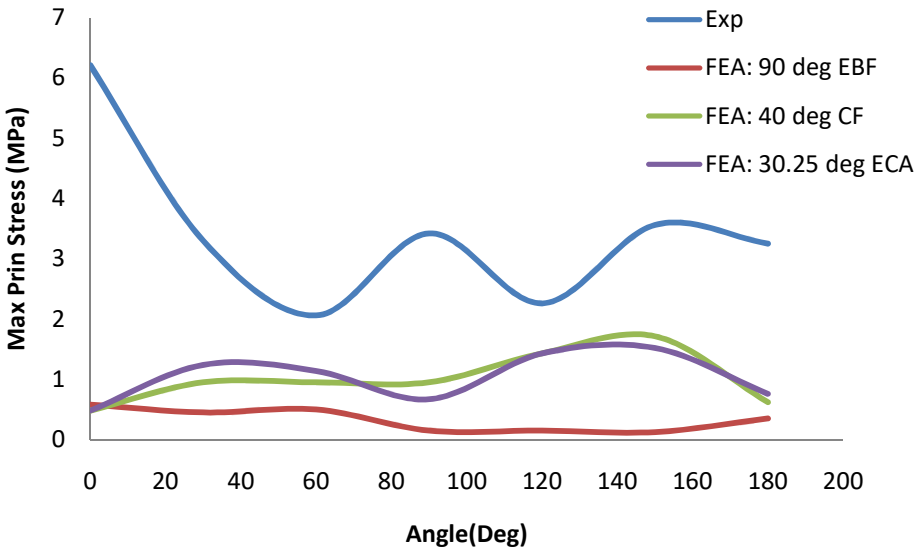

Fig.4.33: Maximum Principal Stress Results at Outboard Bead Seat: Experimental versusFEA at 4750 N Radial Load and 0.3 MPa Inflation Pressure.

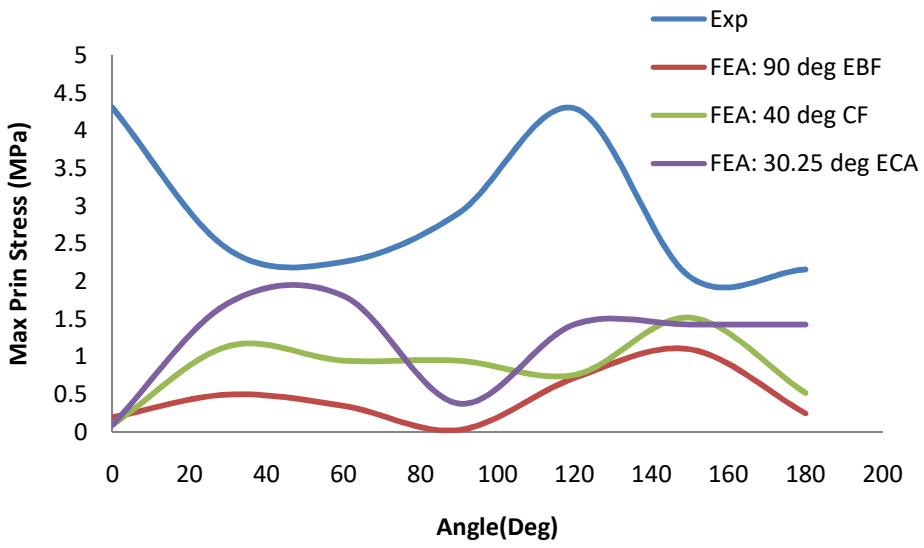

Fig.4.34: Maximum Principal Stress Results at Outboard Bead Seat: Experimental versusFEA at 4750 N Radial Load and 0.15 MPa Inflation Pressure.

Figures 4.35 - 4.36 show the curves of the maximum principal stresses at different inflation pressure and 3570 N radial loading conditions

Figure 4.35, at 0.3 MPa inflation pressure and 3570 N radial load, the experimental ground contact maximum principal stress value was about 3.61 MPa, while those of the FE - 90 degree EBF, 40 degree CF and ECA - are about 0.05, 0.11and 0.10 MPa respectively. Their corresponding mean maximum principal stress values were about 2.44,0.54, 0.53 and 1.04 MPa, respectively, with the least being the 90 degree EBF. Their greatest maximum principal stress values are about 3.61, 1.50,0.09 and 1.81 MPa, respectively.

From Figure 4.36 and at inflation pressure of 0,15 MPa at 3570 N radial load, the highest maximum principal stress values were about 3.25 MPa for the experimental condition; 1.31 MPa for 90 degree EBF; 1.17 MPa for 40 degree CF and 1.37 MPa for ECA, respectively. Their corresponding mean maximum principal stress values were about 1.65, 0.55, 0.50 and 0.67 MPa, respectively, with the least being the 40 degree EBF. The characteristics of the curves are same with those in Figure 4,31 between 0 and 30 degree locations, with the experimental values dominating.

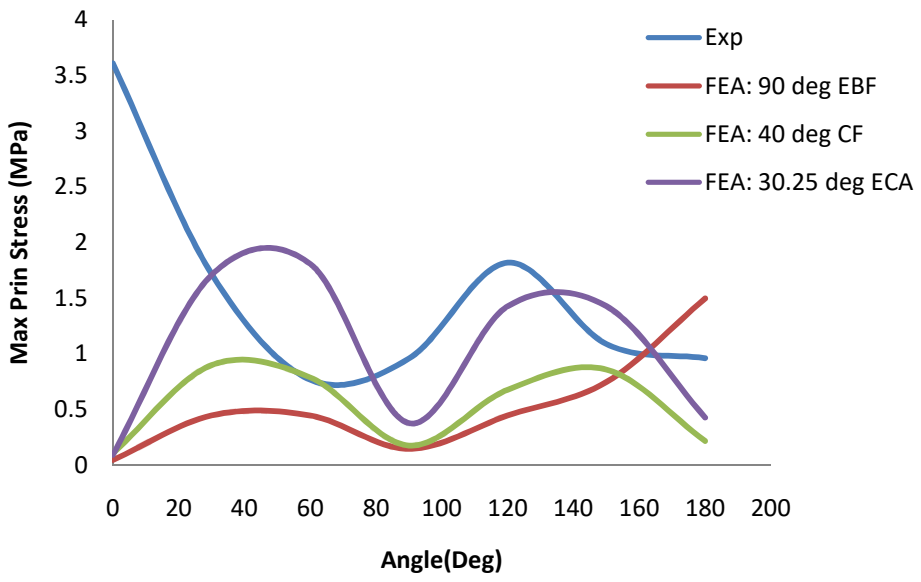

Fig. 4.35: Maximum Principal Stress Results at the Outboard Bead Seat: Experimental versusFEA at 3570 N Radial Load and 0.3 MPa Inflation Pressure.

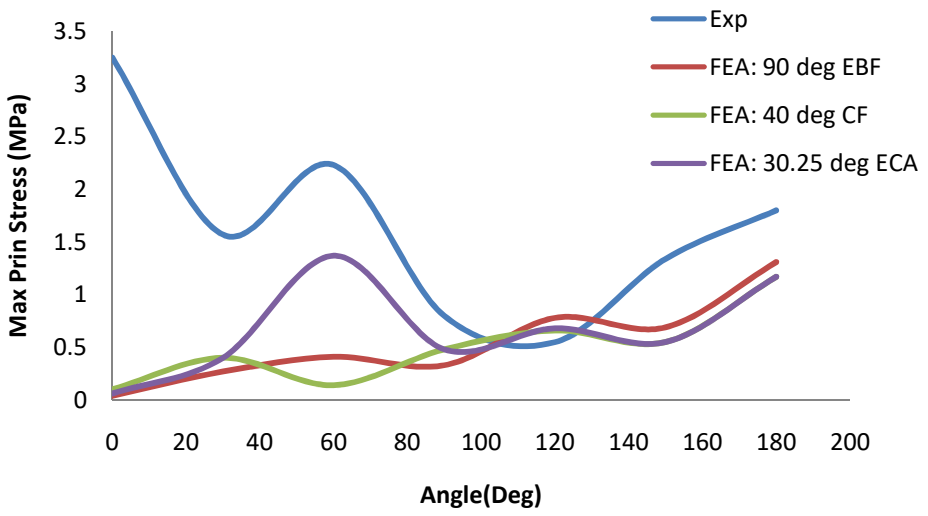

Fig. 4.36: Maximum Principal Stress Results at Outboard Bead Seat: Experimental versusFEA at 3570 N Radial Load and 0.15 MPa Inflation Pressure.

4.4.3 Von-Mises Stress

Figures 4.37 - 4.38 show plots of the Von-Mises stresses of the experimental and FE loading conditions at different inflation pressure of 0.3 and 0.15 MPa respectively, at 4750 N radial load.

At 0.3 MPa, Figure 4.37, it was observed that the respective ground contact Von-Mises stress values were respectively, about 8.78, 1.05, 1.26 and 1.43 MPa for experimental, 90 degree EBF, 40 degree CF andECA. Their corresponding mean mean Von-Mises stresses were about 4.86, 1.44, 2.04 and 2.50 MPa, respectively. The experimental Von-Mises stress values were higher than the FE values within the range of 0 degree and 180 degree location. Between 0 and 30 degree locations, the experimental curve reduced in value with a constant slope and decreases with about the same slope to about 2.88 MPa at 90 degree angular location. The FE curves increased gradually from 0 to 30 degree location and decreased gradually between 30 and 60 degree locations to a value of about 1.04 MPa. It was observed that the experimental values were higher than the FE values for all values between the 0 and 25 degree and between 60 and 180 degree locations

From Figure 4.38, at 0.15 MPa inflation pressure, it could be seen that the Von-Mises stress values at 0 degree contact angle, were about, 6.09, 0.44, 0.70 and 0.65 MPa, respectively for the experimental, 90 degree EBF, 40 degree CF and ECA; with a corresponding mean Von-Mises values of about 3.56,0.93, 1.60 and 1.50 MPa, respectively. The curves assume the same character as those of Figure 4.37.

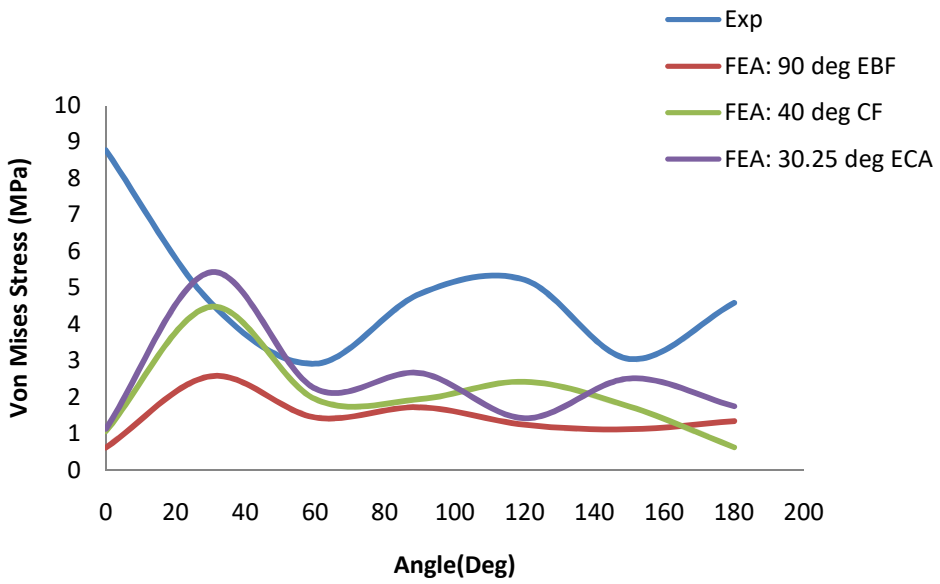

Fig.4.37: Von Mises Stress Results at the Outboard Bead Seat: Experimental versusFEA at 4750 N Radial Load and 0.3 MPa Inflation Pressure.

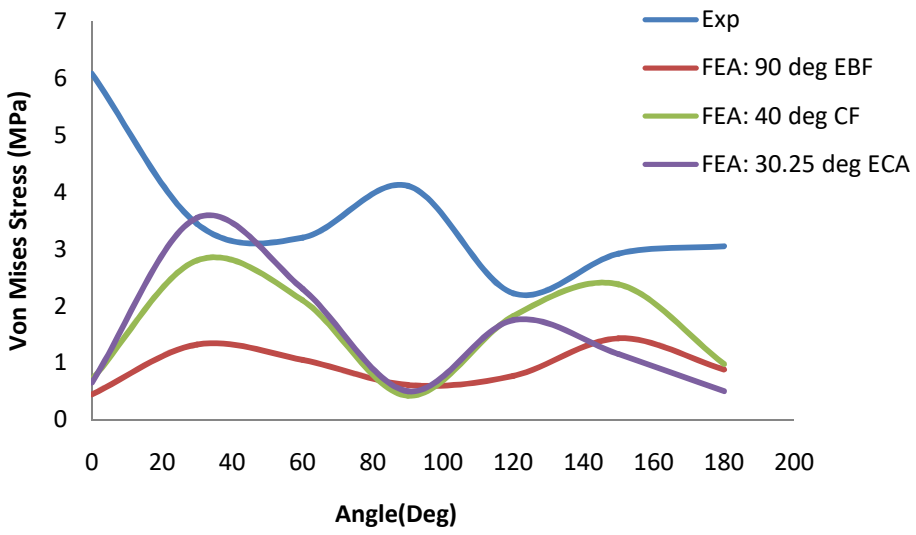

Fig.4.38: Von Mises Stress Results at the Outboard Bead Seat: Experimental versusFEA at 4750 N Radial Load and 0.15 MPa Inflation Pressure.

Figures 4.39 - 4.40 show plots of the Von-Mises stresses of the experimental and FE loading conditions at different inflation pressure of 0.3 MP and 0.15 MPa respectively, at 3570 N radial load.

Figure 4.39 represent the curves at 0.3 MPa inflation pressure, at the outboard bead seat, of the Von-Mises stress values for both the empirical and FE values of 90 degree EBF, 40 degree CF and ECA at 3570 N radial load. The results showed that at ground contact, the experimental value of the Von-Mises stress was about 5.11 MPa; for 90 degree EBF, about 0.11 MPa; about 0.28 MPa for 40 degree CF and about 0.26 MPa for ECA. In the same order as the values at ground contact, the mean Von-Mises stresses wer about, 2.15, 0.63, 1.39 and 1.64 MPa, respectively. Their respective maximum Von - Mises stress values were about 5.11, 1.10, 2.66 and 3.12 MPa, respectively for experimental, 90 degree EBF, 40 degree CF andECA.

At 0.15 MPa, Figure 4.40, it was observed that the respective ground contact Von-Mises stress values at the well were: for experimental, about 4.60 MPa; for 90 degree EBF, about 0.05 MPa; about 0.21 MPa for 40 degree CF, whlie for ECA, it is about .19 MPa. Their corresponding mean Von-Mises stresses were about 2.18 MPa, 0.33 MPa, 0.98 MPa and 1.15 MPa respectively. The maximum Von - Mises stress values were: for experimental, about 4.60 MPa; for 90 degree EBF, about 0.69 MPa; about 1.52 MPa for 40 degree CF, whlie for ECA, it is about 1.81 MPa.

An increase in inflation pressure from 0.15 MPa to 0.3MPa increased the mean Von -Mises stress values as follows: about 31% for the experimental; 91% for the 90 degree EBF; 28% for 40 CF and 43% for ECA. Increasing the radial load from 3570 N to 4750 N maximum load, the mean experimental value at 0.3 MPa is increased by about: 126% for experimental; .129% for 90 deg EBF; 467% for 40 deg CF and 40% for ECA.At 0.15 MPa their corresponding increases were about 63% experimental; 90 deg EBF by 182%; 40 deg CF by 63% and ECA by 16% respectively.

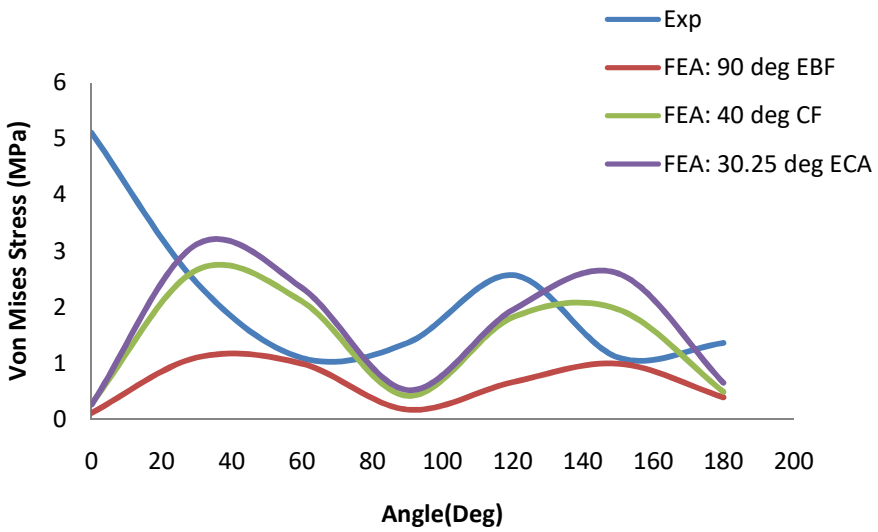

Fig. 4.39: Von Mises Stress Results at the Outboard Bead Seat: Experimental versusFEA at 3570 N Radial Load and 0.3 MPa Inflation Pressure.

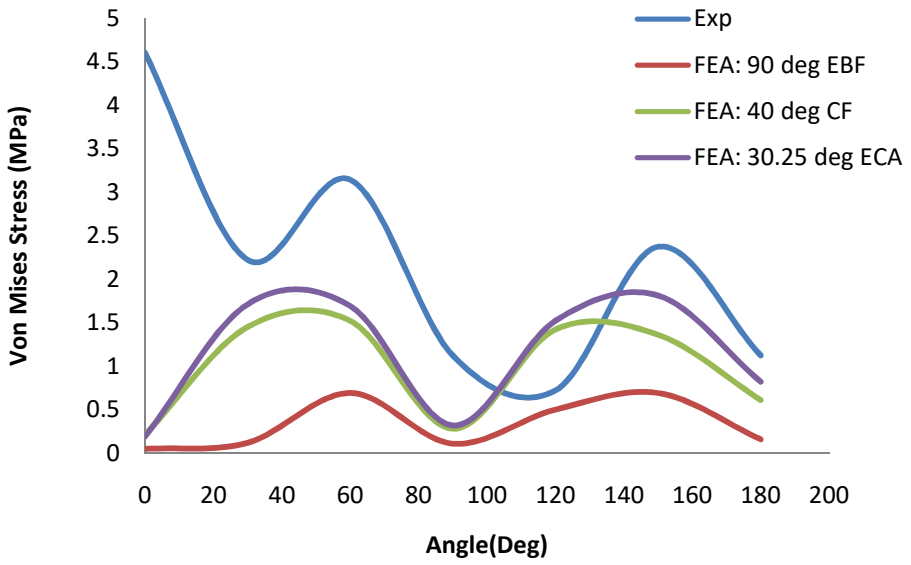

Fig. 4.40: Von Mises Stress Results at the Outboard Bead Seat: Experimental versusFEA at 3570 N Radial Load and 0.15 MPa Inflation Pressure.

4.5 Influenceof Inflation Pressure and Radial Load Variation at Inboard Bead Seat, Well and Outboard Bead Seat

Tables 4.4- 4.6 illustrate the effect of inflation pressure and radial load variation on the mean maximum principal strain at the inboard bead seat, well and outboard bead seat, respectively. It showed that for a 50% increase in inflation pressure (from 0.5 to 0.3 MPa), the mean maximum principal strains were increased by about 51%, 527%, and 20%, respectively at the inboard bead seat, well and outboard bead seat at 4750 N radial load. While at 3570 N radial load, their corresponding increase were 31%, 154% and 58%, respectively. Fora 25% increase in radial load (from 3570 to 4750 N) lead to an increase in maximum principal strain of about 51%, 61% and 105, respectively the inboard bead seat, well and outboard bead seat at inflation pressure of 0.15. Corresponding increase at 0.3 MPa, were 24%, 256% and 150%, respectively.

Table 4.7 - 4.9 showed that for a 50% increase in inflation pressure (from 0.5 to 0.3 MPa) at 4750 N radial load, the mean maximum principal stress was increased by about 19%, 16 % and 22%, respectively at inboard bead seat, well and outboard bead seat, while at 3570 N, their corresponding values were 23%, 32% and 39%, respectively.A 25% increase in radial load (from 3570 to 4750 N) lead to an increase in maximum principal stress of about 61%, 39% and 44%, respectively at inboard bead seat, well and outboard bead seat, respectively at inflation pressure of 0.15. At inflation pressure of 0.3 MPa, the values were up at inboard bead seat, well and outboard bead seat by 73%, 67% and 63% respectively.

Tables 4.10- 4.12 illustrate the effect of inflation pressure and radial load variation on the mean Von- Mises stress at the inboard bead seat, well and outboard bead seat, respectively, It showed that for a 50% increase in inflation pressure (from 0.5 to 0.3 MPa), the mean maximum principal strain was increased by about 68%, 67%, and 52%, respectively at the inboard bead seat, well and outboard bead seat at 4750 N radial load. While at 3570 N radial load, their corresponding increase were 38%, 15% and 44%, respectively, For a 25% increase in radial load (from 3570 to 4750 N) lead to an increase in maximum principal strain of about 255%, 46% and 61%, respectively the inboard bead seat, well and outboard bead seat at inflation pressure of 0.15. Their corresponding increase at 0.3 MPa, were 310%, 126% and 73%, respectively.

Table 4.4: Effect of Inflation Pressure Variation onthe Mean Maximum PrincipalStrain Values at the Inboard Bead Seat

LOAD (N)	Inflation Pressure (MPa)	Experimental ($x10^{-4}$ mm/mm)	90 Degree BF ($x\ 10^{-4}$ mm/mm)	40 Degree CF ($x\ 10^{-4}$ mm/mm)	ECA ($x\ 10^{-4}$ mm/mm)
4750	0.3	1.44	1.00	1.81	2.11
	0.15	0.94	0.62	1.16	1.59
3570	0.3	0.80	0.64	1.16	1.59
	0.15	0.47	0.62	1.13	1.33

Table 4.5: Effect of Inflation Pressure Variation on the Mean Maximum Principal strain Values at the Well

LOAD(N)	Inflation Pressure (MPa)	Experimental ($x10^{-4}$ mm/mm)	90Degree EBF ($x\ 10^{-4}$ mm/mm)	40 Degree CF ($x\ 10^{-4}$ mm/mm)	ECA ($x\ 10^{-4}$ mm/mm)
4750	0.3	1.21	3.73	3.68	3.78
	0.15	1.03	0.29	0.68	0.67
3570	0.3	0.69	1.01	0.98	0.75
	0.15	0.50	0.20	0.37	0.58

Table 4.6: Effect of Inflation Pressure Variation on the Mean Maximum Principal Strain Values at the Outboard Bead Seat

LOAD (N)	Inflation Pressure (MPa)	Experimental ($x10^{-4}$ mm/mm)	90 Degree EBF ($x\ 10^{-4}$ mm/mm)	40 Degree CF ($x\ 10^{-4}$ mm/mm)	ECA ($x\ 10^{-4}$ mm/mm)
4750	0.3	1.00	0.50	0.64	0.84
	0.15	0.39	0.33	0.60	0.72
3570	0.3	0.19	0.23	0.55	0.59
	0.15	0.48	0.16	0.31	0.32

Table 4.7: Effect of Inflation Pressure Variation on the Mean Maximum Principal stress Values at the Inboard Bead Seat

LOAD (N)	Inflation Pressure (MPa)	Experimental (MPa)	90 Degree EBF (MPa)	40 Degree CF (MPa)	ECA (MPa)
4750	0.3	4.52	0.47	1.35	1.09
	0.15	2.89	0.41	1.30	1.11
3570	0.3	1.46	0.39	1.03	0.83
	0.15	1.39	0.26	0.84	0.72

Table 4.8: Effect of Inflation Pressure Variation on the Mean Maximum Principal stress Values at the Well

LOAD (N)	Inflation Pressure (MPa)	Experimental (MPa)	90 Degree EBF (MPa)	40 Degree CF (MPa)	ECA (MPa)
4750	0.3	3.86	8.35	6.67	8.09
	0.15	3.17	4.30	4.23	4.64
3570	0.3	3.01	4.66	3.70	4.33
	0.15	2.40	3.01	3.06	3.29

Table 4.9: Effect of Inflation Pressure Variation on the Mean Maximum Principal stress Values at the Outboard Bead Seat

LOAD (N)	Inflation Pressure (MPa)	Experimental (MPa)	90 Degree EBF (MPa)	40 Degree CF (MPa)	ECA (MPa)
4750	0.3	3.44	0.33	1.01	1.03
	0.15	3.92	0.45	0.85	1.18
3570	0.3	1.56	0.54	0.53	1.04
	0.15	2.65	0.55	0.5	0.67

Table 4.10: Effect of Inflation Pressure Variation on the Mean Von-Mises Stress Values at the Inboard Bead Seat

LOAD (N)	Inflation Pressure (MPa)	Experimental (MPa)	90 Degree EBF (MPa)	40 Degree CF (MPa)	ECA (MPa)
4750	0.3	5.45	5.27	5.66	5.33
	0.15	4.14	2.81	3.59	2.78
3570	0.3	2.33	0.64	1.71	2.19
	0.15	1.96	0.44	1.09	1.56

Table 4.11: Effect of Inflation Pressure Variation on the Mean Von-Mises Stress Values at the Well

LOAD (N)	Inflation Pressure (MPa)	Experimental (MPa)	90 Degree EBF (MPa)	40 Degree CF (MPa)	ECA (MPa)
4750	0.3	6.29	8.52	7.75	6.75
	0.15	4.47	4.23	4.23	4.68
3570	0.3	3.57	3.08	3.14	3.32
	0.15	2.63	3.58	3.00	3.13

Table 4.12: Effect of Inflation Pressure Variation on the Mean Von-Mises Stress Values at the Outboard Bead Seat

LOAD (N)	Inflation Pressure (MPa)	Experimental (MPa)	90 Degree EBF (MPa)	40 Degree CF (MPa)	ECA (MPa)
4750	0.3	4.86	1.44	2.04	2.50
	0.15	3.56	0.93	1.60	1.50
3570	0.3	2.15	0.63	1.39	1.64
	0.15	2.18	0.33	0.98	1.15

Tables 4.13 - 4.15 show the locations of highest induced maximum principal strain values at different inflation pressures of 0.15 and 0.3 MPa and radial loads of 4750 N and 3570 N. Table 4.13, 4.14 and 4.15 represent values at inboard bead seat, well and outboard bead seat, respectively. From the tables, it was observed that the highest maximum principal strain did not act on any specific angular location for all loading conditions. However, in view of the fact that highest maximum principal strain occur mostly at 0 degree location at inboard beat seat and well, it could be safe to assume that highest maximum principal strain values act at the inboard bead seat and well at the point of contact of the wheel with the ground, while that at the outboard lie between 0 and 150 degree location. This could probably be due to the orientation and location of the wheel's arm at the outboard bead seat.

Tables 4.16 - 4.18 represent the locations of highest induced maximum principal stresses at the same loading conditions as those of Tables 4.13 - 4.15. Inboard bead seat, well and outboard bead seat are depicted by Tables 4.16, 4.17 and 4.18, respectively. Again, there was no exact angular location where the highest maximum principal stress act for all loading conditions. However, since the highest maximum principal stress occur mostly at 0 degree location at inboard beat seat and well, it could be said that highest maximum principal stress values act at the inboard bead seat and well at the point of contact of the wheel with the ground, while that at the outboard lie between 0 and 180 degree location. This was due to the reason ascribed to Tables 4.13 - 4.15.

Tables 4.19 - 4.21 represent the locations of highest induced Von-Mises stresses at the same loading conditions as those of Tables 4.11 - 4.13. Inboard bead seat, well and outboard bead seat are depicted by Tables 4.19, 4.20 and 4.21, respectively. It was observed that the highest Von-Mises stress for all loading conditions occur mostly at 0 degree location at inboard beat seat and well, hence, highest Von-Mises stress values could be said to act at the inboard bead seat and well at the point of contact of the wheel with the ground, while that at the outboard lie between 0 and 180 degree location. This was also due to the reason ascribed to Tables 4.11 - 4.13.

Table 4.13: Effect of Inflation Pressure Variation on the HighestInduced Maximum Principal Strain Values at the Inboard Bead Seat

LOAD (N)	Inflation Pressure (MPa)		Experimental (x 10^{-4} mm/mm)	90 Degree EBF (x 10^{-4} mm/mm)	40 Degree CF (x 10^{-4} mm/mm)	ECA (x 10^{-4} mm/mm)
4750	0.3	Value	2.12	1.52	4.51	5.69
		Location (deg)	150	60	0	0
	0.15	Value	1.76	1.29	2.53	5.26
		Location (deg)	0	0	0	0
3570	0.3	Value	1.36	0.95	2.53	5.26
		Location (deg)	0	60	0	0
	0.15	Value	.68	1.99	2.95	3.73
		Location (deg)	60	0	0	0

Table 4.14: Effect of Inflation Pressure Variation on the Highest Maximum Principal Strain Values at the Well

LOAD (N)	Inflation Pressure (MPa)		Experimental ($x10^{-4}$ mm/mm)	90 Degree EBF ($x10^{-4}$ mm/mm)	40 Degree CF ($x\ 10^{-4}$ mm/mm)	ECA ($x\ 10^{-4}$ mm/mm)
4750	0.3	Value	2.11	4.38	5.07	5.66
		Location (deg)	90	0	0	0
	0.15	Value	1.47	0.60	1.56	2.00
		Location (deg)	120	0	0	0
3570	0.3	Value	1.49	1.69	2.29	1.67
		Location (deg)	60	0	0	0
	0.15	Value	0.73	0.47	1.20	1.62
		Location (deg)	150	0	0	0

Table 4.15: Effect of Inflation Pressure Variation on the Highest Maximum Principal Strain Values at the Outboard Bead Seat

LOAD (N)	Inflation Pressure (MPa)		Experimental (x 10^{-4} mm/mm)	90 Degree EBF (x 10^{-4} mm/mm)	40 Degree CF (x 10^{-4} mm/mm)	ECA (x 10^{-4} mm/mm)
4750	0.3	Value	2.22	0.83	0.99	1.56
		Location (deg)	0	150	120	150
	0.15	Value	1.69	0.61	1.01	1.72
		Location (deg)	0	150	150	150
3570	0.3	Value	1.11	.45	0.90	1.03
		Location (deg)	0	30	30	30
	0.15	Value	1.24	0.29	0.55	.61
		Location (deg)	0	150	150	150

Table 4.16: Effect of Inflation Pressure Variation on the Highest Maximum Principal Stress Values at the Inboard Bead Seat

LOAD (N)	Inflation Pressure (MPa)		Experimental (MPa)	90 Degree EBF (MPa)	40 Degree CF (MPa)	ECA (MPa)
4750	0.3	Value	7.20	1.36	5.04	6.30
		Location (deg)	150	60	0	0
	0.15	Value	5.07	1.04	5.04	6.30
		Location (deg)	0	90	0	0
3570	0.3	Value	3.25	1.27	3.93	4.78
		Location (deg)	0	60	0	0
	0.15	Value	2.02	0.60	2.77	4.10
		Location (deg)	90	60	0	0

Table 4.17: Effect of Inflation Pressure Variation on the Highest Maximum Principal Stress Values at the Well

LOAD (N)	Inflation Pressure (MPa)		Experimental (MPa)	90 Degree EBF (MPa)	40 Degree CF (MPa)	ECA (MPa)
4750	0.3	Value	4.49	9.98	12.40	14.28
		Location (deg)	90	0	0	0
	0.15	Value	5.17	5.94	8.37	10.54
		Location (deg)	120	0	0	0
3570	0.3	Value	7.71	11.02	10.01	11.72
		Location (deg)	120	120	120	120
	0.15	Value	5.50	5.45	7.68	9.67
		Location (deg)	120	0	0	0

Table 4.18: Effect of Inflation Pressure Variation on the Highest Maximum Principal Stress Values at the Outboard Bead Seat

LOAD (N)	Inflation Pressure (MPa)		Experimental (MPa)	90 Degree EBF (MPa)	40 Degree CF (MPa)	ECA (MPa)
4750	0.3	Value	6.21	0.58	1.71	1.52
		Location (deg)	0	0	150	150
	0.15	Value	4.31	1.10	1.52	1.81
		Location (deg)	0	150	150	150
3570	0.3	Value	3.61	1.5	0.90	1.81
		Location (deg)	0	90	30	60
	0.15	Value	3.25	1.31	1.17	1.37
		Location (deg)	0	180	180	60

Table 4.19: Effect of Inflation Pressure Variation on the Highest Von-Mises Stress Values at the Inboard Bead Seat

LOAD (N)	Inflation Pressure (MPa)		Experimental (MPa)	90 Degree EBF (MPa)	40 Degree CF (MPa)	ECA (MPa)
4750	0.3	Value	8.60	5.92	11.12	13.11
		Location (deg)	0	0	0	0
	0.15	Value	7.18	3.68	8.06	110.50
		Location (deg)	180	0	0	0
3570	0.3	Value	5.63	1,52	7.44	7.27
		Location (deg)	0	0	0	0
	0.15	Value	2.86	1.23	5.36	5.02
		Location (deg)	60	0	0	0

Table 4.20: Effect of Inflation Pressure Variation on the Highest Von-Mises Stress Values at the Well

LOAD (N)	Inflation Pressure (MPa)		Experimental (MPa)	90 Degree EBF (MPa)	40 Degree CF (MPa)	ECA (MPa)
4750	0.3	Value	9.19	9.45	12.40	12.90
		Location (deg)	90	0	0	0
	0.15	Value	7.32	5.40	8.37	9.00
		Location (deg)	120	0	0	0
3570	0.3	Value	6.33	4.98	7.72	8.29
		Location (deg)	120	0	0	0
	0.15	Value	5.08	6.78	5.77	6.13
		Location (deg)	60	60	60	60

Table 4.21: Effect of Inflation Pressure Variation on the Highest Von-Mises Stress Values at the Outboard Bead Seat

LOAD (N)	Inflation Pressure (MPa)		Experimental (MPa)	90 Degree EBF (MPa)	40 Degree CF (MPa)	ECA (MPa)
4750	0.3	Value	8.78	2.58	4.48	5.43
		Location (deg)	30	30	30	30
	0.15	Value	6.09	1.43	2.80	3.25
		Location (deg)	0	150	30	30
3570	0.3	Value	5.11	1.10	2.66	3.12
		Location (deg)	0	30	30	30
	.15	Value	4.6O	.69	1.52	1.81
		Location (deg)	0	60	60	150

4.6 Effect of Inflation Pressure and Radial Load on Displacementof the FE Wheel Model

The wheel undergoes both stress and deformation (displacement) when loaded. The stress could be determined from experimentally measured strain, but the displacement of the wheel could not be experimentally determined. Therefore, only the FE model of the wheel was analysed at different inflation pressures and radial loads fpr 90 degree EBF, 40 degree CF and experimental contact angle of 30.2 degree (ECA).

Figures 4.41 - 4.46 show the displacement of the rim at the inboard bead seat at 0.3 and 0.15 MPa inflation pressure at radial loads of 4750 and 3570 N, respectively for 90 degree EBF.

Figure 4.41 shows the influence of inflation pressure at 4750 N radial load at inflation pressures of 0.15 and 0.3 MPa. The maximum vertical displacement occurred at 0 degree location for both 0.15 and 0.3 MPa inflation pressure, with values at 0.3 MPa dominating between 0 and 40 degree locations. Higher values were also observed at 0.3 MPa at locations between 140 and 180. Between 40 and 140 degree locations, displacement values at 0.15 MPa inflation pressure dominated. The dominance at 0.15 MPa inflation pressure may probably be due to the fact that the wheel tends to ovalise at lower value of inflation pressure resulting into larger impact of the radial load which lead to higher bending moment and, the tendency of the angular displacement of the arms within this region. The displacement at 40 degree location at both 0.15 and 0.3 MPa was the same because of the presence of an arm about this location and tends to resist further displacement of the wheel at this location. Figures 4.42 - 4.46 possessed the same displacement attributes as that of Figure 4.37.

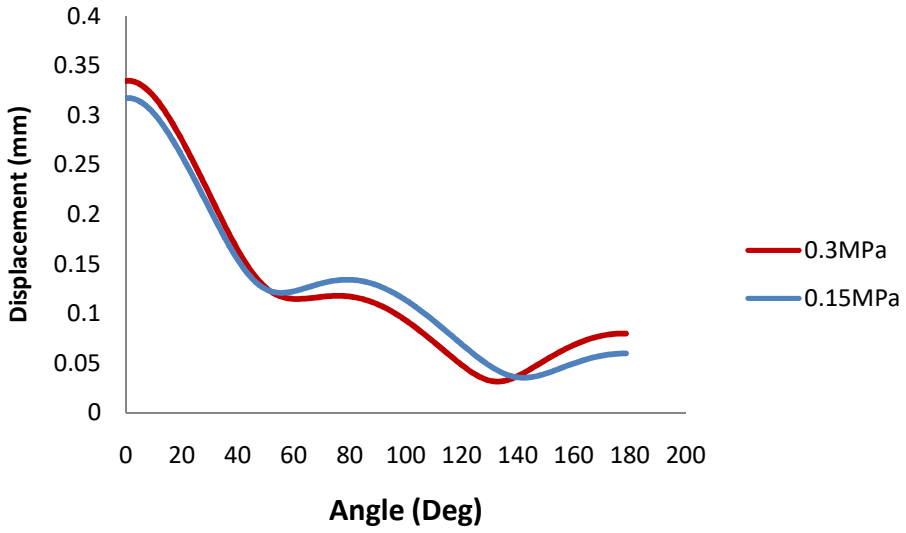

Fig.4.41: Influence of inflation pressure at the inboard bead seat at 4750 N radial load (90 Degree EBF): Displacement

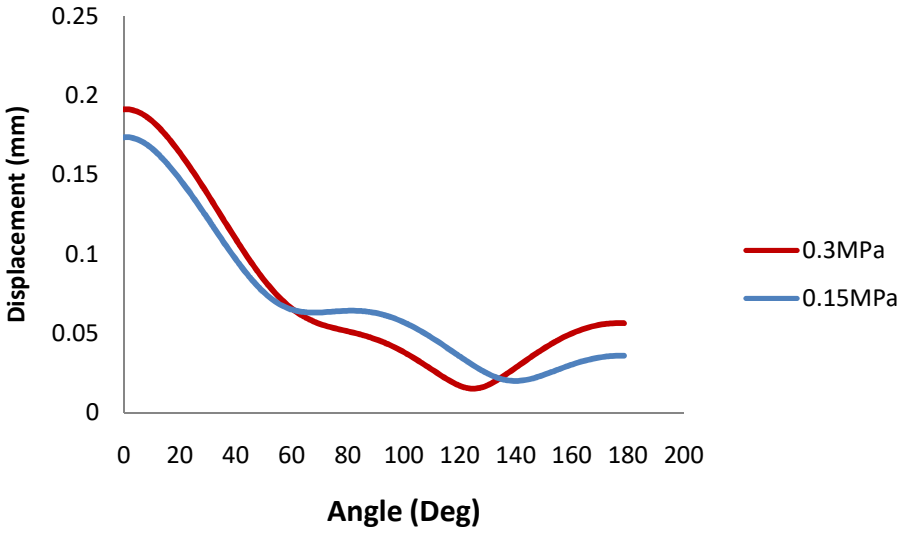

Fig.4.42.: Influence of inflation pressure at the inboard bead seat at 3570 N radial load (90 Degree EBF): Displacement

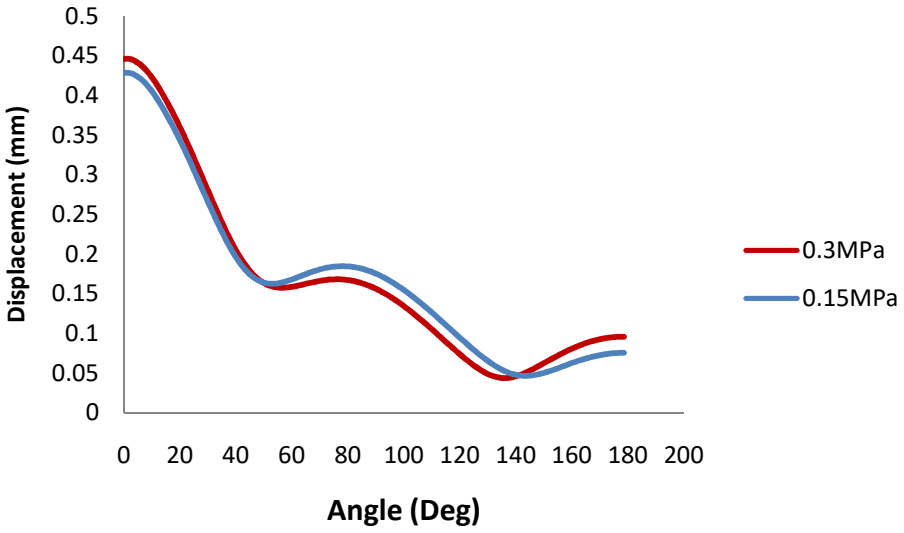

Fig.4.43: Influence of inflation pressure at the inboard bead seat 4750 N radial load (40 Degree CF): displacement

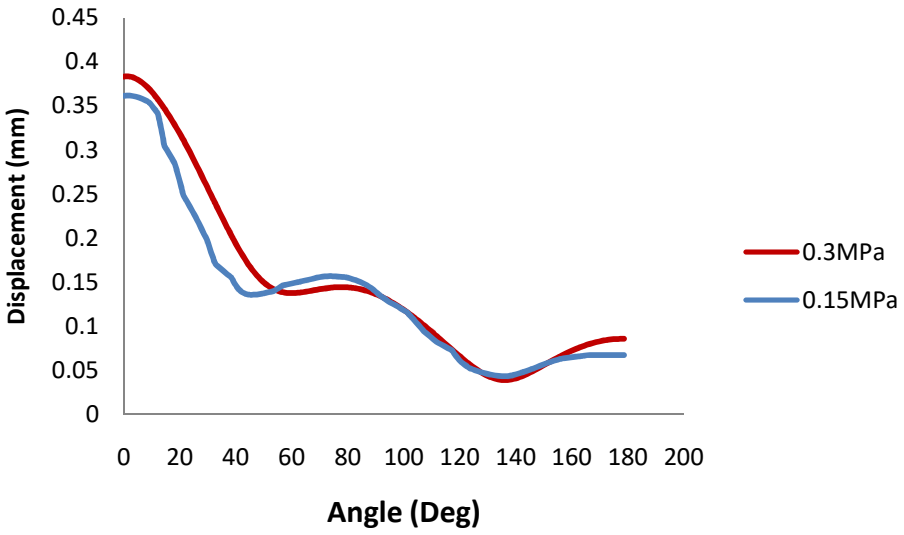

Fig.4.44: Influence of inflation pressure at the inboard bead seat at 3570 N radial load (40 Degree CF): Displacement

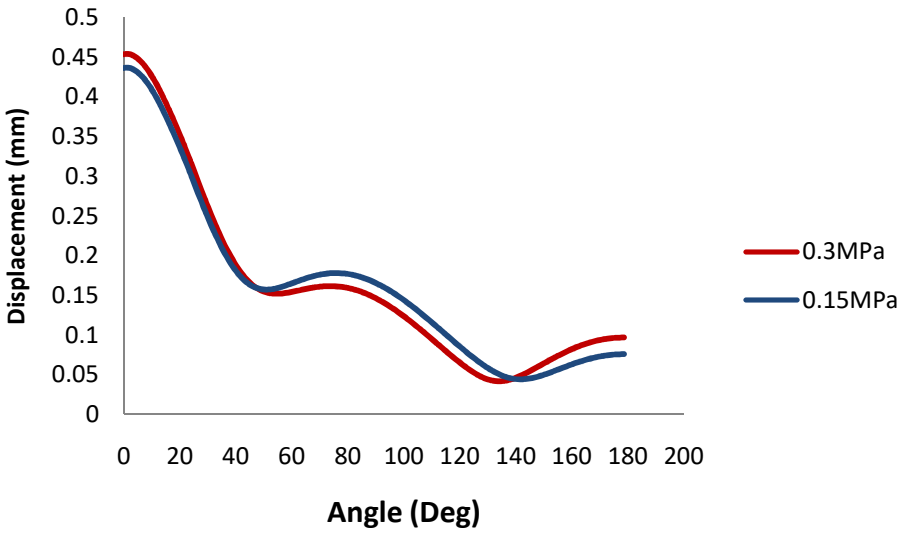

Fig.4.45: Influence of inflation pressure at the inboard bead seat at 4750 N radial load (30.25 degree ECA): displacement

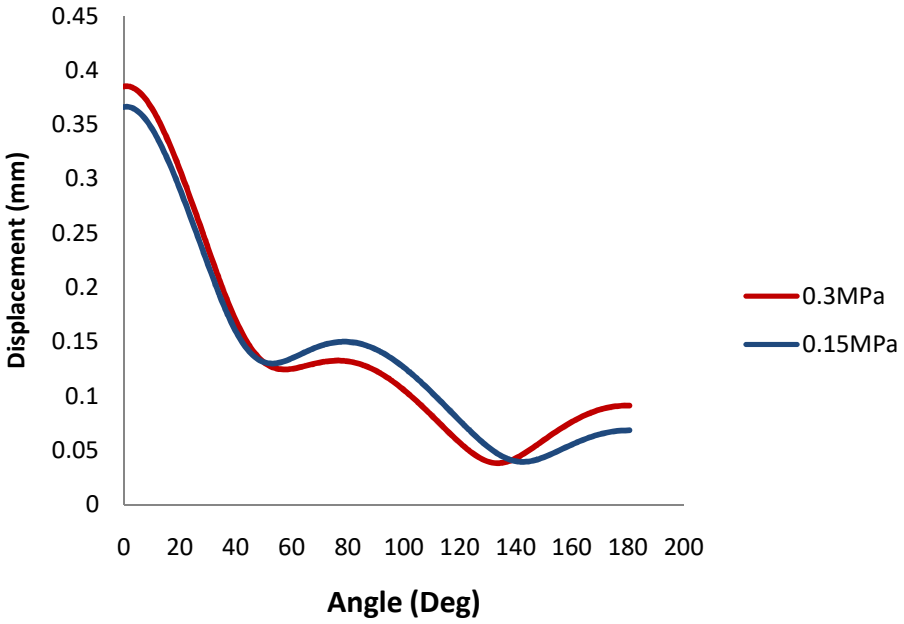

Fig.4.46 : Influence of inflation pressure at the inboard bead seat at 3570 N radial load (30.25 degree ECA): displacement

4.7. Comparison of different loading functions

Figures 4.47 to 4.50 show the comparison of different loading functions at different radial loads and inflation pressures. It was observed that the largest value of displacement was at ECA, followed by 40 degree CF and then by 90 degree EBF.The maximum displacement values at 4750 N radial loadat 0.3 and 0.15 MPa inflation preesure were about 0.46 and 0.44 mm; 0.45 and 0.43 mm; and 0.33 and 0.32 mm, respectivelyfor ECA, 40 degree CF and 90 degree. The corresponding values at 3570 N radial load were 0.39 and 0.37 mm; 0.38 and 0.36 mm; and 0.19 and 0.17 mm, respectively. There was a strong correlation between the 40 degree CF and the ECA. The largest value observed for the ECA was due to the fact that it has the smallest loaddistribution angle compared with the 40 degree CF and 90 degree EBF.

4.8. Comparison of FE Displacement Values at the Inboard Bead Seat, well and Outboard Bead Seat

Figures 4.51 to 4.54 represent the plots of displacement values against angular location.Figure 4.51 show the plots for FE values of 90 deg CF, at 4750 N and at inflation pressures of 0.3 MPa, at the inboard bead seat, well and outboard bead seat. It was observed that the inboard bead seat was more deformed, followed by the well and, then the outboard bead seat. The maximum displacement occurred at 0 degree location. This was due to the relative axial distance of the inboard bead seat and well from the location of the wheel's arms compared to the outboard bead seat and, the off-set of the wheel.Figures 4.52 to 4.54 assumed the same character as that of Figure 4.51.

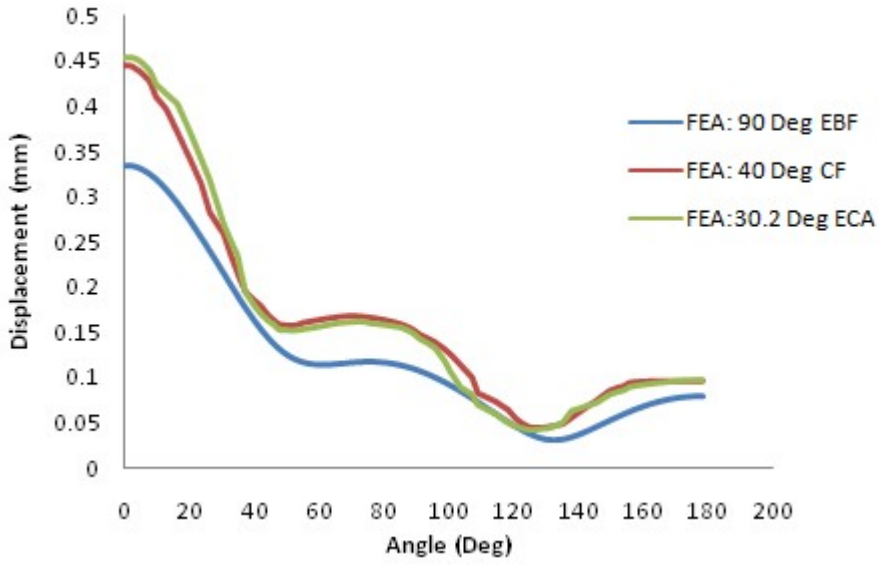

Fig. 4.47: Comparison of different loading functions at the inboard bead seat at 0.3 MPa inflation pressure and 4750 N radial load

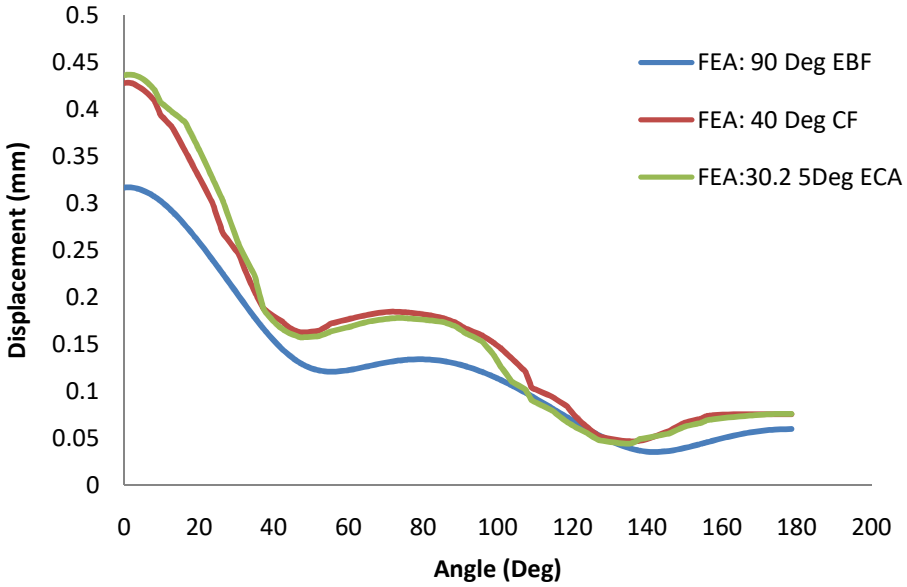

Fig. 4.48: Comparison of different loading functions at the inboard bead seat at 0.15 MPa inflation pressure and 4750 N radial load

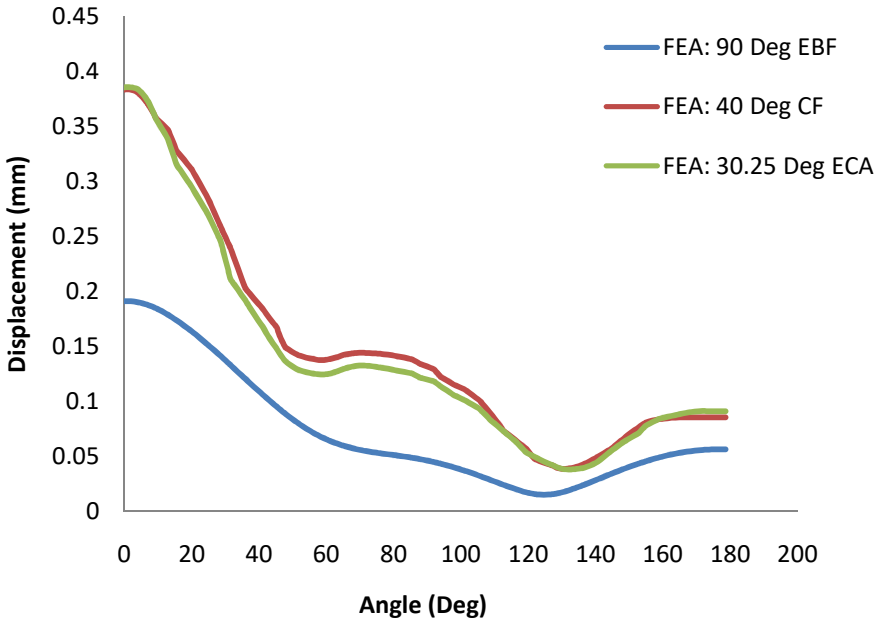

Fig. 4.49: Comparison of different loading functions at the inboard bead seat at 0.3 MPa inflation pressure and 3570 N radial load

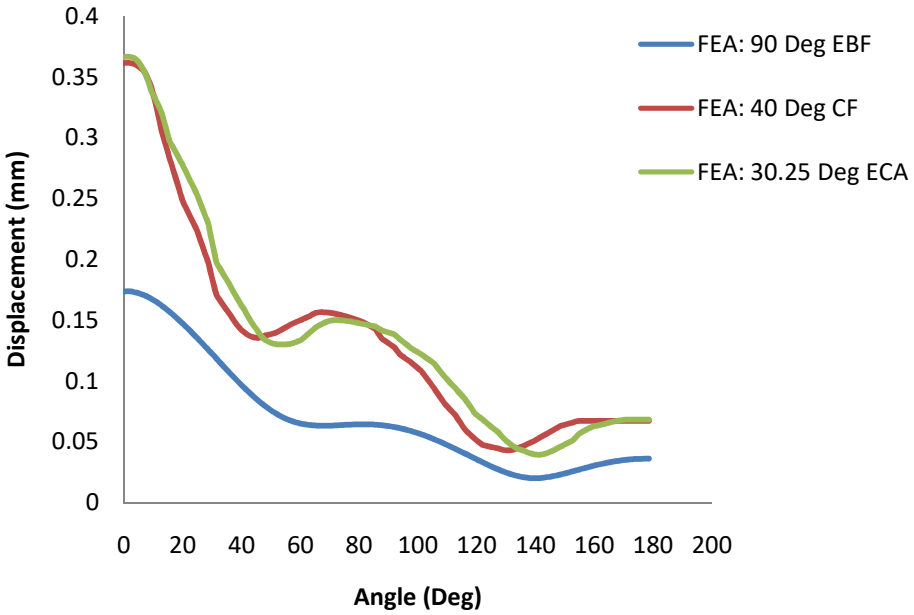

Fig. 4.50: Comparison of different loading functions at the inboard bead seat at 0.15 MPa inflation pressure and 3570 N radial load

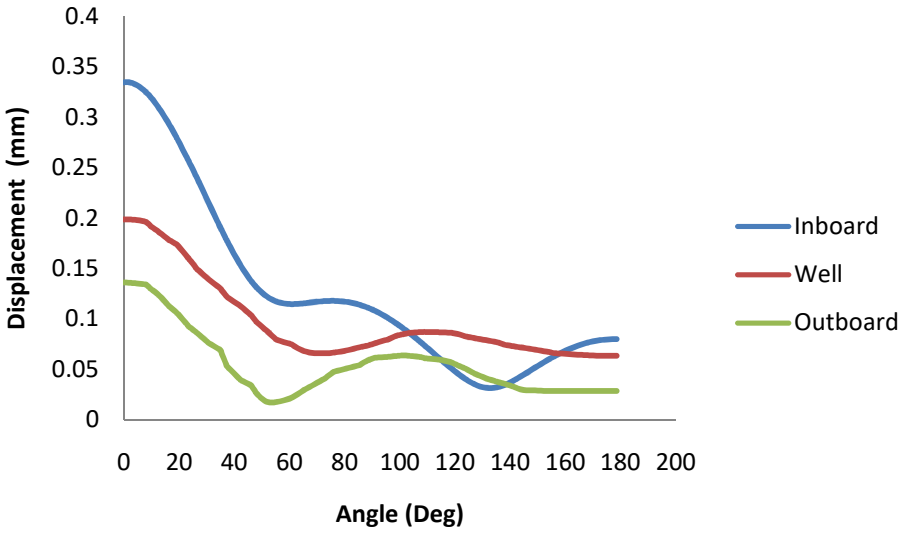

Fig. 4.51: Displacement at different locations of the rim at 0.3 MPa inflation pressure and 4750 N radial load (90 Degree EBF)

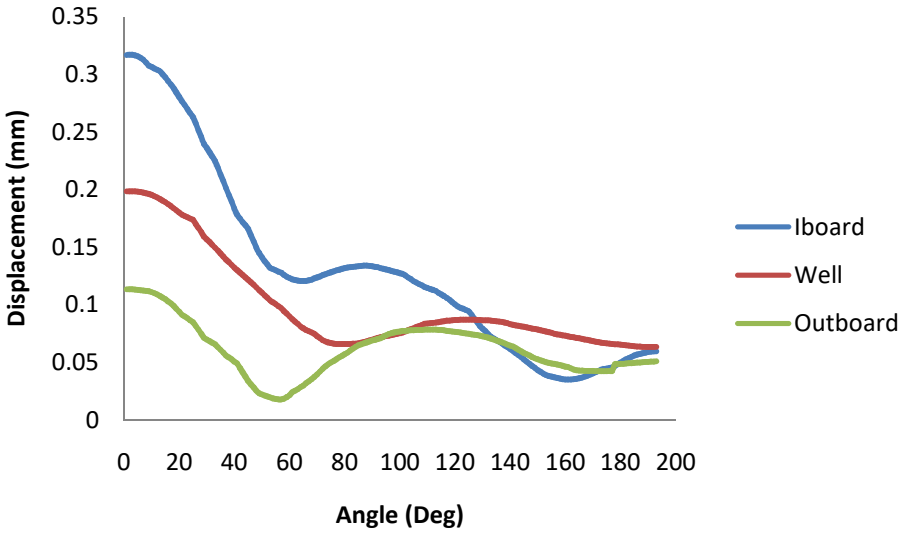

Fig. 4.52: Displacement at different locations of the rim at 0.15 MPa inflation pressure and 4750 N radial load (90 Degree EBF)

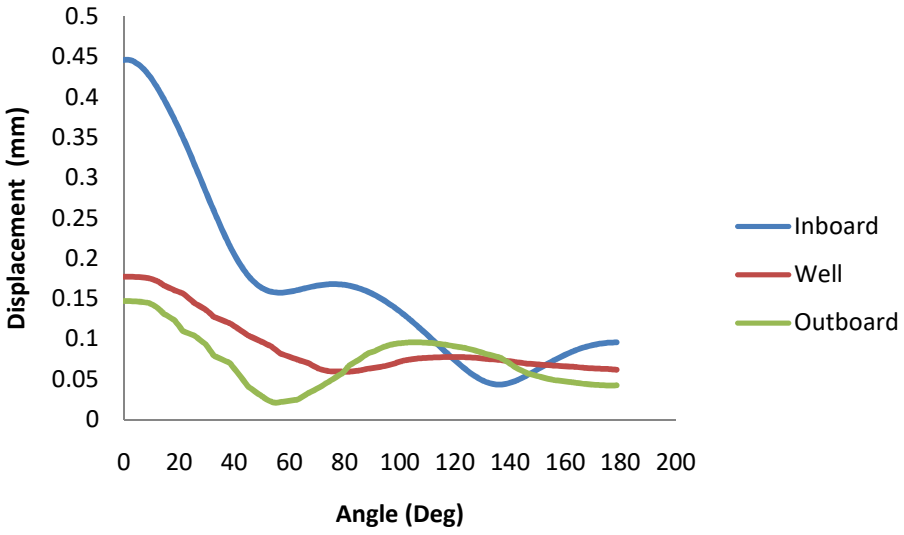

Fig. 4.53: Displacement at different locations of the rim at 0.3 MPa inflation pressure and 4750 N radial load (40 Degree CF)

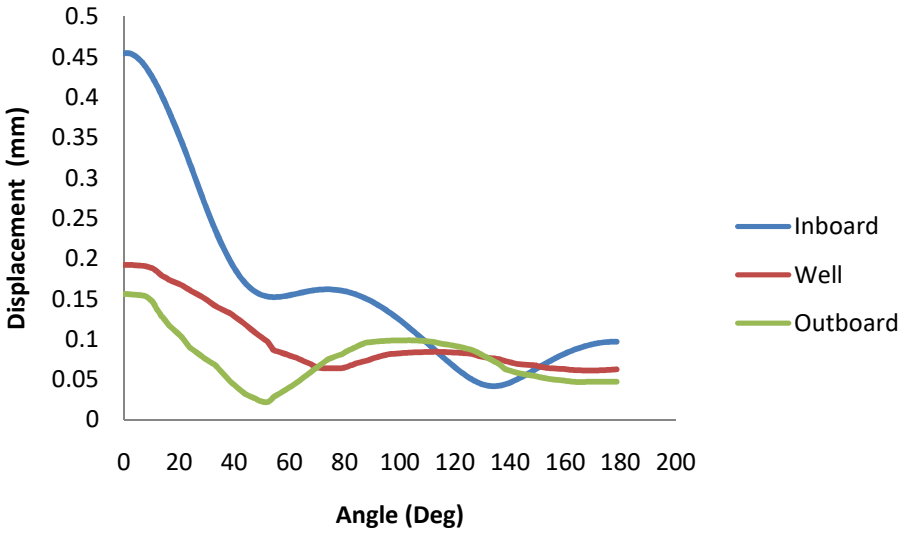

Fig. 4.54: Displacement at different locations of the rim at 0.3 MPa inflation pressure and 4750 N radial load (30.25 degree ECA)

4.9 Comparison of displacement curves

Figure 4.55 shows the relation between the shape the displacement curve obtained by Stearns (2003) and sample graph from this work. The results showed that maximum displacement values occur at the wheel's point of contact with the ground. The results were in good agree as revealed by the shapes of the curves and that of Figures 4.47 - 4.54.

4.10 Comparison of Von - Mises stress

Figure 4.56 (a) & (b) shows the relation between the shape of the Von - Mises stress curve obtained by Sherwood (1995) as reported by Stearns (2000) and sample graph from this work. Sherwood asserted that the effect of the magnitude of Von - Mises stress lies between 0 degree and 40 degree contact angle. The results were in good agree as revealed by the shapes of the curves.

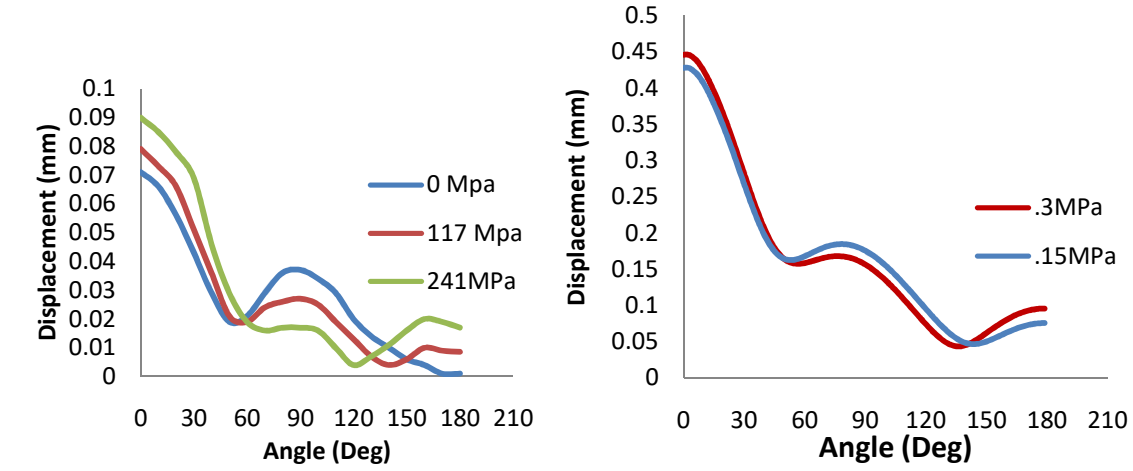

a b

Fig. 4.55: Comparison of displacement curves: (a) Stearns curve at 3114 N radial load (Stearns, 2003): (b) Displacement curves at 4750 N radial load

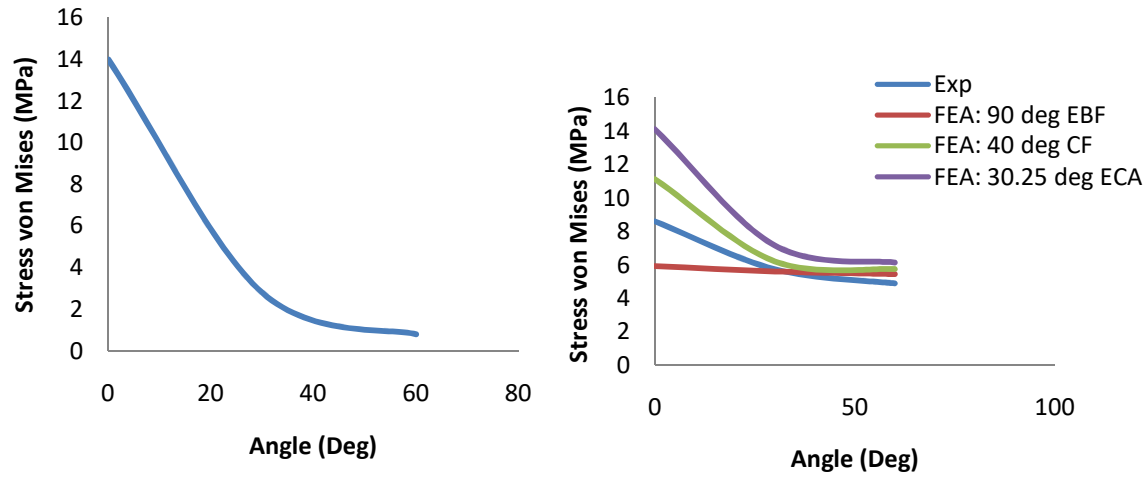

a b

Fig. 4.56: Comparison of Von - Mises stress at inboard bead seat: (a) Sherwood curve, 1995; (b)Stress at 4750 N radial load and 0.3 MPa inflation pressure

4.11 Results FromANOVA

Sample results from two factor ANOVA ($\alpha_{0.05}$) are shown in Appendix (D1-D36) representing relationship between the experimental values and the different loading function angles of 90 degree, 40 degree and ECA, at the same circumferential angular location of the inboard bead seat, outboard bead seat and well. There were no significant difference between the experimental and the FE values.

4.12Numerical Study

Having validated the FE results with the experimental results, a numerical study of the effect of cooling hole geometry was carried out

4.12.1 Effect of cooling hole geometry

Figure 4.57 (a & b) show the wheels with quadrilateral and oval cooling holes each with the same cooling hole area of 3466 mm^2 as the original wheel model and, aspect ratios of 0.78 and 0.71, respectively .Figures 4.54 to 4.56 give graphic views of the induced stresses induced on the experimental and Numerical models.

a 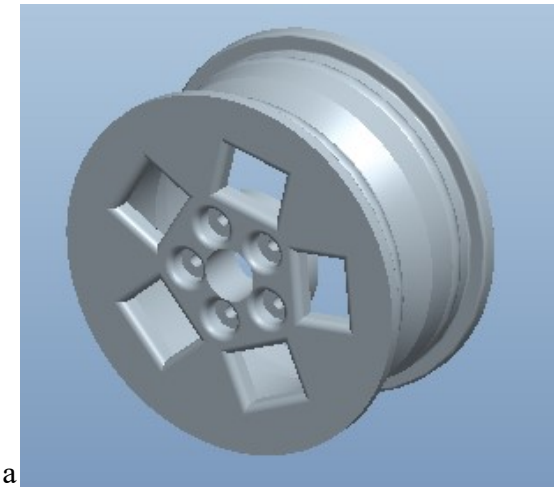 b 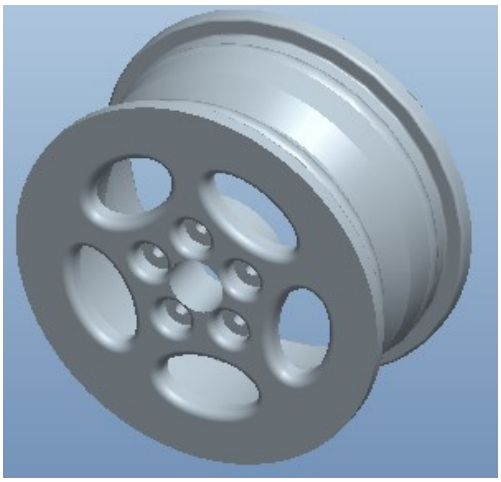

Fig. 4.57: 3-D Model of wheel of area 3466 mm^2 (a) Quadrilateral cooling hole; (b) Oval cooling hole shape

Figure 4.58 shows plots of the numerical and experimental stress values at 30.25 degree contact angle at 4750 N radial load and 0.3 MPa inflation pressure at the inboard bead seat. The maximum stress respectively for quadrilateral cooling hole, oval cooling hole, parabolic-cooling-hole numerical model and parabolic-cooling-hole experimental model were about 7.13, 7.01, 14.11 and 7. 44 MPa. The corresponding mean stress values were 4.83, 4.69, 5.45 and 5.33 MPa, respectively. From the results, oval shape cooling was least stressed followed by the quadrilateral cooling hole, and the parabolic-cooling-holenumerical and experimental model. With quadrilateral cooling hole employed, there was reduction in the maximum and mean stress at the inboard of about 49% and 11%, respectively when compared with the parabolic-cooling-hole numerical model. The corresponding drop in maximum and mean stress, when compared with parabolic-cooling-holeexperimental model, was about 4% and 9%, respectively. With the use of oval shape cooling hole, a drop in maximum and mean of about 50% and 14%, respectively was observed when compared with numerical model. The corresponding drop in stress value when compared with experimental model was about 6% and 12%, respectively.

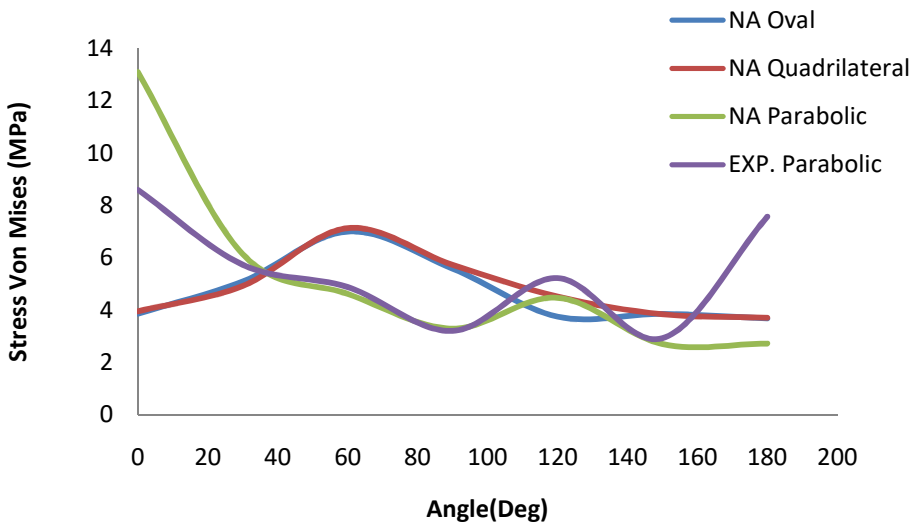

Fig. 4.59: Comparison of the numerical stress values at contact angle of 30.25 degree with experimental results at Inboard bead seat at 4750N radial load and 0.3 MPa Inflation pressure

Figure 4.60 represent plots of the numericals and exprimental stress values at 30.25 degree contact angle at 4750 N radial load and 0.3 MPa inflation pressure at the well. The maximum stress respectively, for quadrilateral cooling hole, oval shape cooling hole, parabolic-cooling-hole numerical model and parabolic-cooling-hole experimental model with parabolic cooling holes were about 6.91, 6,08, 12.9, 9.19 MPa, The corresponding mean stress values were 4.96, 4.76, 6.29 and 6.75 MPa, respectively. At the well, the wheel with oval shape cooling hole was least stressed followed by the quadrilateral cooling hole, and the parabolic-cooling-hole numerical model and parabolic-cooling-hole experimental model. With quadrilateral cooling hole employed, there was reduction in the maximum and mean stress at the well of about 46% and 21%, respectively when compared with the parabolic-cooling-hole numerical model. The corresponding drop in maximum and mean stresses, when compared with parabolic-cooling-hole experimental model, was about 25% and 27%, respectively. With the use of oval shape cooling hole, a drop in maximum and mean stress values of about 53% and 24%, respectively was observed when compared with parabolic-cooling-hole numerical model. The corresponding drop in stress value when compared with parabolic-cooling-hole experimental model was 34% and 29%, respectively.

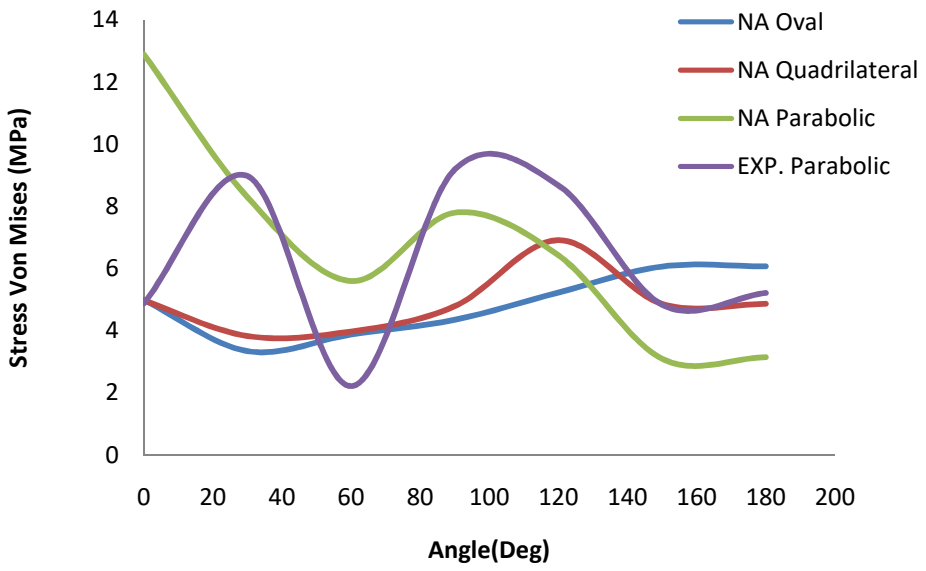

Fig. 4.60: Comparison of the numerical stress values at contact angle of 30.25 degree with experimental results at the well at 4750N radial load and and 0.3 MPa Inflation pressure

Figure 4.61 represent plots of the numerical andexperimental stress values at 30.25 degree contact angle at 4750 N radial load and 0.3 MPa inflation pressure at the well. The maximum stress, respectively for quadrilateral cooling hole, oval shape cooling hole, parabolic-cooling-hole numerical model and parabolic-cooling-hole experimental were about 3.56, 3.40, 3.64 and 9.74 MPa. The corresponding mean stress values were 2.00, 1.91, 2.50 and 4.86 MPa respectively.

With quadrilateral cooling hole employed, there was reduction in the maximum and mean stress values at the well of about 2% and 20%, respectively when compared with the parabolic-cooling-hole numerical model.

The corresponding drop in maximum and mean stress values, when compared with parabolic-cooling-hole experimental model, was about 63% and 59%, respectively.

With the use of oval shape cooling hole, a drop in maximum and mean of about 7% and 61%, respectively was observed when compared with parabolic-cooling-hole numerical model. The corresponding drop in stress value when compared with parabolic-cooling-hole experimental model was 65% and 61%, respectively.

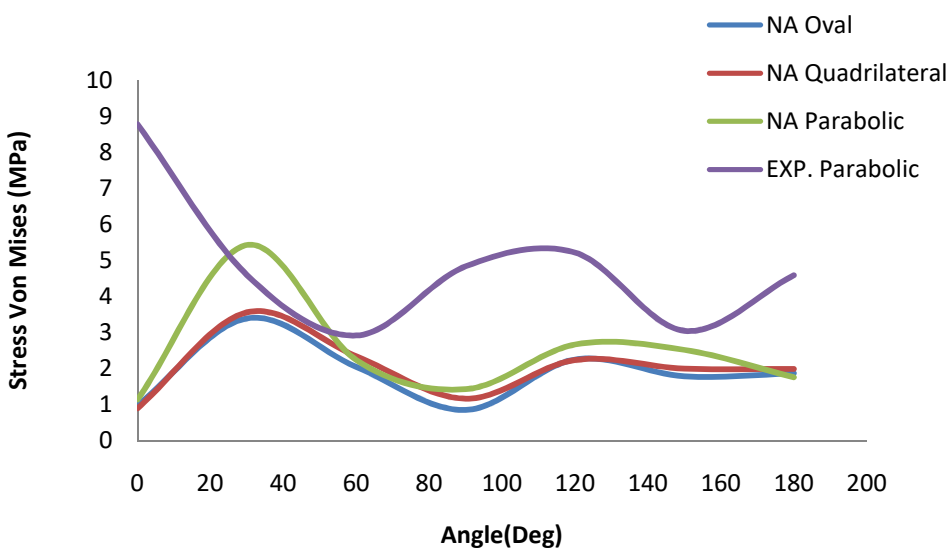

Fig. 4.61: Comparison of the numerical stress values at contact angle of 30.25 degree with experimental results at the outboard bead seat at 4750N radial load and and 0.3 MPa Inflation pressure

4.12.2 Effect of Aspect on the Mechanical Response

The Aspect ratios (AR_s) of 1, 0.5, 0.33 and 0.25 were considered for the cooling holes. For triangular cooling hole, the AR was terminated at 0.5 because it was observed that beyond the equilateral triangular cooling hole, an aspect ratio of 0.5 and beyond lead to greater stress and displacement values and overlapping of cooling holes leading to snapping-off of the web or arm of the wheel, thus, resulting to an open ended cylinder. Figures 4.62, 4.63, 4.64 and 4.65show quadrilateral shape cooling hole and oval shape cooling hole each at aspect ratio of 1, 0.5, 0.33 and 0.25, respectively.

From Figure 4.66 at aspect ratio of 1, it was observed that the wheel with an oval geometric cooling hole was least displaced with a maximum value at ground contact of about 0.191 mm, followed by that with quadrilateral cooling hole with a maximum displacement value of about 0.215 mm. The wheel with a triangular cooling hole was most displaced, with a maximum displacement value of about 0.272 mm.

From Figure 4.67 it could be seen that. the wheel with triangular cooling hole was most stressed with maximum value of Von-Mises stress of value of about 7.952 MPa, while that of the quadrilateral cooling hole and oval cooling hole, respectively, were about 7.530 MPa and 7.059 MPa .

Figures 4.68and 4.669show the effect of AR on the mechanical response of the wheel with triangular cooling hole. It was observed that at AR of 1, the maximum displacement value, Figure 4.63, occurs at ground contact with a value of about 0.272 mm, while that with AR of 0.5 triangular cooling hole was about .414 mm, representing an increase of about 52%. Their corresponding maximum Von-Mises stress values, Figure 4.64, were about 7.952 and 8.679 MPa respectively.

Figures 4.70and 4.71 show the effect of AR on the quadrilateral cooling hole geometry. From Figure 4.65, it could be seen that the maximum displacement values occurred at ground contact, with a maximum displacement value for quadrilateral cooling hole at AR of 1, 0.5, 0.33 and 0.215 were 0.199, 0.212 and 0.225 mm. respectively. The wheel with quadrilateral cooling hole of AR of 0.5 was the least displaced, while that with AR of 0.25 was most displaced.

The magnitude of stress and displacement and, shape of their curveswere affected by shape and aspect ratio of cooling hole

a 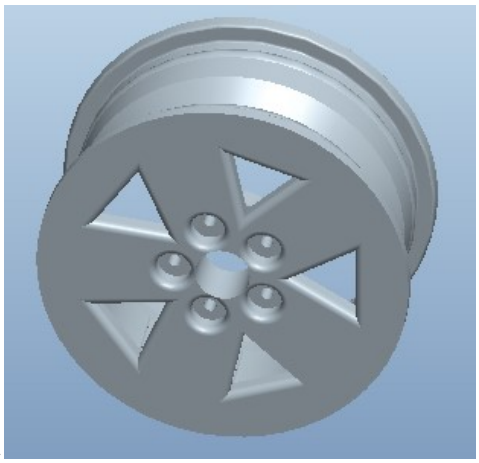 b 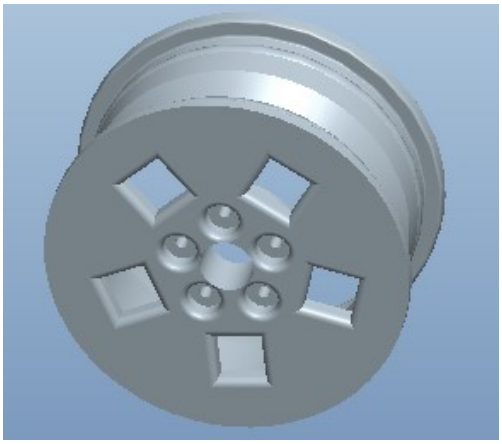

c 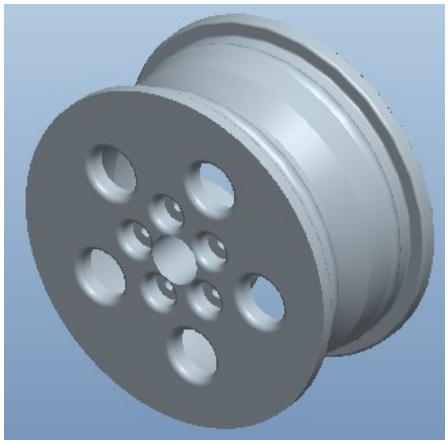

Fig. 4.62: Cooling holes with aspect ratio of 1: (a) Triangular (equilateral), (b) Quadrilateral, (c) (Oval)

a 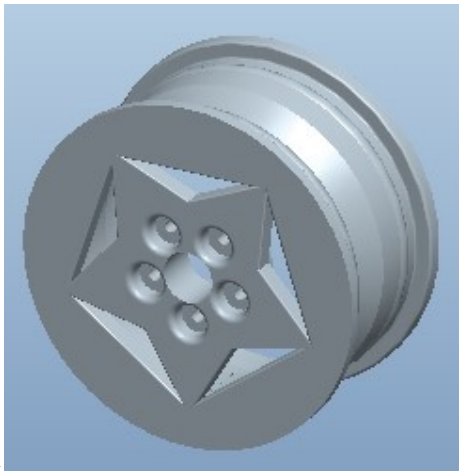 b 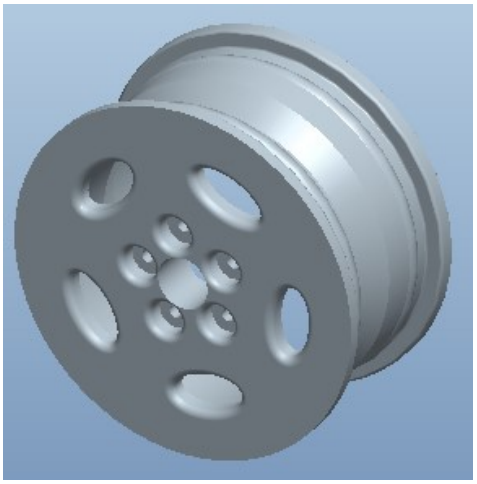

c 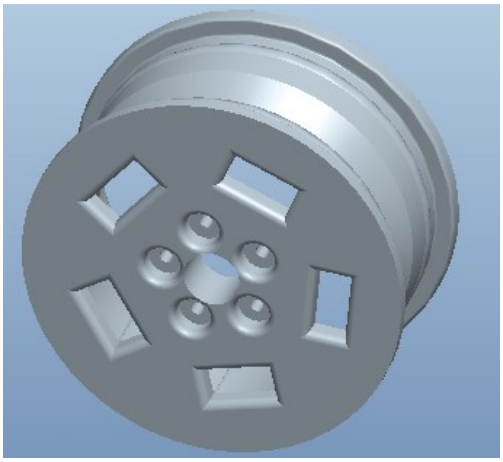

Fig. 4.63: Cooling holes with aspect ratio of 0.5: (a) Triangular (equilateral), (b) Quadrilateral, (c) Oval

a 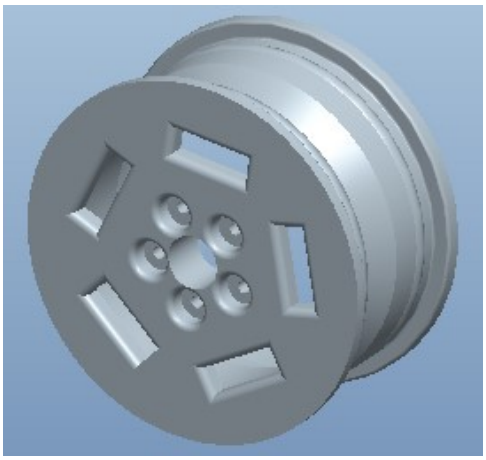 b 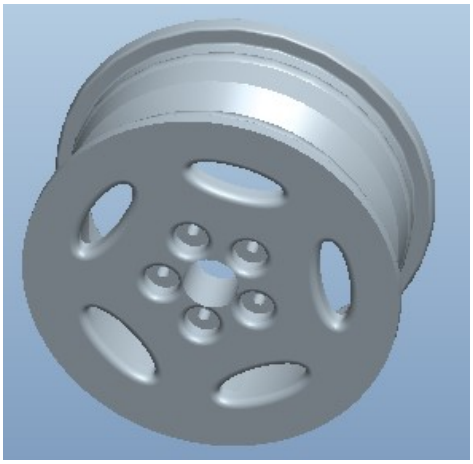

Fig. 4.64: Cooling holes with aspect ratio of 0.33: (a) Quadrilateral, (b) Oval

a 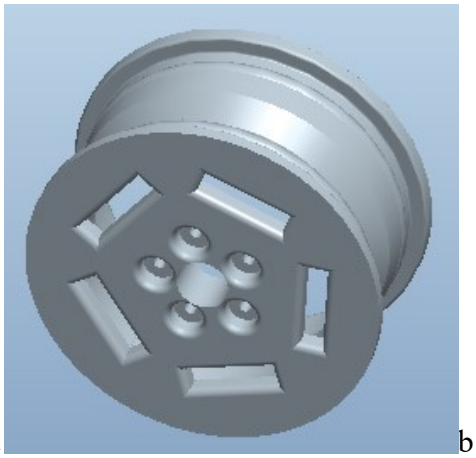 b 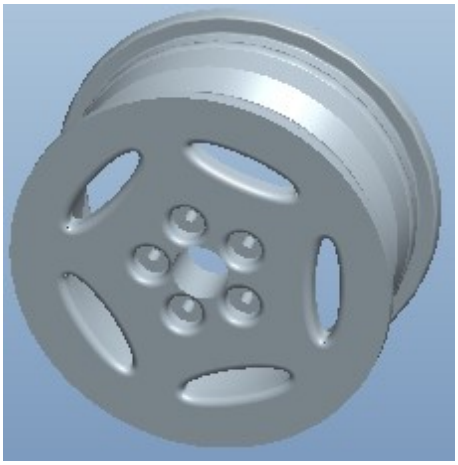

Fig. 4.65: Cooling holes with aspect ratio of 0.25: (a) Quadrilateral, (b) Oval

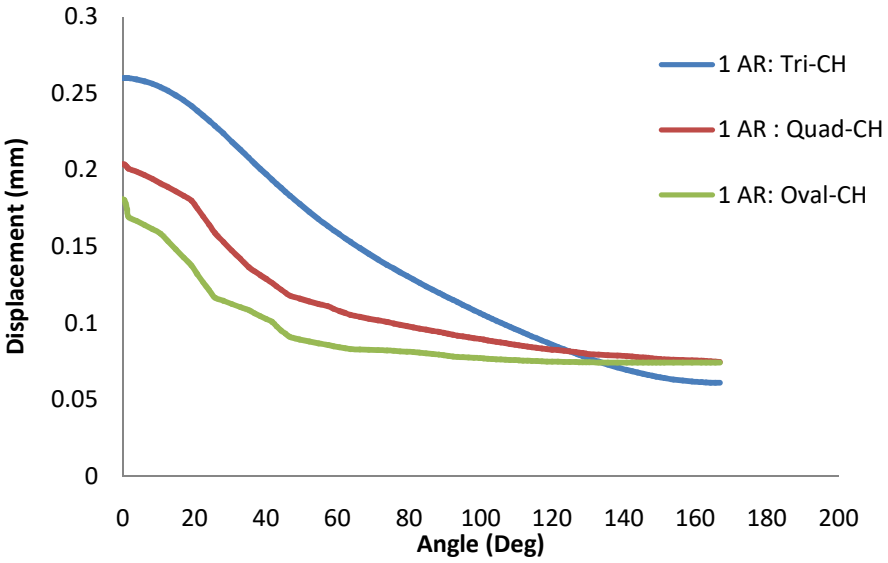

Fig.4.66: Effect of cooling hole geometry on the displacement at the inboard bead seat at 4750 N radial load and 0.3 MPa inflation pressure at Aspect Ratio of 1

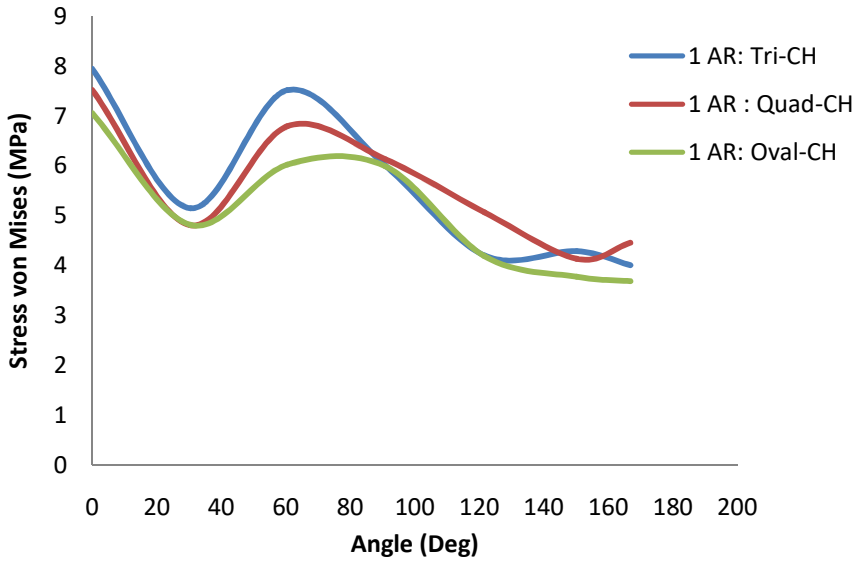

Fig. 4.67: Effect of cooling hole geometry on the Von-Mise stress at the inboard bead seat at 4750 N radial load and 0.3 MPa inflation pressureat aspect ratio of 1

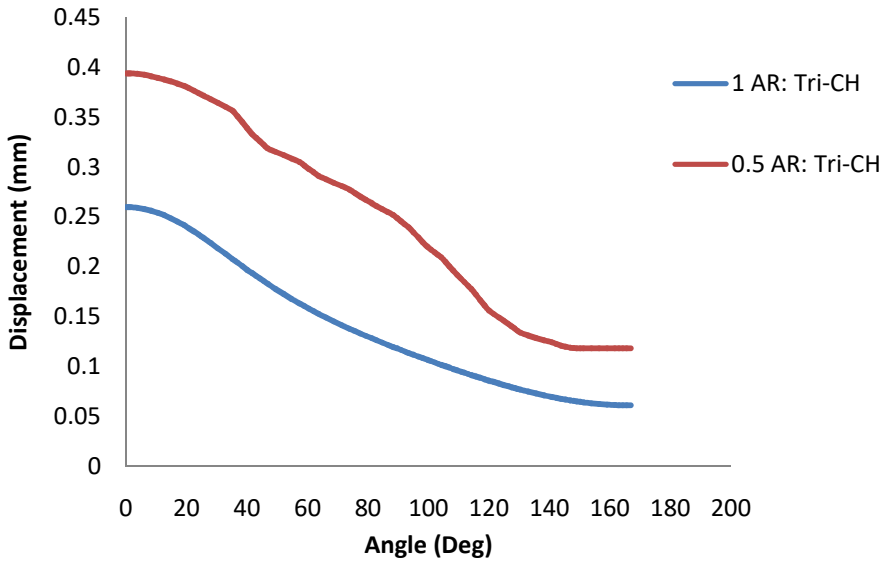

Fig. 4.68: Effect of aspect ratio on the displacement at the inboard bead seat at 4750 N radial load and 0.3 MPa inflation pressure for triangular cooling hole

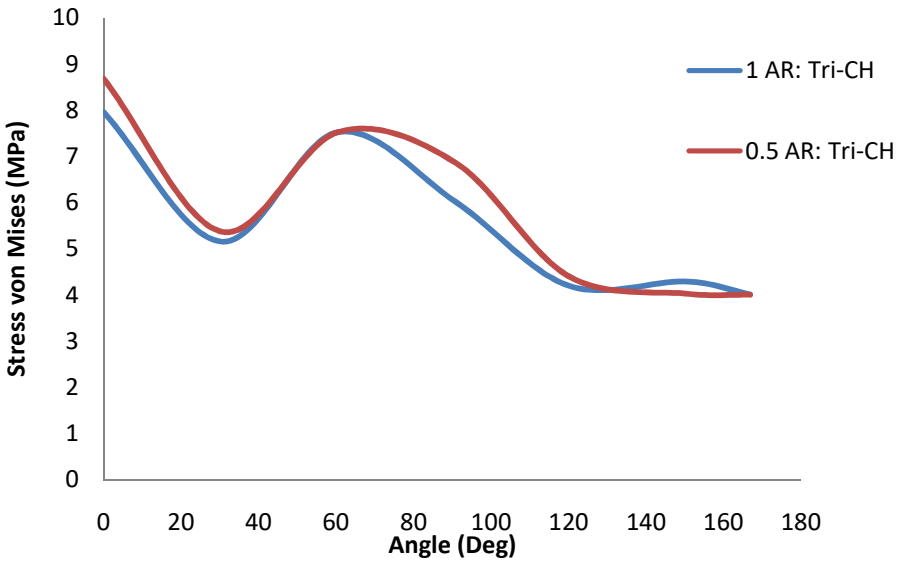

Fig. 4.69: Effect of aspect ratio on the Von-Mise stress at the inboard bead seat at 4750 N radial load and 0.3 MPa inflation pressure for triangular cooling hole

Figure 4.70 shows plots of the Von-Mise stress values of quadrilateral cooling hole at AR of 1, 0.5, 0.33 and 0.25 respectively.Their corresponding maximum Von-Mises stress values, Figure 4.71,were about 7.530, 6.433,7,120 and 7.236 MPa respectively. The least maximum stress value was that of the wheel with AR of 0.5 quadrilateral cooling hole, while that with aspect ratio of 1 quadrilateral cooling hole was most stressed.

Figures 4.72and 4.73 show the effect of AR of the oval shape cooling hole geometry. Figure 4.72shows the displacement plots for aspect ratios of 1 0.5. 0.33, and 0.25, respectively. Corresponding maximum displacement values ground contact of 0 degree were about 0.191, 0.184, .194 and .186 mm, respectively.Figure 4.68shows the graphics of the Von-Mises stresses at AR_s of 1 0.5. 0.33, and 0.25, respectively for the oval shape cooling hole. Corresponding maximum Von -Mises stress values were about 7.952, 6.277, 6.675 and 6.481 MPa respectively..

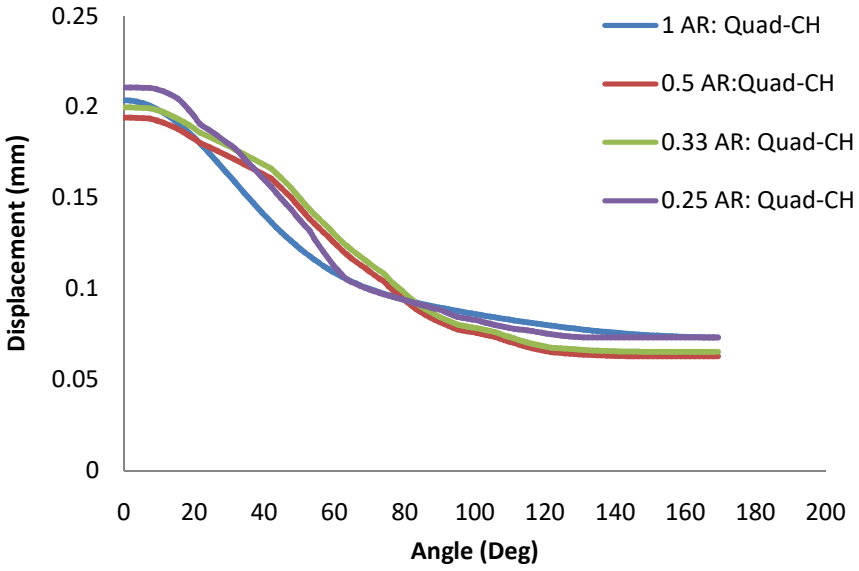

Fig. 4.70: Effect of aspect ratio on the displacement at the inboard bead seat at 4750 N radial load and 0.3 MPa inflation pressure for quadrilateral cooling hole.

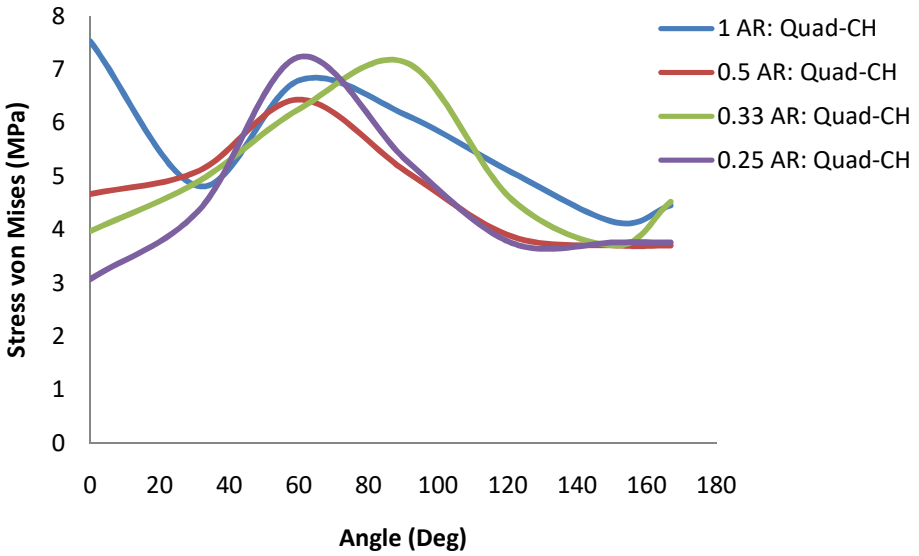

Fig. 4.71: Effect of aspect ratio on the Von-Mise stress at the inboard bead seat at 4750 N radial load and 0.3 MPa inflation pressure for quadrilateral cooling hole.

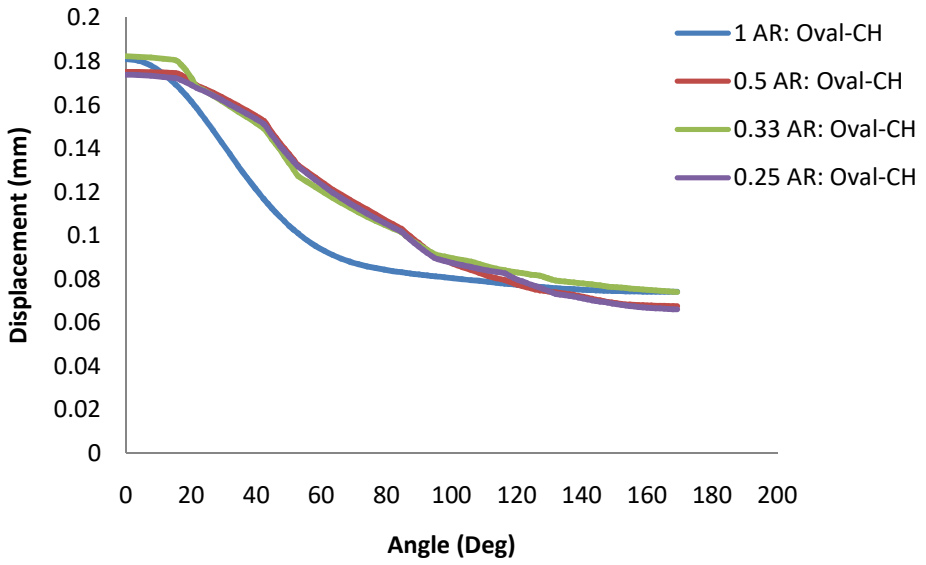

Fig. 4.72: Effect of aspect ratio on the displacement at the inboard bead seat at 4750 N radial load and 0.3 MPa inflation pressure for oval cooling hole.

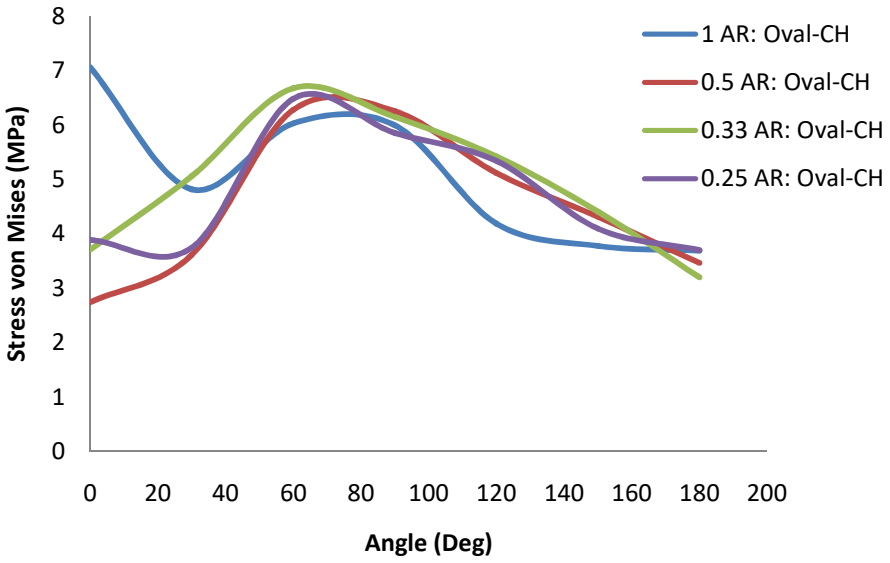

Fig. 4.73: Effect of aspect ratio on the Von-Mise stress at the inboard bead seat at 4750 N radial load and 0.3 MPa inflation pressure for oval cooling hole.

4.12.3 Effect of cooling hole combination on the mechanical response

Having analysed the various cooling geometries of triangular, quadrilateral and oval. It was observed that when corresponding cooling holes were compared at different aspect ratos, it was found that for the triangular set, the equilateral was least stressed and deformed when compared with other form of triangularly shaped cooling hole beyond AR of 1. For the set of quadrilateral cooling hole, that with AR of 0,5 had least values of stress and displacement, while for the set of oval shape cooling hole, that at AR of 0.5 experienced lowest stress and displacement values.

Figure 4.74 (a), (b) & (c) show the cooling holes' combination.A combination of the least stressed cooling hole geometries for each set, at the inboard bead seat at 4750N radial load and 0.3 MPa inflation pressure were analysed, viz: triangular cooling hole at AR 1and oval shape cooling hole at AR of 0.5; triangular cooling hole of AR1 and quadrilateral cooling hole at 0.5 AR and, quadrilateral cooling hole and oval shape cooling hole each at 0.5 AR. Figures 4.70 and 4.71 ,it was observed that the least stress and displaced combination was quadrilateral cooling hole and oval shape cooling hole each at AR of 0.5, with a maximum displacement value at ground contact of about 0.202 mm and a maximum Von-Mises stress value of about 6.59 MPa. The triangular cooling hole and oval shape cooling hole combination had a maximum displacement value at 0 degree location of about 0.258 mm and a maximum Von-Mises stress value of about 7.09 MPa, while that of triangular cooling hole and quadrilateral cooling hole combination has a maximum displacement value of about 0.270 mm and a maximum Von-Mises stress value of about 7.17 MPa.

a 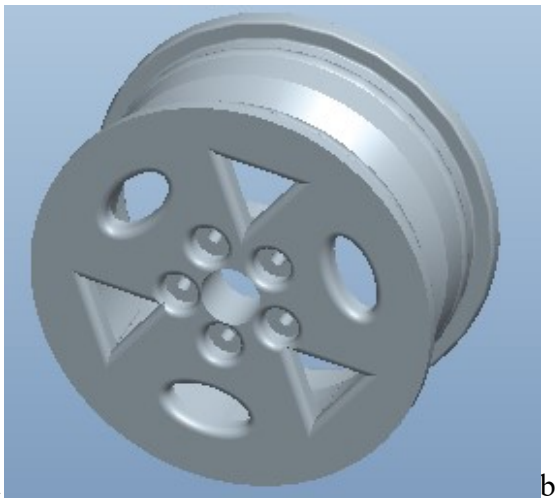 b 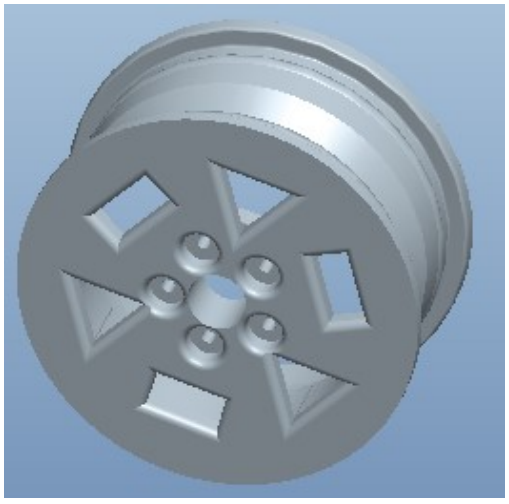

c 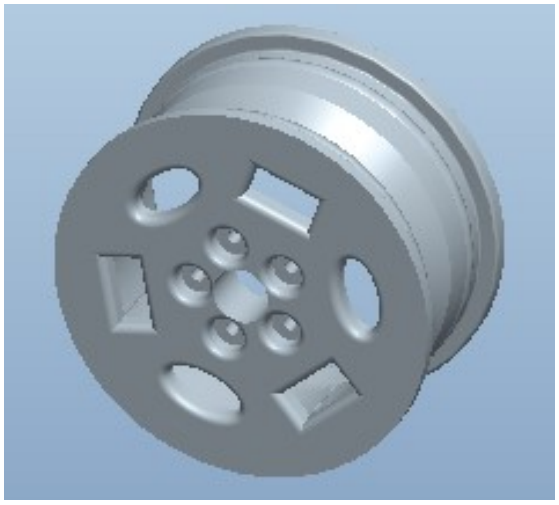

Fig. 4.74: Cooling holes combination: (a) Triangular (equilateral) and Oval (aspect ratio 0.5), (b) Triangular (equilateral) and Quadrilateral (aspect ratio 0.5), (c) Oval (aspect ratio 0.5) and Quadrilateral (aspect ratio 0.5).

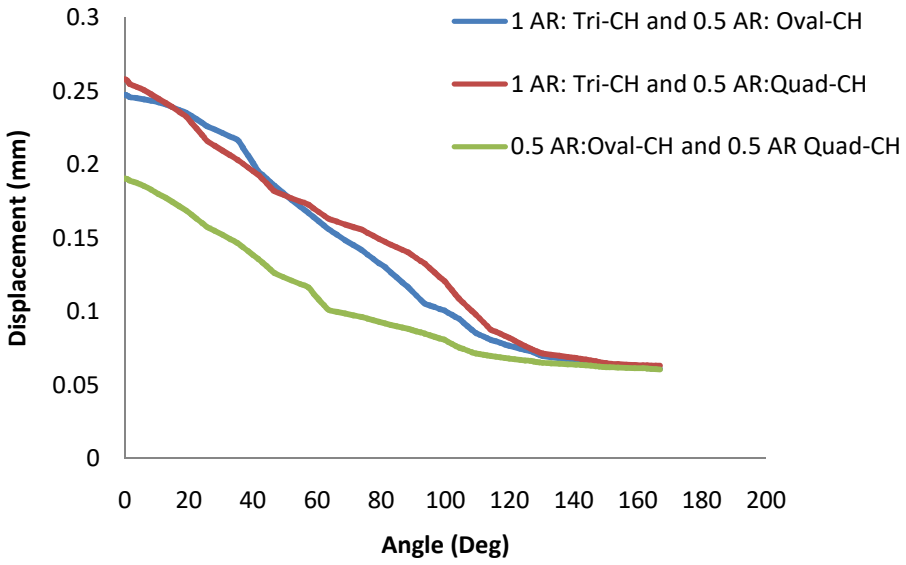

Fig. 4.75: Effect of cooling hole combination on the displacement at the inboard bead seat at 4750 N radial load and 0.3 MPa inflation pressure.

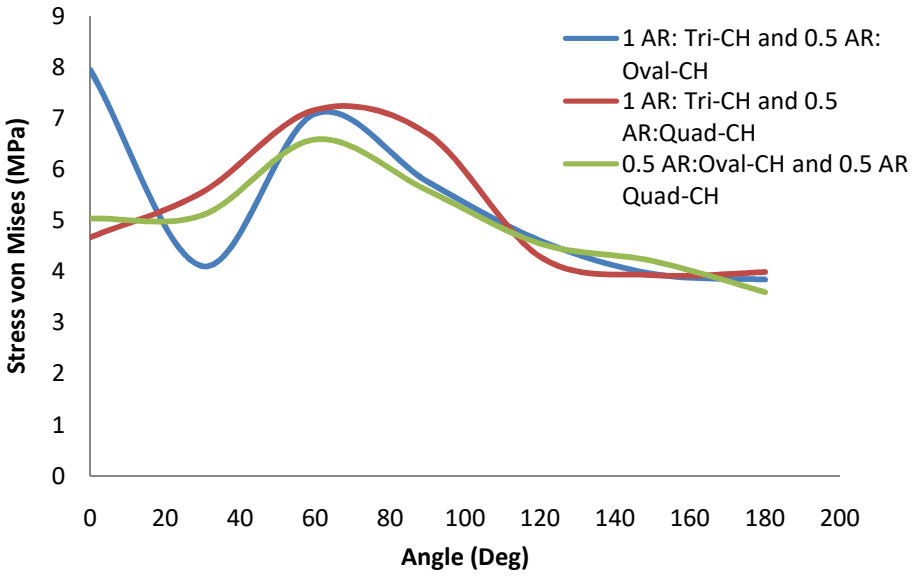

Fig. 4.76: Effect cooling hole combination on the Von-Mise stress at the inboard bead seat at 4750 N radial load and 0.3 MPa inflation pressure.

4.13 Effect of air hole location

Figure 4.77 (a) and (b) show the locations of the air hole considered. While a location at mid-point (central) between spikes was considered for Figure 4.77 (a), a location offset towards one spike was considered for Figure 4.77 (b). Figure 4.79 shows the plots of displacement values at 4750 N radial load and 0.3 MPa inflation pressure. Results showed that the maximum values at ground contact when the air hole was offset is about 0.44 mm, while that for central location is about 0.43 mm; a difference of about 2%. Their mean displacement values were each about 0.17 mm. The presence or location of the air hole does not significantly affect the me the wheel,

a  b 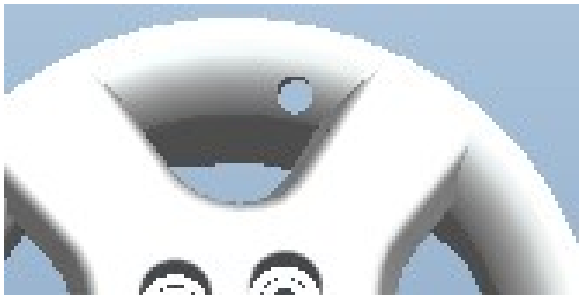

Fig.4.77:Air hole location: (a) Central; (b) Offset.

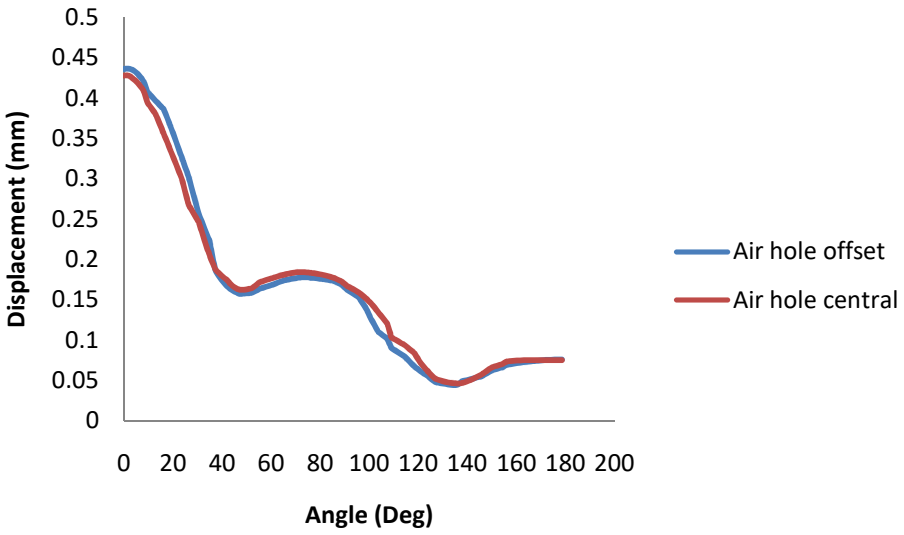

Fig. 4.78: A comparison between air hole location at 4750 N radial load and 0.3 MPa inflation pressure at 30.25 contact angle.

CHAPTER FIVE

5.0CONCLUSION

1. The stress values at the Well, Inboard and Outboard for the quadrilateral al cooling hole wheel were reduced by about 21%, 11% and 59%, respectively when compared with the wheel with parabolic cooling hole. Corresponding reduction in stress values for the oval shape cooling hole wheel were about, 24%, 14% and 75% respectively.

2. Inflation pressure variation affects the magnitude of stress on the rim locations of the inboard bead seat, well and outboard bead seat. When inflation pressure was halved the stress valueswere reducedby about 42%, 56%,and 38%, respectively at the well, inboard and outboard bead seats. While doubling the inflation pressure, increased the stresses at well, Inboard and Outboard bead seats by about 92%, 67% and 85%, respectively.

3. Load variation also affects the magnitude of the stresses induced on the wheel. For an increase in load from 3750 N to 4750 N, that is an increase of about 25% load, increased the stresses at locations of the well, Inboard and Outboard by about 117%, 145%, and 73%, respectively. While a decrease in load from 4750 N to 3570 N reduce the stresses at corresponding locations of the Well, Inboard and Outboard by about 51%, 56% and 40%, respectively.

4. The well was the most stressed location on the rim which is in agreement with literature findings.

5. From the results obtained it could be said that the exact angular location on the rim‘s outboard bead seat where the greatest stress and strain act could not be readily ascertained. It lies atcircumferential angles of between 30 and 150 degree. This may probably be due to the orientation of the spikes.

6. From the results obtained, it could be said that the highest stressat both the inboard bead seat and well lie at the point of contact with the ground, that is, at zero degree contact angle.

7. In employing the contact patch analogy, it was observed that the load distribution angle, the mean contact angle was 30.25.degree. From literature search the load distribution angle approximately30,40or 90 degree.

8. The most deformed location on the rim is at the inboard bead seat at point of contact with the ground (zero degree contact angle) for all range of loading function distribution which agrees favourably with literature findings.Displacement for 30.25 contact angle was highest, followed by 40 degree CF and then 90 degree EBF.

9. A higher inflation pressure is accompanied by a corresponding higher displacement values at the point of contact at the inboard, well, and outboard

10. An increase in radial load from 3570 N to 4750 N increases the displacement value by between 3% and 88%, depending on the load distribution angle and inflation pressure.

11. Results show that at aspect Ratio of 1, the wheel with triangular cooling hole was most stressed and deformed when compared with similar wheels of oval or quadrilateral cooling holes.The wheel with oval cooling hole was least stressed and deformed, while the stress and displacement values for the quadrilateral cooling hole lie in-between. The hihgest stress values at AR of 1 for triangular, quadrilateral and oval cooling holeswas about 7.952, 7.530 and 7,059 MPa, respectively. The highest integrity of the oval shape cooling hole alumnium alloy wheel is established. '

13. It was observed that at aspect ratio of 0.5, maximum displacement and stress values for quadrilateraland oval cooling holes were lowest when compared with values at aspect ratios of 1,0.33 and 0.25. Values for oval cooling hole were lower than those of quadrilateral cooling hole. The values for the triangular cooling hole at aspect ratio of 0.5 were much higher. Beyond aspect ratio of 0.5, for the triangular cooling hole, led to the snapping-off of the arm. The maximumstress value for the triangular cooling hole at AR of 0.5 was increased by about 9% when compared with that at AR of 1. The higheststress value for the quadrilateral cooling hole wheel was reduced by about 20%, 5% and 4% at ARs of 0.5, 0.33 and 0.25, respectively when compared with that at AR of 1. Stress value

for the oval cooling hole wheel was reduced by about 11%, 5% and 8% at ARs of 0.5, 0.33 and 0.25, respectively when compared with that at AR of 1.

13. The displacement value for the triangular cooling hole at AR of .5 was increased by about 52% when compared with that at AR of 1. The displacement for the quadrilateral cooling hole wheel was reduced by about 7% and 1% at ARs of 0.5 and0.33, respectively when compared with that at AR of 1. While at AR of 0.25, the displacement was increased by about 5%. The displacement for the oval cooling hole wheel was reduced by about 4% and 3% at ARs of .5 and .25, respectively when compared with that at AR of 1. While at AR of 0.33, the displacement was increased by about 2%.

14. The cooling hole combination with highest integrity was the oval and quadrilateral at aspect ratio of 0.5 with a displacement and stress values of about .202 mm and 6.57 MPa, respectively when compared with triangular-quadrilateral cooling hole combination and triangular-oval cooling hole combination with displacement and stress values of about .270 mm and 7.17 MPa and .258 mm and 7.09 MPa, respectively.

15. The presence or location of the air hole does not significantly affect the me the wheel,

. The results are considered to be able to contribute to the development of wheels and, the data obtained through this study can be utilized for the design of wheels.

5.1 Recommendations

1. Further experimental works are needed in order to determine accurately the exact loading function. Research in this area is still ongoing.

2. The study revealed that cooling hole shape and aspect ratio influenced the structural integrity of a wheel. It also identified oval cooling hole shape at aspect ratio of 0,5 as the foremost shape .

REFERENCES

Allen, S. H, Alfred, R. H And Herman, G. L. 1961. *Machine Design. Schaum Outline Series McGraw - Hill*, USA., 37-54.

Anonymous., 2006. The global aluminum industry: *Review and forecast* [J]. JOM, 58(11), 10.

Baeumel, A and Seeger, T., 1990.Materials data for cyclic loading.*Amsterdam. Elsevier service.*

Blake, A. 1990.,*Practical Stress Analysis in Engineering Design, McGraw-Hill, New York.* . 363–367.

Borase, K. H and Deore, E. R. 2016. Studying Effect of Pressure on Rim.*International Journal for Research In Multidisplinary Field*. ISSN - 2455-0620, 2 (6) 95-99

Carvalho, C, Voorwald, H and Lopes., 2001., *Automobile wheels – an approach for structural analysis and fatigue life prediction*, SAE paper no. 01 – 4053.

Carret, T.K., Newton, K. & Steeds, W., 2000.Chapter 41 Wheels and Tyres.*Journal of Motor Vehicle*, 13, 1085-1108.

Cerit, M., 2010.Numerical simulation of dynamic side impact test for an aluninum alloy wheel. *Scientific research and essays*.5(18), 2694-2701..

Chia-Lung, C. and Shao-Huei, Y., 2009. Simulation of wheel impact test using finite element method. *Engineering failure analysis*, 16(17), 11-1719.

Chu, C., Conle, F. A. and Bonnen, J. F., 1993. Multiaxial stress–strain modeling and fatigue life prediction of sae axle shafts. In: McDowell DL, Ellis R, editors. *Advances in multiaxial fatigue*.ASTM STP 1191. Philadelphia: American Society for Testing and Materials, 37–54.

Currie, A., 2000. Finite Element Analysis of an Automotive Wheel: A Case Study, National Conference Publication, *Institution of Mechanical Engineers*, Australia. 16–20.

Das K. and Yin, W., 2007. The worldwide aluminum economy: *The current state of the industry* [J]. JOM, 59(11), 57−63.

Dowling, N., 1982. A discussion of methods for existimating fatigue life.*SAE Technical paper* no. 820691.

Ducker Worldwide., 2009. Update *on North American: light vehicle aluminum content compared to the other countries and regions of the world* (phase II).

Esaulov, V. and Sladkovskii, A., 1991. Stress Strain state of Solid Railway Wheel.*Strength of materials*, 2 (10), 1486-1486.

Fadare, D. A., Odebunmi, O. O. and Igbudu, S. O., 2011 Finite element modelling of an aluminium allouy automobile rim under static load. *Ife journal of technology*. 20(2), 75-80.

Fancher, P. S.and Bareket, Z., 1993. Including roadway and tread factors in a semi-emperical model of truck tyres. Tyre models for vehicle dynamics analysis. *Proceedings of 1st international colloquium on tyre models for vehicle system dynamics Amsterdam.Swetz and Zeitlinger.*

Ferreira, G., 1992.*Algor Software Helps Leading Brazilian Wheel Manufacturer ReduceCosts,* Algor Design World..

Firat, M. and. KocabıcaK, U., 2004.Analytical durability modeling and evaluation–complementary techniques for physical testing of automotive components.*Eng. Failure Anal.* 11(4):655–74.

Gergele, J., 1983. Weight of Wheels, Centre D'etudes et de Recherches Michelin, France.

Grbisic, V. and Fisher, G. 1984.Procedure for optimal light-weight design and durability testing of wheels. Int J Vehicle Design 5(6):659–71.

Grbisic, V. and Fisher, G., 1983. Automotive wheels, methods and procedure, optimal design testing. *SAE*-830135.

Hahn, G. T., Bhargava, V., Yoshimura, H. and Rubin., C., 1984 Analysis of RollingContact Fatigue and Fracture. *International Conference on fracture*, 6, 295-316.

http://www.measurementsgroup.com., 2001. M - Bond 43 - B, 600 and 610 installation, 1 - 20.

http://www.offroaders.com/info/tech-corner/reading/wheels.htm (24/7/2012).

Igbudu, O. S. and Fadre, D. A., 2015. Effect of Radial Load Distribution Pattern On The Displacement Of Automobile Aluminium Allot Wheel - Strain Energy Approach. *First University Of Ibadan Technology Conference* (UITECH2015), 358-367.

International Aluminium Institute., 2007. *Improving sustainability in the transport sector through weight reduction and the application of aluminum*.

ISO 3006., 1976. Road vehicles-passenger car wheels- fatigue testing methods, 2, Switzerland.

Janardhan, J., Kumar, R. V. and Lalitha, N. R. 2014.Radial Fatigue Analysis of An Alloy Wheel *Int. Journal of Engineering Research and Applications*www.ijera.com ISSN : 2248-9622, 4 (12) 6, 253-258

Jeusette, T., 1992. Finite element analysis of tyre/rim interface forces under braking. *Tyre Science and Technology* 20(2):83-105.

Jirang,, C., Hans, J. and Roven, J., 2010. Recycling of automotive aluminum.*Trans Nonferrous Met,*China 20(20) 57-2063.

JISD 4103., 1989. Japanese Industrial Standard.Disc wheel for automobiles.

Karandikar, H. and Fuchs, W., 1990.*Fatigue life prediction for wheels by simulation of the rotating bending test*.SAE technical paper, 900147.

Jitendra Shinde, Sunil Kadam, Samuvel Pandit 2017 Review Paper on Design and Analysis of Automotive Wheel Rim Using Finite Element Analysis. *International Research Journal of Engineering and Technology* (IRJET) e-ISSN: 2395-0056 4(7), 2723-27235

Karl, H., 1996. *Practical Hints For Installation of Strain Gages*, 4th Revised Edition, 1 - 54.

Kawashima, H. and Ishihara, K., 1989. Stress Evaluation of Automotive Steel Road Wheel Under Radial Load, *Nippon Kikai Gakkai Ronbunshu*, C Hen, 55(513), 1254-1258.

Kocabicak, U. and Firat.M., 2001.Numerical analysis of wheel cornering fatigue tests.*Engineering failure analysis* 8, 39-54.

Konishi, H., Fujiwara, A., Katsura, T., Takeuchi, K .and Nakata, M., 1996. ImpactStrength of Aluminum alloy Wheel (Influence of Disk and Rim Rigidity on the JWLImpact Strength of Aluminum alloy Wheel)," *Nippon Kikai GakkaiRonbunshu, CHen* 62(599) 2884-2890.

Kouichi, A and Ryoji, I., 2002.*Shortening design and trial term for aluminium roadwheel* by CAE, casting technology (Japanese), 74, 533 – 538.

Kruse, G and Mahning, F., 1976. A comprehensive methods for wheel testing by stress analysis. *SAE Tecnical Paper Series*, 760042.

Landgraf, R., Thangjitham, S. and Ridder, R., 1994. Automotive Wheel Assembly: A Case study in Durability Design. *ASTM Special Technical publication*, 5-22.

Leslie, L. K., 1986. Tyre soil interaction model for turning (steered) tyres. *Journal of terramechanics* 23(3), 153-169.

Li, P, Lee, P. D, Lindley, T. C., Maijer, D. M., Davis, G. R and Elliot, J. C., 2006.*Adv. Eng. Mater*. 8, 476-479.

Li, P., Maijer, D. M., Lindley, T. C. and Lee, P. D., 2007.A through process model of the impact of in-service loading, residual stress, and microstructure on the final fatigue life of an A56 Automobile wheel.*Material science and engineering* 20(30) 460-461

Li, P., Maijer, D. M., Lindley, T. C. and Lee, P. D., 2007.Simulating the residual stress in an A356 automobile wheel and its impact on fatigue life.*The mineral, metals and materials society and ASM international.*

Liangmo, W., Yufa, C., Chenzhi, W. and Qingzheng, W., 2011 Fatigue life analysis of aluminium wheels by simulation of rotary fatigue test. Strojniski Vestnik – *Journal of mechanical engineering* l57(1), 31 – 39.

Mattia Merlin, GiulioTimelli, Franco Bonollo and Gian LucaGaragnani 2009.Impact behaviour of A356 alloy for low-pressure die casting automotive wheels.*Journal of Material Processing Technology*, 209 (2), 1060-1073.

Mehemet, F., Recep, K., Murat, O. and Hamid, M., 2009. Numerical modeling and simulation of wheel radial fatigue teats.*Engineering failure analysis*. 16, 1535-1541.

Mizoguchi, T., Nishimura, H., Nakata, K.and Kawakami, J., 1982. *Stress Analysis andFatigue Strength Evaluation of Sheet Fabricated 2 - Piece Aluminum alloy Wheels for Passenger Cars*," R&D, Research & Development (Kobe Steel, Ltd) 32(2), 25-28.

Mohamed Lukhman, M. , Naveen Kumar, M., Venkatesan, J., Sathish kumarS, Srinavinapriya, D.2017.Design and Analysis of Al 356.2 and ZK60A Wheel Rim with

Radial and Spiral Flexures.*International Journal of Advance Engineering and Research Development* 4(5), ISSN, 2348-6406.

Mohd, I. F. B. B., 2011. Simulation test of automotive alloy wheel using computer aided engineering software. *http://umpir.ump.edu.*my/143/11. 31/03/11.

Morita, Y and Sumimoto, Y., 1987. Finite Element Analysis of a Steel Road Wheel*Metals Publication* 35(3), 89–106.

Morita, Y., Kawashima, H. and Ishihara, K., 1989 Induced Stress Evaluation ofAutomotive Steel Road Wheel During Endurance Tests, *Sumitomo Metals*, 41(2), 27-34.

Morita, Y.,Kawashima, H., Ishihara, K and. Komatsu, H., 1987. Finite Element Analysis of a Car Wheel, *Sumitomo Metals*, 39(3), 245-263.

Muhammet, C., 2010. Numerical simulation of dynamic side impact test for an aluminium alloy wheel.Scientific research and essays, 5(18), 2494 – 2710.

Nallusamy, S., Mankanda Prabu, N., Balakannan and Gautam Majumdar, 2015. Analysis of Static Stress in an Alloy Wheel of the Passengercar", International Journal of Engineering Research in Africa, (16), 17-25.

Nigerian Pilot, 2016.Disturbing road accidents statistics in Nigeria. Editorial, March, 10

Noda, T., 1982. Development of Aluminum alloy Disk Wheel for Truck and Bus. *SAE Technical Paper Series*, 820343,

Panithi Dasu, L. Abhilash, 2016. Fatigue Analysis of Aluminum Alloy Wheel, *International Journal of Research in Mechanical Engineering & Technology*,P-ISSN 7(1), 47-55

Raju, R., P, Satyanarayana, B., Ramji, K and Babu, S. K., 2009. Evaluation of fatigue life of aluminium alloy wheels under bending loads. *Fatigue and Fracture of Engineering Materials and Structure* 32(2), 119–126

Raju, R., Satyanrayana, B., Ramji, K. and Suresh, B. K., 2007. Evaluation of fatigue life of aluminium alloy wheels under radial loads. *Engineering failure analysis* 14, 791- 800.

Ramamurti, V. and Srinivasan, V., 1981. Stress Analysis of Webs of Rimmed Wheels. *Journal of Strain Analysis for Engineering Design*, 161, 1-8.

Rao, S. S., 1992. *The Finite Eement Methods in Engineering*.2nd Edition. Paragon Press plc, Headington Hill Hall, Oxford OX3 OBW, England.

Razak, I. M., 2015 Design And Development of Alloy Wheel. *https://www.researchgate.net/profile/Muhammad_Ikhwan_Razak*

Reipert, P., 1985. Optimization of an Extremely Light Cast Aluminum alloy Wheel Rim *International Journal of Vehicle Design*, 6(4-5), 509-513.

Richard, C. and Rice, M., 1988.*SAE Fatigue design handbook*. 2nd ed. Warrendale (PA): SAE Publication..

Riesner, M. I. and 'DeVries, R., 1983. Finite element analysis and structural optimization of vehicle wheels.*SAE technical paper*, 830133.

Rihda, R., 1976. Finite element analysis f Automotive Wheels.*SAE technical publication*, 760085.

Rombach, G. and Kuckshinrichs, W., 2002 The future of automotive aluminium [C]//TMS Annual Meeting. Seattle, 1003−1010.

Sakyann, V. G., 1996. *Lecture notes on Strength of Materials, FUT, Minna*, Unpublished.

Shang, R. and Altenhof, W., 2005.Wheel impact performance with consideration of material in homogeneity and a simplified approach for modeling, international journal Crashworthiness 10, 137 – 150.

Shang, R., Altenhof, W., Hu, H and Li, N., 2008. Rotary fatigue analysis of forged magnesium road wheels.*SAE technical paper*, 2008-01-0211.

Shang, R., Li, N., Altenhof, W. and Hu, H., 2004. Dynamic side impact simulation of aluminium wheels incorporating material property variations, Aluminum. *The minerals, metals & materials society.*

Sherwood, J. A., Ayres, J. M., Gross, T. S. and Watt, D., 1995. An investigation of tyre-wheel interface loading using ADINA. *Computers and structures*, 56(2-3), 377-87.

Sourav Das (2014) Design and Weight Optimization of AluminiumAlloy Wheel *International Journal of Scientific and Research Publications*, 4 (6) ISSN 2250-3153

Stearns , J. C., 2000. *An investigation of stress and displacement distribution in aluminium alloy automobile rim.* Ph.D thesis, University of Akron, 1-22, 128 -170.

Stearns, J., Srivastan, T. S., Prakesh, A. and Lam, P. C., (2003) Modelling the mechanical response of aluminium alloy automotive rim. *Material science and engineering* A366, 262-268.

Stroud, K. A., 1996.*Further Engineering Mathematics*.3rd Edition. Macmillan Press ltd.

Tanaka, K.., Ishihara, K and. Komatsu, H., 1987. Fatigue Strength of Car Road Wheels, *Sumitomo Metals*, 39(4), 325-336.

Team, Z., 2014. *Different types of tyres*. www.zigwheels.com.16/6/14

Thomas, T. J. and Nair, S., 1983.Elasto-plastic stress analysis and fatigue prediction of a car wheel under mechanical and cyclic thermal loads.*Computers and structures* 17(3), 313-320.

Tonuk, E and Samim, Y., 2001. Pediction of automobile tyre cornering force characteristics by finite element modeling analysis.*Computers* 1219-1232.

Topac, M. M.. Eran, S. and Kuralay, N. S., 2012. Fatigue life prediction of a heavy vehicle steel wheel under radial loads by using finite element analysis.*Engineering failure analysis*, 20, 67-79.

Torgal, S. and Mishra, S., 2012. Stress Analysis of Wheel Rim. *International Journal of Mechanical Engineering and Research*, l(1)1, 34 - 37.

Tsang.N., 1989.Finite element simulation of the tyre rim interface.*Tyre Science and Technology* 17(2), 310-325.

Tyre Markings. http://www.tyresizesca lculator.com 06/03/2015, 1:28 am

Vijay.S and Mouli, A, C., 2015.Static and Fatigue Analysis of Aluminium Alloy Wheel.Proceedings of International Conference on Recent *Trends in Mechanical Engineering. South Asian Journal of Engineering and Technology*, 2(1)

Wang, N., Li, Y., Du, L., Wu, D. and Liu, X., 2009.*Fatigue property of low cost and high strength wheel steel for commercial vehicle.*International Journal of Iron and Steel Research, 16 (4) 44-48

Wimmer, A and Petersen, J., 1979. Road Stress Resistance and Lightweight Construction of Automobile Road Wheels," *SAE Technical Paper Series*, 79071.

Wood, G, Bllundell, M and Sharma, S., 2011. A low parameter tyre model for aircraft ground dynamic simulation. *Materials and design* xxx, xxx-xxx.

Woods, R., 1988. *Finite Element Analysis Case Study: Wheel Optimization," University of Dayton.*1-20.

Wright, D. H., 1999. Testing automotive materials and components. Warrendale: *SAE Publication.*

Wright, D., 1983. Test methods for automobile wheel. *I. Mech. E. Publications. Conference,* 0375.

Wubin, X., Peter, J. O., Bing, L. and Jian, L., 2011. *Shanping. Simplified stress analysis of large – scale harbour machine's wheel*, http//resourse.metapress.com.

www.//en.m.wilkipeadia.org, 2017, *Curb Weight (Total Weight of A Vehicle),* 11/03/2017 4:14 AM

www.dictionary.com

www.gov.uk/vehicle (2017) *Vehicle Weights Explained*. 25/02/17.

www.measurementsgroup.com., 2000. *Strain Gage Rosettes Selection, Application & Data Selection*, 1-20.

www.santaanawheel.com. 15/10/2016

www.tyresizescalculator.com, 6/05/2015

Xiaofeng, W. and Xiaoge, Z., 2010.Simulation of dynamic cornering fatigue test of a steelpassenger car wheel.*International journal of fatigue*, 32, 44-422.

Yang, M. L., Zhao, L. L., Zhang, Q. Q. and, Zhou, T. T. (2013). Numerical Simulation Analysis of Aluminium Alloy Wheels Casting Defects and Casting Process Optimization. *Materials Science Forum*, 749, 125-132.

Yi, J. Z.,.Gao, Y. X, Lee, P. D., Flower, H. M. and Lindley, T. C., 2003. *Metal material Transaction*., 34A 1878-1890.

Zang, B., Maijer, D. M. AND Cockcroft, S. L., 2007.*Material Science. Eng*. A 10(10-16), 2-18, in press.

Zienkiewicz, O. C., 1977.*The Finite Elemnt Method*, 3rd ed., McGraw-Hill, New York.

APPENDIX A

Table A1: Experimental Strain Values at 4750 N Radial Loadand0.3 MPa Inflation pressure

ROSETTE NO.	GUAGE READINGS G1 ε_1 (mm/mm)	G2 ε_2 (mm/mm)	G3 ε_3 (mm/mm)	ANGLE (deg)	WHEEL LOCATION
R1	0.000170	0.000090	0.000110	0	INBOARD
R2	0.000050	0.000090	0.000100	0	WELL
R3	0.000180	0.000140	0.000060	0	OUTBOARD
R4	'0.000050	0.000130	0.000130	30	INBOARD
R5	0.000190	0.000010	0.000060	30	WELL
R6	0.000090	0.000070	0.000070	30	OUTBOARD
R7	0.000050	0.000090	0.000100	60	INBOARD
R8	0.000010	0.000177	'0.000010	60	WELL
R9	0.000060	0.000030	0.000030	60	OUTBOARD
R10	0.000064	0.000042	0.000020	90	INBOARD
R11	0.000028	0.000090	0.000064	90	WELL
R12	0,000080	0.000080	0.000090	90	OUTBOARD
R13	0.000100	0.000120	0.000010	120	INBOARD
R14	0.000140	0.000100	0.000150	120	WELL
R15	0.000190	0.000010	0.000060	120	OUTBOARD
R16	0.000200	0.000140	0.000140	150	INBOARD
R17	0,000080	0.000080	0.000090	150	WELL
R18	0.000060	0.000030	0.000030	150	OUTBOARD
R19	0.000130	0.000120	0.000120	180	INBOARD

R20	0.000100	0.000120	0.000010	180	WELL
R21	0.000072	0.000112	0.000076	180	OUTBOARD

Table A2: Experimental Strain Values At 4750 N Radial Load and0.15 MPa Inflation Pressure

ROSETTE NO.	GUAGE READINGS G1 ε_1 (mm/mm)	G2 ε_2 (mm/mm)	G3 ε_3 (mm/mm)	ANGLE (deg)	WHEEL LOCATION
R1	0.000154	0.000050	0.000050	0	INBOARD
R2	0.000018	'0.000050	0.000050	0	WELL
R3	0.000154	0.000030	0.000034	0	OUTBOARD
R4	0.000016	0.000076	0.000076	30	INBOARD
R5	'0.000050	0.000130	0.000130	30	WELL
R6	0.000016	0.000076	0.000076	30	OUTBOARD
R7	0.000062	0.000046	0.000042	60	INBOARD
R8	0.000130	0.000120	0.000120	60	WELL
R9	0.000060	0.000030	0.000030	60	OUTBOARD
R10	0.000028	0.000032	0.000056	90	INBOARD
R11	0.000072	0.000112	0.000076	90	WELL
R12	0.000046	0.000064	0.000082	90	OUTBOARD
R13	0.000010	0.00092	'0.000040	120	INBOARD
R14	0.000126	0.000096	0.000126	120	WELL
R15	0.000010	0.000177	'0.000010	120	OUTBOARD
R16	0.000072	0.000112	0.000076	150	INBOARD

R17	0.000010	0.000177	'0.000010	150	WELL
R18	0.000060	0.000030	0.000030	150	OUTBOARD
R19	0.000010	0.000177	'0.000010	180	INBOARD
R20	0.000060	0.000030	0.000030	180	WELL
R21	0.000064	0.000042	0.000020	180	OUTBOARD

Table A3: Experimental Maximum Principal Strain Values at 4750N Radial Loadand0.3 MPa

ROSETTE NO.	MAX. PRIN. STRAIN ε_{pmax} (mm/mm)	ANGLE (deg)	WHEEL LOCATION
R1	18.47214E-05	0	INBOARD
R2	11.10555E-05	0	WELL
R3	22.19804E-05	0	OUTBOARD
R4	13.50000E-05	30	INBOARD
R5	1.140064E-05	30	WELL
R6	9.414213E-05	30	OUTBOARD
R7	11.10555E-05	60	INBOARD
R8	8..566042E-05	60	WELL
R9	6.621320E-05	60	OUTBOARD
R10	7.678505E-05	90	INBOARD
R11	21.10634E-05	90	WELL
R12	9.500000E-05	90	OUTBOARD
R13	15.54988E-05	120	INBOARD
R14	18.10555E-05	120	WELL
R15	1.140064E-05	120	OUTBOARD
R16	21.24264E-05	150	INBOARD
R17	9.500000E-05	150	WELL

R18	11.52884E-05	150	OUTBOARD
R19	13.20711E-05	180	INBOARD
R20	15.54988E-05	180	WELL
R21	9.961249E-05	180	OUTBOARD

Table A4: Experimental Maximum Principal Strain Values at 4750 N Radial Load and0.15MPa Inflation Pressure

ROSETTE NO.	MAX. PRIN. STRAIN ε_{pmax} (mm/mm)	ANGLE (deg)	WHEEL LOCATION
R1	17.55391E-05	0	INBOARD
R2	4.34558E-05	0	WELL
R3	16.89714E-5	0	OUTBOARD
R4	8.842640E-05	30	INBOARD
R5	13.50000E-05	30	WELL
R6	8.842640E-05	30	OUTBOARD
R7	6.629113E-05	60	INBOARD
R8	13.20711E-05	60	WELL
R9	1.140064E-05	60	OUTBOARD
R10	6.087681E-05	90	INBOARD
R11	9.961249E-05	90	WELL
R12	9.246050E-05	90	OUTBOARD
R13	1.516228E-05	120	INBOARD
R14	14.72132E-05	120	WELL
R15	14.96657E-05	120	OUTBOARD
R16	9.961249E-05	150	INBOARD
R17	8.831300E-05	150	WELL
R18	8..566042E-05	150	OUTBOARD
R19	14.96657E-05	180	INBOARD
R20	8..566042E-05	180	WELL
R21	7.678505E-05	180	OUTBOARD

Table A5: Experimental Maximum Principal Stress Values at 4750 N Radial Load and0.3 MPa Inflation Pressure

ROSETTE NO.	MAX. PRIN. STRESS σ_{pmax} (N/m^2)	ANGLE (deg)	WHEEL LOCATION
R1	6.082344E+06	0	INBOARD
R2	3.448298E+06	0	WELL
R3	6.212529E+06	0	OUTBOARD
R4	4.051497E+06	30	INBOARD
R5	2.260729E+06	30	WELL
R6	'3.296474E+06	30	OUTBOARD
R7	3.448298E+06	60	INBOARD
R8	1.571966E+06	60	WELL
R9	2.062338E+06	60	OUTBOARD
R10	2.260729E+06	90	INBOARD
R11	6.495840E+06	90	WELL
R12	3.423610E+06	90	OUTBOARD
R13	3.691254E+06	120	INBOARD
R14	6.138470E+06	120	WELL
R15	2.260729E+06	120	OUTBOARD
R16	7.199251E+06	150	INBOARD
R17	3.423610E+06	150	WELL
R18	3.560210E+06	150	OUTBOARD
R19	4.914875E+06	180	INBOARD
R20	3.691254E+06	180	WELL
R21	3.245941E+06	180	OUTBOARD

Table A6: Experimental Maximum Principal Stress Values at 4750N Radial Load and0.15 MPa Inflation Pressure

ROSETTE NO.	MAX. PRIN. STRESS σ_{pmax} (N/m^2)	ANGLE (deg)	WHEEL LOCATION
R1	5.074323E+06	0	INBOARD
R2	1.091344E+06	0	WELL
R3	4.311946E+06	0	OUTBOARD
R4	4.051497E+06	30	INBOARD
R5	4.176263E+06	30	WELL
R6	2.433803E+06	30	OUTBOARD
R7	1.554899E+06	60	INBOARD
R8	4.914875E+06	60	WELL
R9	2.260729E+06	60	OUTBOARD
R10	2.023436E+06	90	INBOARD
R11	3.245941E+06	90	WELL
R12	2.906336E+06	90	OUTBOARD
R13	.510814E+06	120	INBOARD
R14	5.175298E+06	120	WELL
R15	4.395377E+06	120	OUTBOARD
R16	3.245941E+06	150	INBOARD
R17	1.571966E+06	150	WELL
R18	2.062338E+06	150	OUTBOARD
R19	4.395377E+06	180	INBOARD
R20	2.062338E+06	180	WELL
R21	4.395377E+06	180	OUTBOARD

Table A7: Experimental Von - Mises stress values at 4750N Radial Loadand0.3 MPa Inflation Pressure

ROSETTE NO.	VON-MISES STRESS σ_{pmax} (N/m^2)	ANGLE (deg)	WHEEL LOCATION
R1	8.601733E+06	0	INBOARD
R2	4.876629E+06	0	WELL
R3	8.785843E+06	0	OUTBOARD
R4	5.729682E+06	30	INBOARD
R5	8.980077E+06	30	WELL
R6	4.602993E+06	30	OUTBOARD
R7	4.876629E+06	60	INBOARD
R8	2.223096E+06	60	WELL
R9	2.916652E+06	60	OUTBOARD
R10	3.197154E+06	90	INBOARD
R11	9.186504E+06	90	WELL
R12	4.8417166E+06	90	OUTBOARD
R13	5.220222E+06	120	INBOARD
R14	8.681107E+06	120	WELL
R15	5.220222E+06	120	OUTBOARD
R16	10.18128E+06	150	INBOARD
R17	4.8417166E+06	150	WELL
R18	3.054886E+06	150	OUTBOARD
R19	6.9506837E+06	180	INBOARD
R20	5.220222E+06	180	WELL
R21	4.590453E+06	180	OUTBOARD

Table A8: Experimental Von - Mises Stress Values at 4750N Radial Load and0.15 MPa Inflation Pressure

ROSETTE NO.	VON-MISES STRESS σ_{pmax} (N/m^2)	ANGLE (deg)	WHEEL LOCATION
R1	7.176176E+06	0	INBOARD
R2	1.543393E+06	0	WELL
R3	6.098012E+06	0	OUTBOARD
R4	3.0548864E+06	30	INBOARD
R5	5.729682E+06	30	WELL
R6	3.054886E+06	30	OUTBOARD
R7	3.149866E+06	60	INBOARD
R8	6.950683E+06	60	WELL
R9	3.197154E+06	60	OUTBOARD
R10	2.861571E+06	90	INBOARD
R11	4.590453E+06	90	WELL
R12	4.110180E+06	90	OUTBOARD
R13	1.919932E+06	120	INBOARD
R14	7.318976E+06	120	WELL
R15	6.216002E+06	120	OUTBOARD
R16	4.590453E+06	150	INBOARD
R17	2.223096E+06	150	WELL
R18	2.916652E+06	150	OUTBOARD
R19	6.216002E+06	180	INBOARD
R20	2.916652E+06	180	WELL
R21	6.216002E+06	180	OUTBOARD

TableA9 : Experimental Strain Values at 3570 N Radial Load and 0.3 MPa Inflation Pressure

ROSETTE NO.	GUAGE READINGS G1 ε1 (mm/mm)	G2 ε2 (mm/mm)	G3 ε3 (mm/mm)	ANGLE (deg)	WHEEL LOCATION
R1	0.000120	0.000042	0.000042	0	INBOARD
R2	0.000022	0.000020	0.000024	0	WELL
R3	0.000102	0.000056	0.000063	0	OUTBOARD
R4	0.000008	0.000036	0.000036	30	INBOARD
R5	0.000008	0.000036	0.000036	30	WELL
R6	0.000050	0.000010	0.000022	30	OUTBOARD
R7	0.000036	0.000042	0.000084	60	INBOARD
R8	0.000070	0.000056	0.000118	60	WELL
R9	0.000014	0.000035	0.000014	60	OUTBOARD
R10	0.000014	0.000028	0.000022	90	INBOARD
R11	0.000070	0.000042	0.000050	90	WELL
R12	0.000105	0.000014	0.000008	90	OUTBOARD
R13	0.000014	0.000050	0.000008	120	INBOARD
R14	0.000014	0.000035	0.000014	120	WELL
R15	0.000048	0.000050	0.000036	120	OUTBOARD
R16	0.000028	0.000064	0.000035	150	INBOARD
R17	0.000045	0.000010	0.000028	150	WELL
R18	0.000014	0.000028	0.000022	150	OUTBOARD
R19	0.000080	0.000042	0.000050	180	INBOARD
R20	0.000102	0.000056	0.000063	180	WELL
R21	0.000028	0.000022	0.000008	180	OUTBOARD

TableA10 : Experimental Strain Values At 3570 N and 0.150 MPa Inflation Pressure

ROSETTE NO.	GUAGE READINGS G1 ε_1 (mm/mm)	G2 ε_2 (mm/mm)	G3 ε_3 (mm/mm)	ANGLE (deg)	WHEEL LOCATION
R1	0.000060	0.000022	0.000022	0	INBOARD
R2	0.000028	0.000022	0.000018	0	WELL
R3	0.000096	0.000036	0.000042	0	OUTBOARD
R4	0.000010	0.000030	0.000032	30	INBOARD
R5	0.000032	0.000032	'0.000046	30	WELL
R6	0.000046	0.000022	0.000022	30	OUTBOARD
R7	0.000028	0.000032	0.000056	60	INBOARD
R8	0.000046	0.000036	0.000096	60	WELL
R9	0.000062	0.000046	0.000042	60	OUTBOARD
R10	0.000010	0.000012	0.000014	90	INBOARD
R11	0.000062	0.000046	0.000042	90	WELL
R12	0.000018	0.000032	0.000010	90	OUTBOARD
R13	0.000018	0.000032	0.000010	120	INBOARD
R14	0.000012	0.000020	0.000012	120	WELL
R15	0.000010	0.000012	0.000014	120	OUTBOARD
R16	0.000018	0.000042	0.000040	150	INBOARD
R17	0.000070	0.000042	0.000050	150	WELL
R18	0.000028	0.000064	0.000035	150	OUTBOARD
R19	0.000052	0.000054	0.000032	180	INBOARD
R20	0.000032	0.000010	0.000032	180	WELL
R21	0.000018	0.000032	0.000010	180	OUTBOARD

Table A11: Experimental Maximum Principal Strain Values at 3570 N Radial Load and 0.3 MPa Inflation Pressure

ROSETTE NO.	MAX. PRIN. STRAIN ε_{pmax} (mm/mm)	ANGLE (deg)	WHEEL LOCATION
R1	13.61543E-05	0	INBOARD
R2	2.616228E-05	0	WELL
R3	11.05179E-05	0	OUTBOARD
R4	4.179899E-05	30	INBOARD
R5	4.179899E-05	30	WELL
R6	5.754066E-05	30	OUTBOARD
R7	10.50999E-05	60	INBOARD
R8	14.94437E-05	60	WELL
R9	2.884924E-05	60	OUTBOARD
R10	2.507107E-05	90	INBOARD
R11	7.523155E-05	90	WELL
R12	3.526268E-05	90	OUTBOARD
R13	4.100000E-05	120	INBOARD
R14	2.884924E-05	120	WELL
R15	5.513840E-05	120	OUTBOARD
R16	5.259502E-05	150	INBOARD
R17	5.400714E-05	150	WELL
R18	2.507107E-05	150	OUTBOARD
R19	8.695450E-05	180	INBOARD
R20	11.05179E-05	180	WELL
R21	3.526268E-05	180	OUTBOARD

Table A12: Experimental Maximum Principal Strain Values at 3570 N Radial Load and0.15 MPa Inflation Pressure

ROSETTE NO.	MAX. PRIN. STRAIN ε_{pmax} (mm/mm)	ANGLE (deg)	WHEEL LOCATION
R1	6.7870005E-05	0	INBOARD
R2	3.061577E-06	0	WELL
R3	10.74107E-06	0	OUTBOARD
R4	3.662050E-05	30	INBOARD
R5	4.700000E-5	30	WELL
R6	5.097056E-05	30	OUTBOARD
R7	6.807681E-05	60	INBOARD
R8	6.629113E-05	60	WELL
R9	12.41214E-05	60	OUTBOARD
R10	1.516228E-05	90	INBOARD
R11	6.629113E-05	90	WELL
R12	3.055295E-05	90	OUTBOARD
R13	3.055295E-05	120	INBOARD
R14	1.765685E-05	120	WELL
R15	1.516228E-05	120	OUTBOARD
R16	4.462050E-05	150	INBOARD
R17	7.523155E-05	150	WELL
R18	5.400714E-05	150	OUTBOARD
R19	6.302379E-05	180	INBOARD
R20	5.259502E-05	180	WELL
R21	3.055295E-05	180	OUTBOARD

Table A13: Experimental Maximum Principal Stress Values at 3570 N Radial Load and 0.3 MPa Inflation Pressure

ROSETTE NO.	MAX. PRIN. STRESS σ_{pmax} (N/m^2)	ANGLE (deg)	WHEEL LOCATION
R1	3.250354E+06	0	INBOARD
R2	0.933553E+06	0	WELL
R3	3.610362E+06	0	OUTBOARD
R4	1.156271E+06	30	INBOARD
R5	1.818770E+06	30	WELL
R6	1.7216456E+06	30	OUTBOARD
R7	3.013803E+06	60	INBOARD
R8	4.482827E+06	60	WELL
R9	0.771126E+06	60	OUTBOARD
R10	1.092893E+06	90	INBOARD
R11	2.53804E+06	90	WELL
R12	0.962734E+06	90	OUTBOARD
R13	0.873657E+06	120	INBOARD
R14	0.771126E+06	120	WELL
R15	1.818770E+06	120	OUTBOARD
R16	1.541710E+06	150	INBOARD
R17	2.544955E+06	150	WELL
R18	1.092893E+06	150	OUTBOARD
R19	2.842464E+06	180	INBOARD
R20	2.3988346E+06	180	WELL
R21	0.962734E+06	180	OUTBOARD

Table A14: Experimental Maximum Principal Stress Values at 3570N Radial Load and0.15 MPa Inflation Pressure

ROSETTE NO.	MAX. PRIN. STRESS σ_{pmax} (N/m^2)	ANGLE (deg)	WHEEL LOCATION
R1	1.997457E+06	0	INBOARD
R2	1.003460E+06	0	WELL
R3	3.254808E+06	0	OUTBOARD
R4	1.052250E+06	30	INBOARD
R5	1.052250E+06	30	WELL
R6	1.573045E+06	30	OUTBOARD
R7	2.023436E+06	60	INBOARD
R8	3.595509E+06	60	WELL
R9	2.227291E+06	60	OUTBOARD
R10	0.510811E+06	90	INBOARD
R11	1.554899E+06	90	WELL
R12	0.797869E+06	90	OUTBOARD
R13	0.797869E+06	120	INBOARD
R14	0.549969E+06	120	WELL
R15	0.510811E+06	120	OUTBOARD
R16	1.359698E+06	150	INBOARD
R17	2.53804E+06	150	WELL
R18	1.677546E+06	150	OUTBOARD
R19	1.944118E+06	180	INBOARD
R20	1.541710E+06	180	WELL
R21	0.797869E+06	180	OUTBOARD

Table A15: Experimental Von - Mises stress values at 3570N Radial Load and 0.3 MPa Inflation Pressure

ROSETTE NO.	VON-MISES STRESS σ_{pmax} (N/m^2)	ANGLE (deg)	WHEEL LOCATION
R1	5.626705E+06	0	INBOARD
R2	1.320243E+06	0	WELL
R3	5.105823E+06	0	OUTBOARD
R4	1.635214E+06	30	INBOARD
R5	1.635214E+06	30	WELL
R6	2.434774E+06	30	OUTBOARD
R7	4.262162E+06	60	INBOARD
R8	6.339675E+06	60	WELL
R9	1.090537E+06	60	OUTBOARD
R10	1.135266E+06	90	INBOARD
R11	3.599109E+06	90	WELL
R12	4.596695E+06	90	OUTBOARD
R13	1.263822E+06	120	INBOARD
R14	1.090537E+06	120	WELL
R15	2.572179E+06	120	OUTBOARD
R16	2.180307E+06	150	INBOARD
R17	2.372408E+06	150	WELL
R18	1.135266E+06	150	OUTBOARD
R19	4.020102E+06	180	INBOARD
R20	5.105823E+06	180	WELL
R21	1.361512E+06	180	OUTBOARD

Table A16: Experimental Von - Mises Stress Values at 3570N Radial Load and0.15 MPa Inflation Pressure

ROSETTE NO.	VON-MISES STRESS σ_{pmax} (N/m^2)	ANGLE (deg)	WHEEL LOCATION
R1	2.824830E+06	0	INBOARD
R2	1.419107E+06	0	WELL
R3	4.602993E+06	0	OUTBOARD
R4	1.488102E+06	30	INBOARD
R5	2.232930E+06	30	WELL
R6	2.224622E+06	30	OUTBOARD
R7	2.861571E+06	60	INBOARD
R8	5.084817E+06	60	WELL
R9	3.149866E+06	60	OUTBOARD
R10	0.722396E+06	90	INBOARD
R11	3.149866E+06	90	WELL
R12	1.128357E+06	90	OUTBOARD
R13	1.128357E+06	120	INBOARD
R14	0.722396E+06	120	WELL
R15	1.919932E+06	120	OUTBOARD
R16	1.922903E+06	150	INBOARD
R17	3.599109E+06	150	WELL
R18	2.372408E+06	150	OUTBOARD
R19	2.749398E+06	180	INBOARD
R20	2.180307E+06	180	WELL
R21	1.128357E+06	180	OUTBOARD

APPENDIX
COMPUTER PROGRAMME TO EVALUE MAXIMUM PRICIPAL STRAINS AND STRESSES

```
!    PROGRAMME TO COMPUTE PRINCIPA STRAINS,
!    STRESSES AND VON - MISES STRESSES
WRITE(*,*) ' YOUNG'S MODULUS, E'
READ(*,*) E
WRITE(*,*) 'MESURED STRAIN, E1'
READ(*,*) E1
WRITE(*,*) 'MESURED STRAIN, E2'
READ(*,*) E2
WRITE(*,*) 'MESURED STRAIN, E3'
READ(*,*) E3
WRITE(*,*) 'POISON'S RATIO'
READ(*,*) V
    A=(E1+E3)/2.0
    B=1.0/SQRT(2.0)
    C=SQRT((E1-E3)**2+(E2-E3)**2)
    EP=A+(B*C)
    EQ=A-(B*C)
    D=E/(1.0-V**2)
    F=EP+V*EQ
    G=EQ+V*EP
    GP=D*F
    GQ=D*G
    STR=SQRT(((GP-GQ)**2) +GP**2+GQ**2)*.5)
WRITE(*,*)'EP=',EP
WRITE(*,*)'EQ=',EQ
WRITE(*,*)'GP=',GP
WRITE(*,*)'GQ=',GQ
WRITE(*,*)'STR=',VMS
    END
```

APPANDIX C

STRAIN GAUGE LOCATIONS AND PLACEMENT

PlateC1: Wheel-tyre assembly in the test rig showing attached strain rosette at the outside surface of the rim: Inboard view

Plate C2: Wheel-tyre assembly in the test rig showing attached strain rosette at the outside surface of the rim: Outboard view.

PlateC3: Wheel-tyre assembly in the test rig with lead wires.

PlateC4: Wheel-tyre assembly in the test rig showing the instrument (strain measuring device) connection to the lead wires of the strain rosette.

PlateC5: Tools and apparatus used for the gauge assembly and testing

APPENDIX D

Table D1: ANOVA: Two-Factor Without Replication: Maximum Principal Strain Results at the Inboard Bead Seat: Experimental versus FE at 4750 N Radial Load and 0.3 MPa Inflation Pressure

Source of Variation	*SS*	*df*	*MS*	*F*	*P-value*	*F crit*
Rows	1.63E-06	6	2.72E-08	3.983204	0.010354	2.661305

	4.79E-08					
Columns		3	1.6E-08	2.341498	0.107443	3.159908
	1.23E-07		6.83E-09			
Error		18				

Table D2*:*ANOVA: Two-Factor Without Replication:Maximum Principal Strain Results at the Inboard Bead Seat: Experimental versusFEA at 4750 N Radial Load and 0.15 MPa Inflation Pressure.

Source of Variation	*SS*	*Df*	*MS*	*F*	*P-value*	*F crit*
	1.23E-07		2.05E-08			
Rows		6		4.101067	0.009092	2.661305
	3.25E-08		1.08E-08			
Columns		3		2.173412	0.126527	3.159908
Error	8.98E-	18	4.99E-			

	0					
	9					

Table D3: ANOVA: Two-Factor Without Replication: Maximum Principal Strain Results at the Inboard Bead Seat: Experimental versusFEA at 3570 N Radial Load and 0.3 MPa Inflation Pressure.

Source of Variation	*SS*	*Df*	*MS*	*F*	*P-value*	*F crit*
	1.18E-0		1.96E-0			
Rows		6	8	3.823338	0.012384	2.661305
	4.17E-0		1.39E-0			
Columns	8	3	8	2.707037	0.075858	3.159908
	9.23E-0		5.13E-0			
Error	8	18	9			

	2.52E-0					
Total		27				

Table D4: ANOVA: Two-Factor Without Replication: Maximum Principal Strain Results at the Inboard Bead Seat: Experimental versusFEA at 3570 N Radial Load and 0.15 MPa Inflation Pressure.

Source of Variation	*SS*	*Df*	*MS*	*F*	*P-value*	*F crit*
	8.27E-0		1.38E-0			
Rows	8	6	8	5.707515	0.001794	2.661305
	3.54E-0		1.18E-0			
Columns	8	3	8	4.890984	0.011684	3.159908
	4.34E-0		2.41E-0			
Error	8	18	9			

	1.62E-					
	(					
Total		27				

Table D5: ANOVA: Two-Factor Without Replication: Maximum Principal Stress Results at the Inboard Bead Seat: Experimental versus FE at 4750 N Radial Load and 0.3 MPa Inflation Pressure.

Source of Variation	*SS*	*Df*	*MS*	*F*	*P-value*	*F crit*
Rows	39.55469	6	6.592448	4.942029	0.003762	2.661305
Columns	20.2694	3	6.756467	5.064986	0.010209	3.159908
Error	24.0112	18	1.333956			
Total	83.83529	27				

Table D6: ANOVA: Two-Factor Without Replication: Maximum Principal Stress Results at the Inboard Bead Seat: Experimental versusFEA at 4750 N Radial Load and 0.15 MPa Inflation Pressure.

Source of Variation	*SS*	*Df*	*MS*	*F*	*P-value*	*F crit*
Rows	37.59989	6	6.266649	5.153482	0.003049	2.661305
Columns	14.21533	3	4.738442	3.896736	0.026238	3.159908
Error	21.88805	18	1.216003			
Total	73.70327	27				

Table. D7: ANOVA: Two-Factor Without Replication: Maximum Principal Stress Results at the Inboard Bead Seat: Experimental versusFEA at 3570 N Radial Load and 0.3 MPa Inflation Pressure.

Source of Variation	*SS*	*Df*	*MS*	*F*	*P-value*	*F crit*
Rows	18.0783	6	3.013051	3.302902	0.02266	2.661305
Columns	3.613754	3	1.204585	1.320464	0.298639	3.159908
Error	16.42038	18	0.912243			
Total	38.11244	27				

Table D8: ANOVA: Two-Factor Without Replication: Maximum Principal Stress Results at the Inboard Bead Seat: Experimental versusFEA at 3570 N Radial Load and 0.15 MPa Inflation Pressure.

Source of Variation	*SS*	*Df*	*MS*	*F*	*P-value*	*F crit*
Rows	37.59989	6	6.266649	5.153482	0.003049	2.661305
Columns	14.21533	3	4.738442	3.896736	0.026238	3.159908
Error	21.88805	18	1.216003			
Total	73.70327	27				

Table D9: ANOVA: Two-Factor Without Replication: Von Mises Stress Results at the Inboard Bead Seat: Experimental versusFEA at 4750 N Radial Load and 0.3 MPa Inflation Pressure

Source of Variation	*SS*	*Df*	*MS*	*F*	*P-value*	*F crit*
Rows	104.5768	5	20.91535	7.850164	0.000831	2.901295
Columns	12.26031	3	4.086771	1.533888	0.246669	3.287382
Error	39.96481	15	2.664321			
Total	156.8019	23				

Table D10: ANOVA: Two-Factor Without Replication:Von Mises Stress Results at the Inboard Bead Seat: Experimental versusFEA at 4750 N Radial Load and 0.15 MPa Inflation Pressure.

Source of Variation	*SS*	*df*	*MS*	*F*	*P-value*	*F crit*
Rows	80.11252	6	13.35209	4.307443	0.007269	2.661305
Columns	16.24737	3	5.41579	1.747158	0.193291	3.159908
Error	55.79588	18	3.099771			
Total	152.1558	27				

Table.D11: ANOVA: Two-Factor Without Replication:Von Mises Stress Results at the Inboard Bead Seat: Experimental versusFEA at 3570 N Radial Load and 0.3 MPa Inflation Pressure

Source of Variation	*SS*	*df*	*MS*	*F*	*P-value*	*F crit*
Rows	67.49511	6	11.24918	7.333446	0.00044	2.661305
Columns	12.36449	3	4.121498	2.686842	0.07731	3.159908
Error	27.61121	18	1.533956			
Total	107.4708	27				

Table D12:ANOVA: Two-Factor Without Replication*:*Von Mises Stress Results at the Inboard Bead Seat: Experimental versusFEA at 3570 N Radial Load and 0.15 MPa Inflation Pressure.

Source of Variation	*SS*	*df*	*MS*	*F*	*P-value*	*F crit*
Rows	27.36064	6	4.560107	5.181661	0.002965	2.661305
Columns	8.849261	3	2.949754	3.351812	0.042105	3.159908
Error	15.84085	18	0.880047			
Total	52.05075	27				

Table D13: ANOVA: Two-Factor Without Replication:Maximum Principal Strain Results at the Well : Experimental versus FEA at 4750 N Radial Load and 0.3 MPa Inflation Pressure.

Source of Variation	*SS*	*df*	*MS*	*F*	*P-value*	*F crit*
Rows	3.46E-08	6	5.76E-09	2.394757	0.070499	2.661305
Columns	2.95E-08	3	9.83E-09	4.082929	0.022433	3.159908
Error	4.33E-08	18	2.41E-09			
Total	1.07E-07	27				

Table D14:**ANOVA*:* Two-Factor Without Replication*:*Maximum Principal Strain Results at the Well : Experimental versus FEA at 4750 N Radial Load and 0.15 MPa Inflation Pressure**.**

Source of Variation	*SS*	*df*	*MS*	*F*	*P-value*	*F crit*
Rows	1.95E-08	6	3.25E-09	1.854821	0.144612	2.661305
Columns	1.27E-08	3	4.24E-09	2.421258	0.099497	3.159908
Error	3.16E-08	18	1.75E-09			
Total	6.38E-08	27				

Table D15: ANOVA: Two-Factor Without Replication: Maximum Principal Strain Results at the Well: Experimental versusFEA at 3570 N Radial Load and 0.3 MPa Inflation Pressure

Source of Variation	*SS*	*df*	*MS*	*F*	*P-value*	*F crit*
Rows	3.73E-08	6	6.22E-09	5.075062	0.003294	2.661305
Columns	9.76E-09	3	3.25E-09	2.6533	0.079789	3.159908
Error	2.21E-08	18	1.23E-09			
Total	6.92E-08	27				

Table D16:ANOVA: Two-Factor Without Replication:**Maximum Principal Strain Results at the Well: Experimental versusFEA at 3570 N Radial Load and 0.15 MPa Inflation Pressure**

Source of Variation	*SS*	*df*	*MS*	*F*	*P-value*	*F crit*
Rows	1.93E-08	6	3.21E-09	3.143851	0.02744	2.661305
Columns	6.02E-09	3	2.01E-09	1.965121	0.155392	3.159908
Error	1.84E-08	18	1.02E-09			
Total	4.37E-08	27				

Table D17:**ANOVA: Two-Factor Without Replication**:**Maximum Principal Stress Results at the Well: Experimental versus FEA at 4750 N Radial Load and 0.3 MPa Inflation Pressure**.

Source of Variation	*SS*	*df*	*MS*	*F*	*P-value*	*F crit*
Rows	65.10817	6	10.85136	1.806495	0.154386	2.661305
Columns	35.03587	3	11.67862	1.944215	0.158657	3.159908
Error	108.1235	18	6.006859			
Total	208.2675	27				

Table 18: ANOVA: Two-Factor Without Replication:Maximum Principal Stress Results at the Well: Experimental versus FEA at 4750 N Radial Load and 0.15 MPa Inflation Pressure.

Source of Variation	*SS*	*df*	*MS*	*F*	*P-value*	*F crit*
Rows	44.49084	6	7.415139	2.136152	0.099129	2.661305
Columns	4.946171	3	1.648724	0.474964	0.703591	3.159908
Error	62.48268	18	3.47126			
Total	111.9197	27				

Table D19: ANOVA: Two-Factor Without Replication:Maximum Principal Stress Results at the Well: Experimental versus FEA at 3570 N Radial Load and 0.3 MPa Inflation Pressure.

Source of Variation	*SS*	*df*	*MS*	*F*	*P-value*	*F crit*
Rows	187.0988	6	31.18313	24.97743	8.42E-08	2.661305
Columns	8.800838	3	2.933613	2.3498	0.106585	3.159908
Error	22.47214	18	1.248452			
Total	218.3718	27				

Table D20: ANOVA: Two-Factor Without Replication:Maximum Principal Stress Results at the Well: Experimental versus FEA at 3570 N Radial Load and 0.15 MPa Inflation Pressure

Source of Variation	*SS*	*df*	*MS*	*F*	*P-value*	*F crit*
Rows	67.41482	6	11.2358	4.193119	0.008223	2.661305
Columns	2.920486	3	0.973495	0.363301	0.780269	3.159908
Error	48.23246	18	2.679581			
Total	118.5678	27				

Table D21:ANOVA: Two-Factor Without Replication: Von Mises Stress Results at the Well: Experimental versusFEA at 4750 N Radial Load and 0.3 MPa Inflation Pressure.

Source of Variation	*SS*	*df*	*MS*	*F*	*P-value*	*F crit*
Rows	72.6112	6	12.10187	3.661463	0.014891	2.661305
Columns	29.8019	3	9.933967	3.005557	0.05753	3.159908
Error	59.4936	18	3.3052			
Total	161.9067	27				

Table D22: ANOVA: Two-Factor Without Replication:Von Mises Stress Results at the Well: Experimental versus FEA at 4750 N Radial Load and 0.15 MPa Inflation Pressure.

Source of Variation	*SS*	*df*	*MS*	*F*	*P-value*	*F crit*
Rows	22.69852	6	3.783087	1.143659	0.377779	2.661305
Columns	1.698429	3	0.566143	0.17115	0.914481	3.159908
Error	59.54182	18	3.307879			
Total	83.93877	27				

Table D23: ANOVA: Two-Factor Without Replication:Von Mises Stress Results at the Wellt: Experimental versus FEA at 3570 n N Radial Load and 0.3 MPa Inflation Pressure.

Source of Variation	*SS*	*df*	*MS*	*F*	*P-value*	*F crit*
Rows	64.62239	6	10.7704	4.257929	0.007666	2.661305
Columns	0.858611	3	0.286204	0.113147	0.951276	3.159908
Error	45.53086	18	2.529492			
Total	111.0119	27				

Table D24:**ANOVA: Two-Factor Without Replication:Von Mises Stress Results at the Well: Experimental versusFEA at 3570 N Radial Load and 0.15 MPa Inflation Pressure**

Source of Variation	*SS*	*df*	*MS*	*F*	*P-value*	*F crit*
Rows	67.71544	6	11.28591	20.91117	3.33E-07	2.661305
Columns	2.207171	3	0.735724	1.363191	0.285808	3.159908
Error	9.714729	18	0.539707			
Total	79.63734	27				

Table D25:ANOVA: Two-Factor Without Replication*:* Maximum Principal Strain Results at the Outboard Bead Seat: Experimental versusFEA at 4750 N Radial Load and 0.3 MPa Inflation Pressure

Source of Variation	*SS*	*df*	*MS*	*F*	*P-value*	*F crit*
Rows	4.64E-09	6	7.73E-10	0.411315	0.861879	2.661305
Columns	6.6E-08	3	2.2E-08	11.72078	0.000172	3.159908
Error	3.38E-08	18	1.88E-09			
Total	1.04E-07	27				

Table D26:ANOVA: Two-Factor Without Replication: Maximum Principal Strain Results at the Outboard Bead Seat: Experimental versusFEA at 4750 N Radial Load and 0.15 MPa Inflation Pressure

Source of Variation	*SS*	*df*	*MS*	*F*	*P-value*	*F crit*
Rows	1.2E-08	6	1.99E-09	1.314064	0.301056	2.661305
Columns	4.3E-08	3	1.43E-08	9.449954	0.000571	3.159908
Error	2.73E-08	18	1.52E-09			
Total	8.23E-08	27				

Table D27: ANOVA: Two-Factor Without Replication: Maximum Principal Strain Results at the Outboard Bead Seat: Experimental versusFEA at 3570 N Radial Load and 0.3 MPa Inflation Pressure

Source of Variation	*SS*	*df*	*MS*	*F*	*P-value*	*F crit*
Rows	1.66E-08	6	2.76E-09	3.335051	0.021809	2.661305
Columns	2.05E-08	3	6.83E-09	8.248416	0.001156	3.159908
Error	1.49E-08	18	8.28E-10			
Total	5.19E-08	27				

Table D28: ANOVA: Two-Factor Without Replication:Maximum Principal Strain Results at the Outboard Bead Seat: Experimental versus FEA at 3570 N Radial Load and 0.15 MPa Inflation Pressure

Source of Variation	*SS*	*df*	*MS*	*F*	*P-value*	*F crit*
Rows	1.34E-09	6	2.24E-10	0.348884	0.901329	2.661305
Columns	1.23E-08	3	4.09E-09	6.364076	0.003944	3.159908
Error	1.16E-08	18	6.42E-10			
Total	2.52E-08	27				

Table D29: ANOVA: Two-Factor Without Replication: Maximum Principal Stress Results at the Outboard Bead Seat: Experimental versus FEA at 4750 N Radial Load and 0.3 MPa Inflation Pressure

Source of Variation	*SS*	*df*	*MS*	*F*	*P-value*	*F crit*
Rows	3.926248	6	0.654375	0.79603	0.585208	2.661305
Columns	104.5191	3	34.83969	42.38159	2.3E-08	3.159908
Error	14.79686	18	0.822048			
Total	123.2422	27				

Table D30:ANOVA: Two-FactorWithout Replication:Maximum Principal Stress Results at the Outboard Bead Seat: Experimental versus FEA at 4750 N Radial Load and 0.15 MPa Inflation Pressure

Source of Variation	*SS*	*df*	*MS*	*F*	*P-value*	*F crit*
Rows	2.1899	6	0.364983	0.662601	0.680567	2.661305
Columns	45.77984	3	15.25995	27.70334	5.8E-07	3.159908
Error	9.915014	18	0.550834			
Total	57.88475	27				

Table D31: ANOVA: Two-Factor Without Replication:Maximum Principal Stress Results at the Outboard Bead Seat: Experimental versus FEA at 3570 N Radial Load and 0.3 MPa Inflation Pressure

Source of Variation	*SS*	*df*	*MS*	*F*	*P-value*	*F crit*
Rows	1.566128	6	0.261021	0.549298	0.764228	2.661305
Columns	16.97109	3	5.657028	11.90475	0.000157	3.159908
Error	8.553435	18	0.475191			
Total	27.09065	27				

Table D32: ANOVA: Two-Factor Without Replication:Maximum Principal Stress Results at the Outboard Bead Seat: Experimental versus FEA at 3570 N Radial Load and 0.15 MPa Inflation Pressure.

Source of Variation	*SS*	*df*	*MS*	*F*	*P-value*	*F crit*
Rows	1.760786	6	0.293464	0.688	0.661991	2.661305
Columns	13.54378	3	4.514594	10.58405	0.000307	3.159908
Error	7.677843	18	0.426547			
Total	22.98241	27				

Table D33:ANOVA: Two-Factor Without Replication:Von Mises Stress Results at the Outboard Bead Seat: Experimental versusFEA at 4750 N Radial Load and 0.3 MPa Inflation Pressure.

Source of Variation	*SS*	*df*	*MS*	*F*	*P-value*	*F crit*
Rows	5.286393	6	0.881065	0.415971	0.858779	2.661305
Columns	158.1642	3	52.7214	24.89098	1.26E-06	3.159908
Error	38.12566	18	2.118092			
Total	201.5763	27				

Table D34:ANOVA: Two-Factor Without Replication:Von Mises Stress Results at the Outboard Bead Seat: Experimental versus FEA at 4750 N Radial Load and 0.15 MPa Inflation Pressure

Source of Variation	*SS*	*df*	*MS*	*F*	*P-value*	*F crit*
Rows	6.589236	6	1.098206	1.025129	0.440791	2.661305
Columns	77.17024	3	25.72341	24.01173	1.63E-06	3.159908
Error	19.28314	18	1.071285			
Total	103.0426	27				

Table D35:ANOVA: Two-Factor Without Replication:Von Mises Stress Results at the Outboard Bead Seat: Experimental versus FEA at 3570 N Radial Load and 0.3 MPa Inflation Pressure

Source of Variation	*SS*	*df*	*MS*	*F*	*P-value*	*F crit*
Rows	5.951685	6	0.991947	1.4546	0.248989	2.661305
Columns	29.31996	3	9.773321	14.33168	5.13E-05	3.159908
Error	12.27489	18	0.681938			
Total	47.54654	27				

Table D36: ANOVA: Two-Factor Without Replication: Von Mises Stress Results at the Outboard Bead Seat: Experimental versusFEA at 3570 N Radial Load and 0.15 MPa Inflation Pressure

Source of Variation	*SS*	*df*	*MS*	*F*	*P-value*	*F crit*
Rows	5.951685	6	0.991947	1.4546	0.248989	2.661305
Columns	29.31996	3	9.773321	14.33168	5.13E-05	3.159908
Error	12.27489	18	0.681938			
Total	47.54654	27				

APPENDIX E

DEFORMED WHEEL FRINGES

a 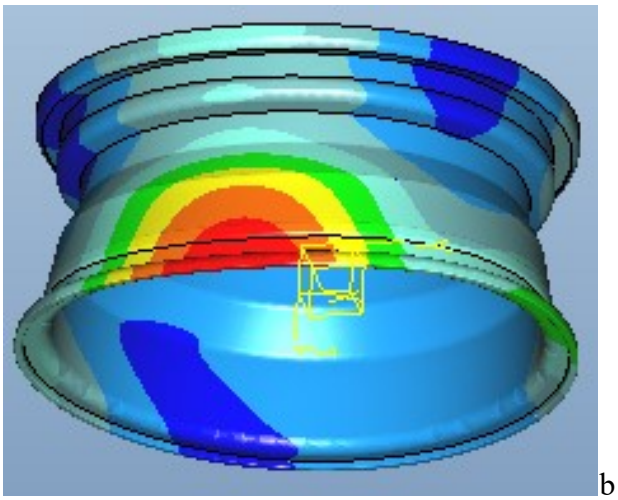 b 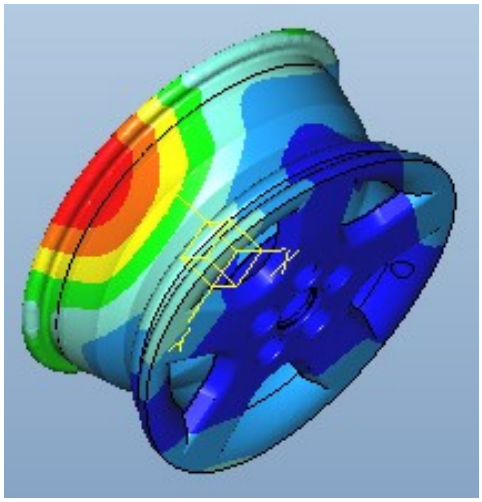

Fig.E1: Deformed: Wheel (a) Inboard side, (b) Outboard side

a 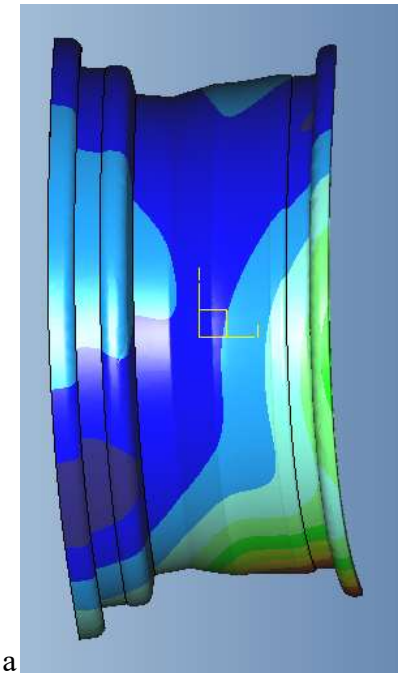 b 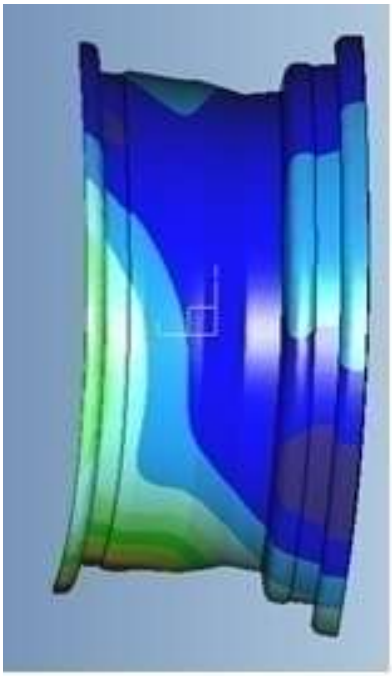

Fig.E2: Figure: Deformed: Wheel (a) left side, (b) right side

a 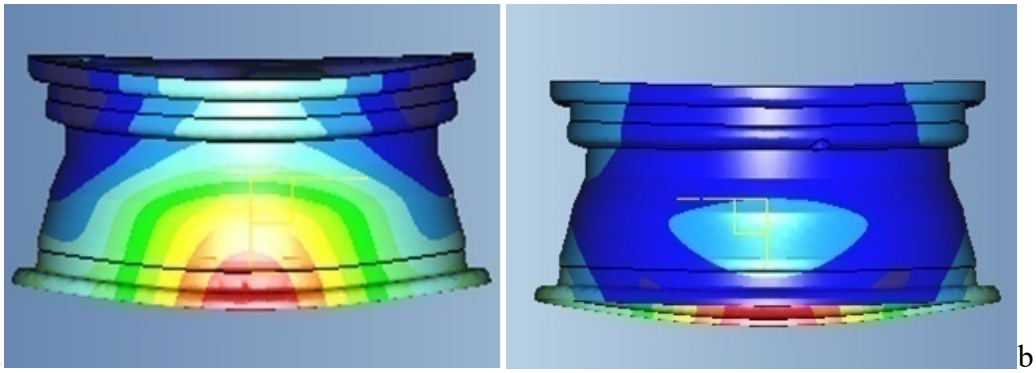 b

Fig.E3: Deformed: Wheel (a) Top, (b) Bottom

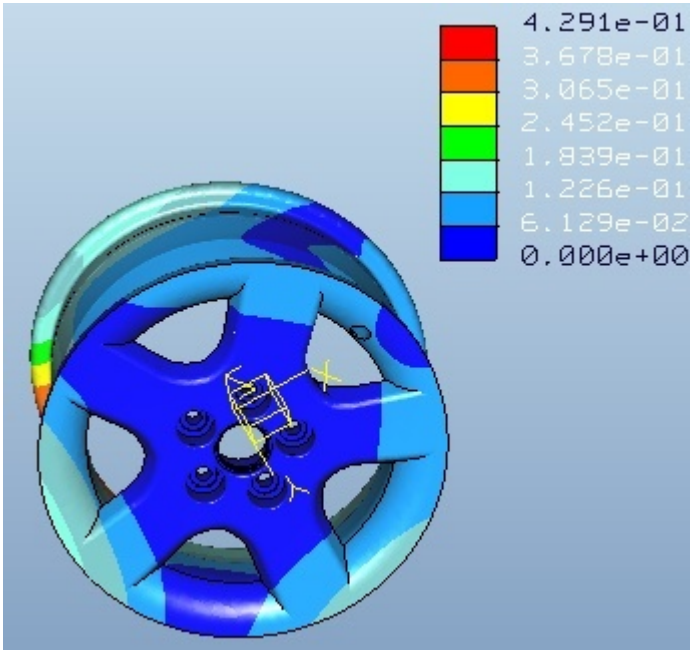

Fig. E4: Displacement (mm) of numerical model of wheel with parabolic shape cooling hole

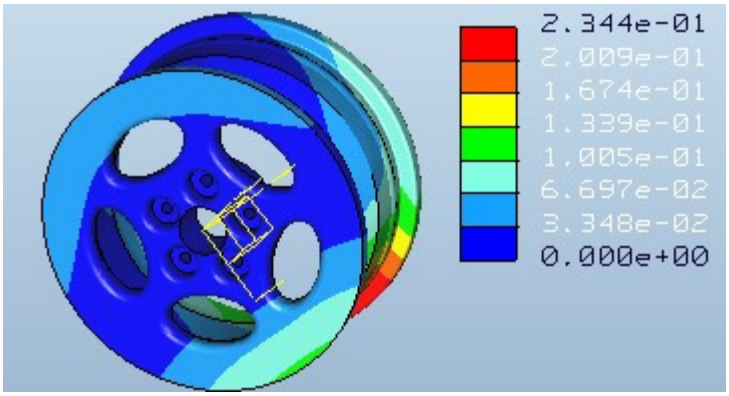

Fig. E5: Displacement (mm) of numerical model of wheel with oval shape cooling hole

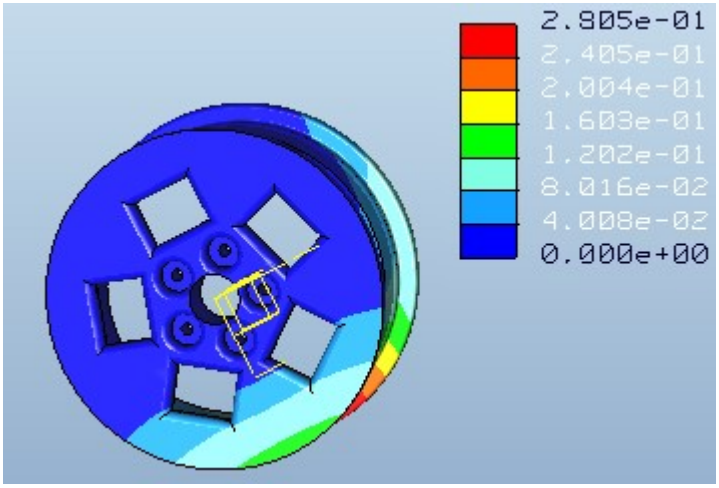

Fig. E6: Displacement (mm) of numerical model of wheel with quadrilateral shape cooling hole

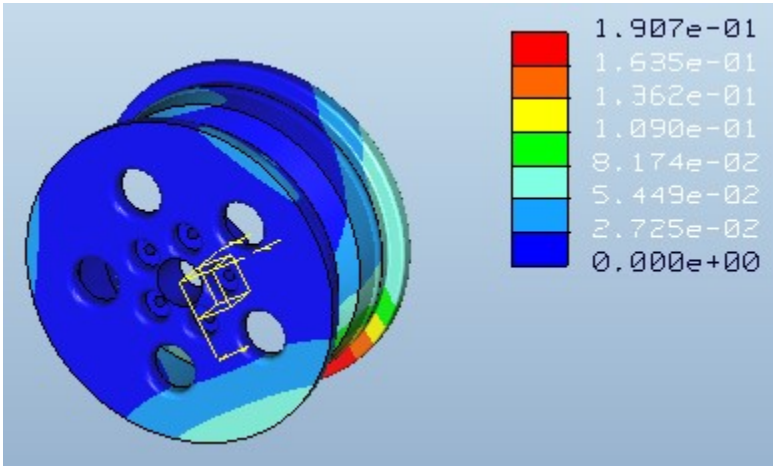

Fig. E7: Displacement (mm) of wheel with oval shape cooling hole at aspect ratio of 1

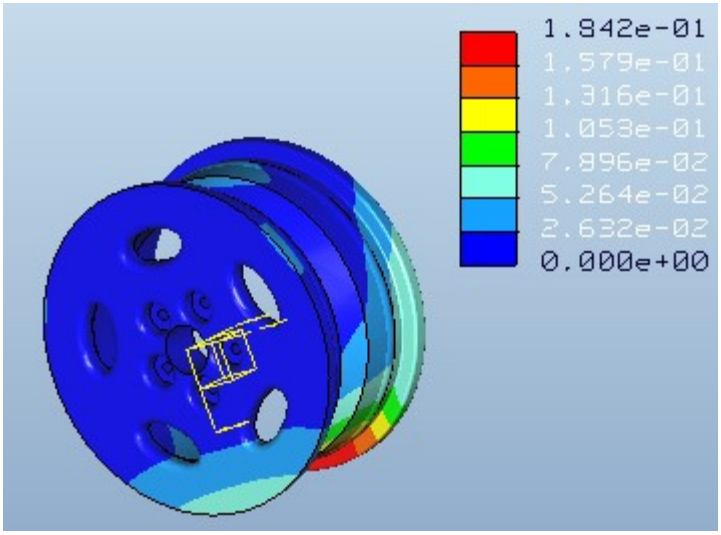

Fig. E8: Displacement (mm) of wheel with oval shape cooling hole at aspect ratio of 0.5

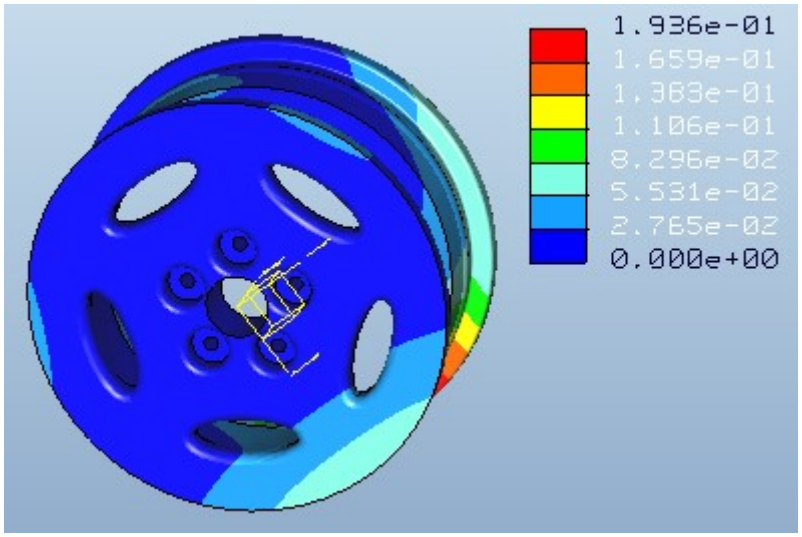

Fig. E9: Displacement (mm) of wheel with oval shape cooling hole at aspect ratio of 0.33

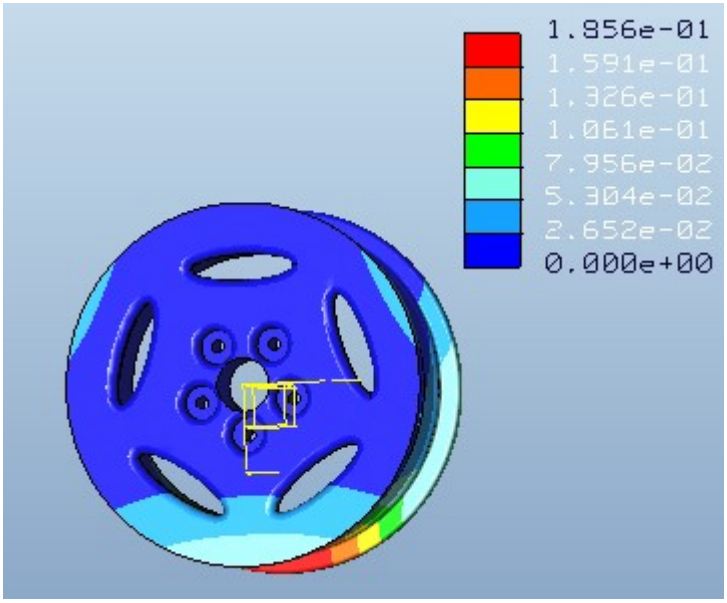

Fig. E10: Displacement (mm) of wheel with oval shape cooling hole at aspect ratio of 0.25

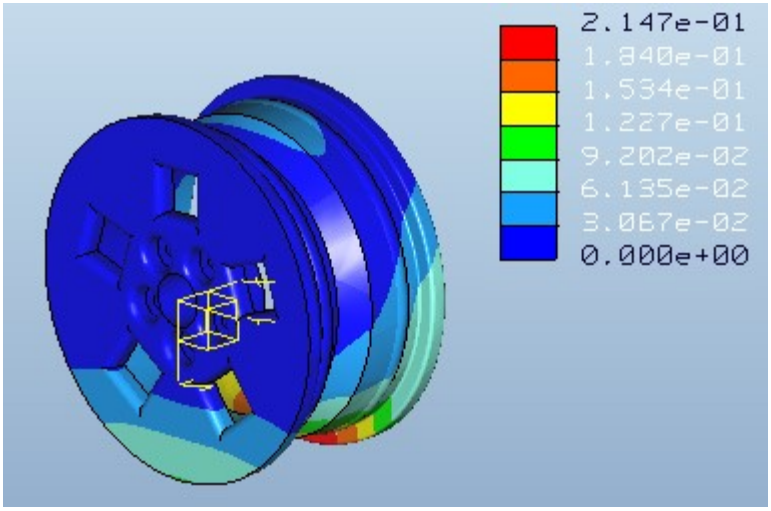

Fig. E11: Displacement (mm) of wheel with quadrilateral shape cooling hole at aspect ratio of 1

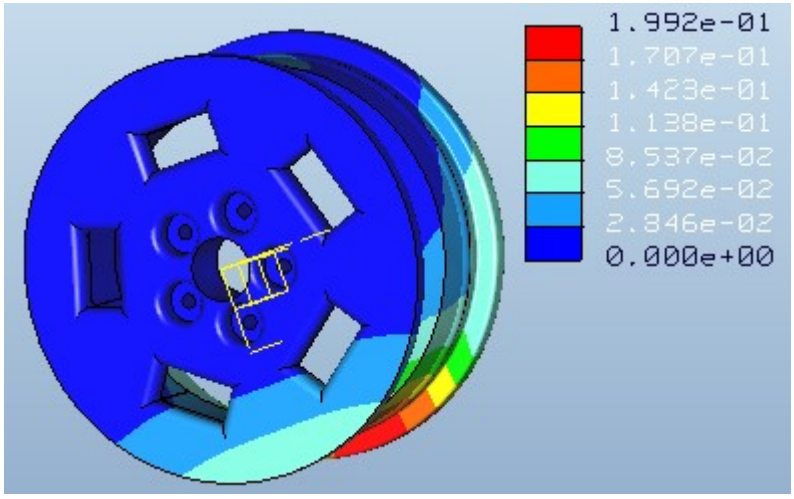

Fig. E12: Displacement (mm) of wheel with quadrilateral shape cooling hole at aspect ratio of 0.5

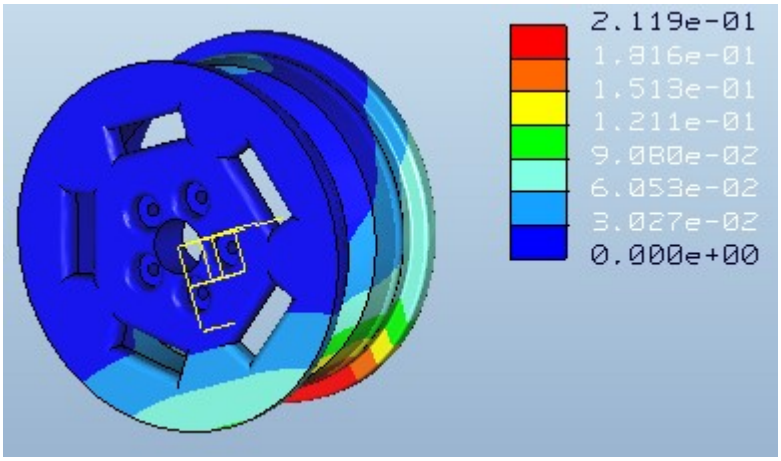

Fig. E13: Displacement (mm) of wheel with quadrilateral shape cooling hole at aspect ratio of 0.33

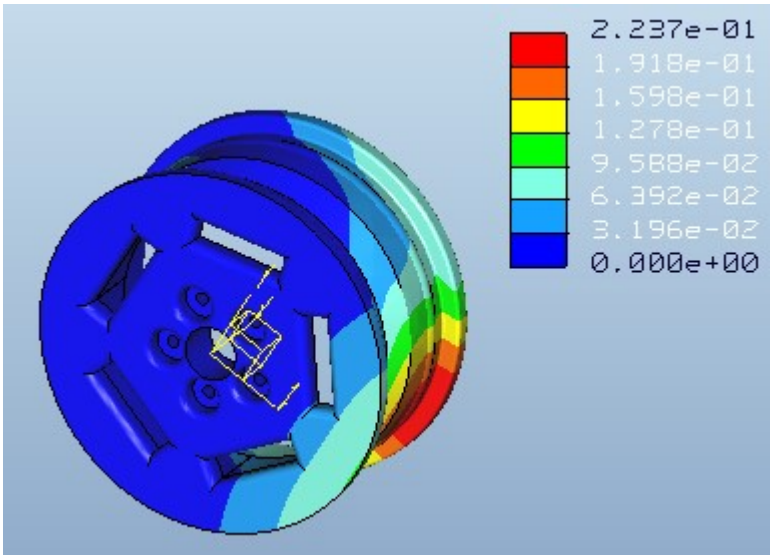

Fig. E14: Displacement (mm) of wheel with quadrilateral shape cooling hole at aspect ratio of 0.25

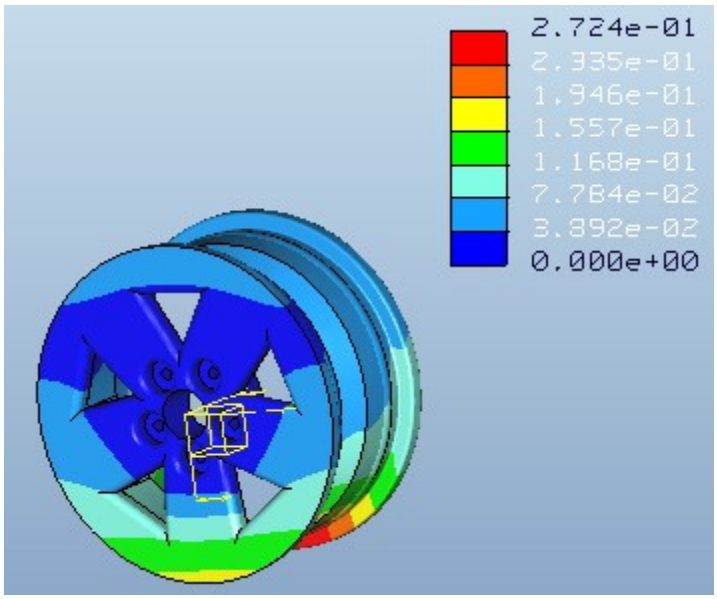

Fig. E15: Displacement (mm) of wheel with triangular shape cooling hole at aspect ratio of 1

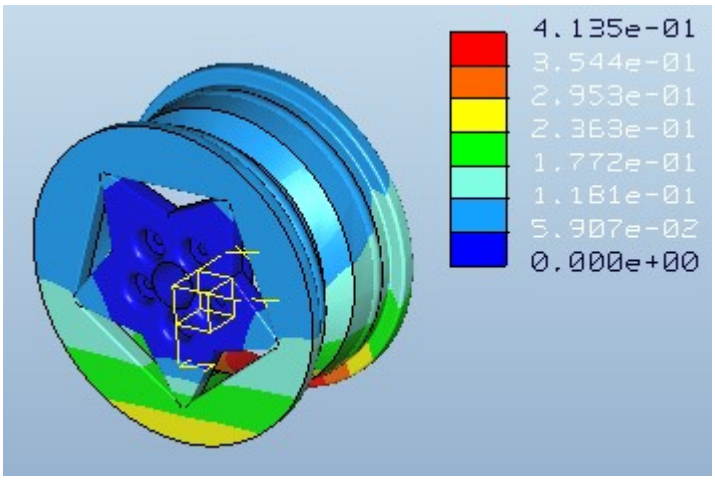

Fig. E16: Displacement (mm) of wheel with triangular shape cooling hole at aspect ratio of 0.5